2016

Variability of Optical Counterparts to X-ray Sources within the Galactic Bulge Survey

Christopher Bradley Johnson
Louisiana State University and Agricultural and Mechanical College, cjoh285@lsu.edu

VARIABILITY OF OPTICAL COUNTERPARTS TO X-RAY SOURCES WITHIN THE GALACTIC BULGE SURVEY

A Dissertation

Submitted to the Graduate Faculty of the
Louisiana State University and
Agricultural and Mechanical College
in partial fulfillment of the
requirements for the degree of
Doctor of Philosophy

in

The Department of Physics and Astronomy

by
Christopher B. Johnson
B.S., University of Arizona, 2010
M.S., Louisiana State University, 2015
August 2016

This accomplishment is dedicated solely to my mother, and to my family for many generations to come.

Acknowledgements

This work could not have been completed if it were not for the incredible support of my family and friends. I would like to give a special acknowledgement to my late grandfather, Marvin Allison Packett, who was a design engineer at General Motors for giving me the ability and encouragement to critically think and analyse problems when presented before me. Understanding physics would have been impossible without the mathematical skills that I acquired from my mother, Patricia Ann Johnson, and her tireless efforts to nag me at every turn and her attitude towards never giving up or giving in.

I would like to give huge thanks my advisor, Rob Hynes, who has taken the time to instill in me all of the knowledge that he could and to pass on his everlasting appreciation of the cosmos and the underlying physics contained within. I would not have been able to finish in the time and manner that I did had it not been for the guidance and the many "closed door" talks we had in his office. I would like to thank my collaborators Peter Jonker, Manuel Torres, Tom Maccarone, Chris Britt, Brad Schaefer, and Betsy Green for their many comments and suggestions on papers and interpreting questions through email and conversation. I would also like to thank my committee for their support.

I would not have been as successful in graduate school without the invaluable preparation I received from my undergraduate program at the University of Arizona. I would like to thank Steward Observatory and, specifically, Dr. Elizabeth "Betsy" Green for essentially molding me in to the researcher I am today.

My love for math and calculus are the product of one of the most passionate teachers I have ever had the pleasure of meeting, let alone, taking classes from. When I was at Macomb Community College, Mr. Zak Musallam (Mr. USA) showed me that math and functions are easy and fun through his patented "polynomial dance" and that is something I will never

forget.

I give immeasurable thanks to the time spent unwinding at the local watering holes when graduate school was not fun. Whether it was playing pool and eating popcorn at Spanish Moon, ping pong and darts with the locals at Radio Bar, root beer floats and trivia at Chimes, or "Thirst and 10" at Varsity, life seemed a bit easier, at least for a little while. An incalculable amount of hours were spent at Highland Coffees writing this dissertation and deserves special recognition.

I would also like to recognize the many people who have influenced me and my life in the past, present and future and who continue to do so in a loving and caring way. I would love to especially thank Edward Montiel, Ted Chao, Zack Edwards, Kelsie Krafton, Ali Dreyfuss, "Dramber", the "Lovely" Jessica Pattison, "Shrek", Anton Joe, Ishita Maity, Jon Cripe, Jonny and Kat, and too many more to name!

This work was supported, in part, by the National Science Foundation under Grant Number AST-0908789 and by NASA through Chandra Award Numbers AR3-14002X, GO4-15047X, and AR5-16004X issued by the Chandra X-ray Observatory Center, which is operated by the Smithsonian Astrophysical Observatory for, and on behalf of, the National Aeronautics Space Administration under contract NAS8-03060. A portion of my travel, to and from conferences, was supported by two Louisiana Space Grant Consortium (LaSPACE) Graduate Student Research Awards (GSRA) for the years 2013 and 2015.

Table of Contents

List of Tables

List of Figures

Abstract

The Chandra Galactic Bulge Survey (GBS) is a shallow, wide field survey to search for and classify X-ray sources in the Galactic Bulge. Specifically, we are looking for Low Mass X-ray Binaries (LMXBs): systems containing either a neutron star or black hole that is accreting matter from a roughly stellar mass companion via Roche-Lobe overflow. My research uses optical, time-series photometry from the DECam instrument on the Blanco 4.0 m telescope at the Cerro Tololo Inter-American Observatory to identify counterparts to new X-ray sources in the GBS. For the systems that are variable in brightness in the optical, I use the morphology of the light curves and the relative proportion of optical and X-ray light, to identify high inclination systems through eclipses, and to determine what periodicity, if any, is present in the optical light. Combining these properties with optical spectroscopic campaigns, I can partially or fully classify the X-ray sources and their counterparts. The GBS contains a variety of X-ray sources, including Low Mass X-ray Binaries, Cataclysmic Variables, Intermediate Polars, Active Galactic Nuclei, W Ursa Majoris stars, RS Canum Venaticorum stars, active stars, flare stars, slowly pulsating B stars, and intermediate polars. Only a handful of sources are identified as potential new Low Mass X-ray Binaries in quiescence, which places limits on the number of such systems in the Galaxy.

In addition to the GBS work, I have done work on Cataclysmic Variables, focusing on archival and historical light curves to get a glimpse at the evolution of these systems. In the case of classical novae, one popular evolutionary model suggests that post-eruption the system should fade in brightness over a timescale of 50-100 years between 0.2-1.0 mag/century. I make use of the Harvard College Observatory Plate Archives to search for photographic plates containing the target systems and manually extract magnitudes and dates to look for trends in the long term light curve.

1. Introduction

In this chapter, I will begin by discussing the background of the science topics comprising my work, beginning with the life of a star and the evolution of binary systems. I will then focus more on the particular science questions addressed by my work before moving on to describing particular types of systems I have been focusing on in my research.

1.1 Basics of Binary Evolution

1.1.1 Single Star Evolution

The stellar lifecycle of a star begins during the pre-main sequence (PMS) protostar phase when a molecular cloud has reached a critical density and it starts contracting in on itself due to self gravitation. PMS stars are classified as T Tauri stars or Herbig Ae/Be stars, the former being low mass, the latter being intermediate mass with both types containing circumstellar disks. As the PMS star continues to contract, the critical internal temperature is reached in the core and hydrogen starts fusing. At this point in time, the star is said to be on the main sequence (MS). The more massive stars evolve off of the main sequence quickly, on timescales of only a few million years. By comparison, stars like the Sun take 10 billion years to evolve off the main sequence. The evolutionary timescale is dependent on the mass of the star and can be quantified with the relation $\tau_{MS} \propto \mathrm{M}^{-2.5}$, where τ_{MS} is the time spent on the main sequence and M is the mass of the star. The least massive stars take much more time to finish burning hydrogen in their cores. After hydrogen core burning terminates, stars continue burning hydrogen in a shell around a helium core. The star then begins to swell and leave the main sequence to follow the Red Giant Branch (RGB) where their radii get larger and the energy emitted per unit time gets larger and the effective

temperature decreases. Eventually, enough helium is produced in the core to ignite helium burning at the tip of the RGB, until it, too, is depleted followed by shell helium burning when the star enters the Asymptotic Giant Branch (AGB). Lighter stars (≤ 8 $M_\odot$) finish life by being unable to fuse carbon, nitrogen, and oxygen in their cores, blowing off the outer layers (i.e. a planetary nebula in specific cases) and leaving behind a hot, cooling White Dwarf (WD). The heaviest stars (≥ 8 $M_\odot$) will continue piling up the ash from the previous fusion reactions in their cores, then ignition occurs, until the fusing of iron. Fusing iron causes the star to lose energy (an endothermic process), so stars cannot burn iron in large quantities under normal circumstances. When enough iron has accumulated in the core, the core cannot be supported by electron degeneracy pressure and it collapses and a supernova is set in to motion. As a crude guide, intermediate mass star supernovae leave neutron stars (NS) behind while more massive stars may result in a black hole (BH) (Tauris & van den Heuvel 2006).

White dwarfs are composed primarily of degenerate material consisting of either primarily helium or carbon and oxygen. They are deficient in hydrogen, being the remnant of the old core of a star in which the hydrogen fuel was used up. For the higher mass progenitors, oxygen, neon, and magnesium may be present. They range in mass from a tenth of a solar mass up to the Chandrasekar Mass Limit of 1.4 $M_\odot$, which is the maximum mass that electron degeneracy pressure can support (Warner 2003). The radius of a WD is approximately the same as that of Earth, though there is a dependence on the mass (Warner, 2003). Counterintuitively, more massive WDs have smaller radii, which is true for any degenerate matter. NSs are also degenerate and have a mass distribution that peaks around the Chandrasekar Mass, with an upper limit that is around 2 $M_\odot$ (Özel & Freire, 2016). Composed primarily of neutrons, the exact inner structure of NSs is still an open question, though it is thought that below the outer crust, the neutrons form a superfluid. Supported by neutron degeneracy, NSs are much more compact than WDs, reaching densities 4–5 times nuclear

density. Typical NS radii are on the order of 10 km, but precise measurements of a NS radius have not yet been made. BHs have a radius (known as the Schwarzschild radius) which is well defined by General Relativity and depends only on the mass and spin of the BH (Frank et al., 2002):

$$\mathrm{R}_{Schw} = \frac{2GM}{c^2} \tag{1.1}$$

where G is the gravitational constant, M is the mass of the BH, and c is the speed of light in vacuum. The Schwarzschild radius of a BH is formed after the BH has collapsed beyond what any pressure can support as the speed of the pressure wave would have to exceed c, the speed of light. As an example, the R_{Schw} of a BH with zero spin and 1 $\mathrm{M}_{\odot}$ would be 3 km and scales linearly with mass.

1.1.2 Binary System Evolution

We often find the end products of the stellar life cycle in binary star systems and refer to them as stellar remnants or compact objects. In a binary system, the effective gravitational potential in the rotating frame of the system is called the Roche Potential, $\Phi_{\mathrm{R}}(\overrightarrow{r})$, and is given by the following equation (assuming that stars can be described as point masses):

$$\Phi_{\mathrm{R}}(\overrightarrow{r}) = -\frac{GM_1}{|\overrightarrow{r} - \overrightarrow{r_1}|} - \frac{GM_2}{|\overrightarrow{r} - \overrightarrow{r_2}|} - \frac{1}{2}(\overrightarrow{\omega} \times \overrightarrow{\mathrm{r}})^2 \tag{1.2}$$

In Equation 1.2, $\overrightarrow{r}$ is the displacement from the center of mass of the system, $\overrightarrow{r_1}$ is the distance to M_1 and $\overrightarrow{r_2}$ is the distance to M_2. Figure 1.1 shows a cross section of the equipotential surfaces in the orbital plane where force is perpendicular to the equipotentials. There are 5 equilibrium points called "Lagrange points" in equipotential space labelled L_1–L_5. The saddle point in between the two stars, L_1, is of particular interest in binary systems. This is known as the inner Lagrange point and the equipotential surface intersecting this saddle-point is called the Roche lobe. As the more massive star in the binary sequence evolves, it

can expand past its Roche lobe and matter can begin flowing from the more massive star onto the less massive star. As material accretes, it forms a stream out of the L_1 point which then forms an accretion disk of material around the compact object which starts orbiting in a Keplerian orbit. This type of binary system is called a *semi-detached* binary. When the mass ratio of the two stars, $q = \frac{M_{donor}}{M_{accretor}} = \frac{\mathrm{M_2}}{\mathrm{M_1}}$, exceeds a certain value (which depends on the equation of state of the donor), mass transfer is unstable and results in the accretion rate increasing, creating a positive feedback loop. This situation can then lead to an atmosphere of gas surrounding both stars if the material overflows the L_2 point, which is then called the common envelope (CE). While in this phase of binary evolution, the system loses energy and angular momentum due to friction inside the CE, and the stars get much closer together (Paczyński, 1976). When both stars fill the Roche lobe, the system is called a *contact* binary. If neither star fills their Roche lobe, we call it a *detached* binary.

When a massive star finishes its evolution in a supernova, the binary may become unbound. The companion can be ejected from the binary due to mass loss during the supernova. The result of the companions ejection is referred to as a "Blaauw kick" (Blaauw, 1961). If the binary loses $\geq 1/2$ its mass in the ejection, the Blaauw kick will unbind the system. For example, the typical NS mass is 1.4 $\mathrm{M_\odot}$, which is ≥ 8 $\mathrm{M_\odot}$ less than the progenitor star. If mass loss were the only determinant in whether the system remains bound, there should be no NSs with low mass companions. However, the size of the core determines the end state of the star and the core size is determined before the CE stage. During the CE phase, the primary may expel more mass from the system through the outer Lagrange points than the supernova later blows away allowing the system to remain bound. The other factor that needs to be accounted for is the presence of asymmetries in the supernova explosion or a "natal kick". This kick is oriented randomly with respect to the binary motion, so it could serve either to remove or add angular momentum and could also cancel out the Blauuw kick if both kicks are oriented directly opposite one another.

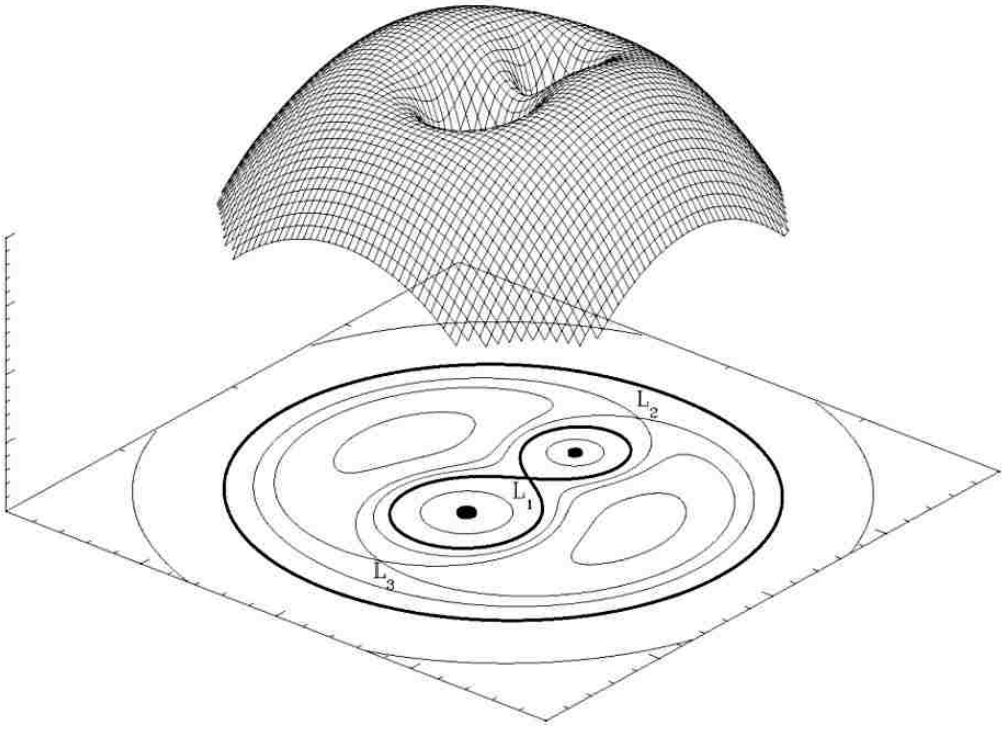

Figure 1.1: A cross section of the orbital plane showing the intersection of the plane with equipotential surfaces of the effective gravitational potential between two stars in a binary. The saddle point in the middle marks the equipotential surface called the Roche lobe. Matter can flow across this saddle point to accrete onto the companion star. Figure reproduced from Frank et al. (2002).

1.1.3 Types of Binaries

If the system remains bound, it can get closer together still through magnetic braking, which occurs when the magnetic field of the companion star interacts with its stellar wind. Material is forced to corotate with the magnetic field lines at the Alfvén radius and serving to remove angular momentum from the system (Ivanova & Taam, 2003). For very close binaries (P_{orb} $\leq$ 2–3 hr), gravitational radiation becomes an important mechanism for removing angular momentum from the system as well.

If the system still remains bound and the donor star ends up filling its Roche lobe, it is

called an X-ray Binary (XRB), and contains either a NS or a BH primary. Binaries with low mass companions ($\leq 1\,M_\odot$) are Low Mass X-ray Binaries (LMXBs), while those with high mass companions are High Mass X-ray Binaries (HMXBs). Systems with intermediate mass companions ($\sim$1–8 $M_\odot$) are called Intermediate Mass X-ray Binaries (IMXBs). LMXBs accrete through Roche lobe overflow once the companion gets close enough through angular momentum loss or evolves to fill the Roche lobe itself. The size of the star is then the size of the Roche lobe, which is approximated by Paczyński (1971) as:

$$\frac{R_{\rm RL}}{a} = 0.462 \left(\frac{q}{1+q}\right)^{1/3} \tag{1.3}$$

where a is the binary separation and $R_{\rm RL}$ is the Roche lobe radius. Paczyński's relation is only valid to within 2% error when using a mass ratio $q \leq 0.8$. A slightly better approximation can be implemented for any mass ratio, $0 \leq q \leq \infty$ using the Eggleton (1983) relation:

$$\frac{R_{\rm RL}}{a} = \frac{0.49q^{2/3}}{0.6q^{2/3} + \ln(1+q^{1/3})} \tag{1.4}$$

which has been shown to be better to within 1% error.

Initially, accretion through Roche lobe overflow in NS IMXBs is not stable because of the high mass ratio in these systems. Advances in computing have shown that the evolution of the donor in NS IMXBs can lead to a state of stable mass accretion (Pfahl et al., 2003). On the other hand, BH IMXBs can stably transfer matter through their Roche lobe much like the system GRO J1655-40 (Orosz & Bailyn, 1997). HMXBs accrete material through high stellar winds from the companion *or* from Roche lobe overflow, or some combination of the two. Be XRBs are a type of HMXB that consist of a spectral class Be star showing hydrogen emission lines and a NS in orbit around it. These systems can form an excretion disk in the equatorial plane of the star, which is not in general, the same as the orbital plane

of the system. The NS can then interact with this excretion disk and, in some cases, it can pass through the disk as it approaches the closest point of its orbit (periastron). The high mass companions of HMXBs do not live for long and so these systems can trace regions of recent star formation (Grimm et al., 2003). They are also optically very bright because of their high mass companion.

If the primary is not massive enough to undergo a core collapse supernova and form a NS, it will become a WD binary system. A WD accreting material from a companion though RLOF is called a Cataclysmic Variable (CV) and can show many different types of dramatic changes in variability. The most dramatic event occurs when enough hydrogen has accreted onto the surface of the WD to ignite fusion, which results in a classical nova (CN) eruption (see Section 1.9) in which the system brightens optically by 2–8 orders of magnitude for periods lasting days to months (Warner, 2003). Dwarf Nova (DN) are another type of CV in which brightening events occur in the accretion disk. A third type of CV is referred to as a nova-like (NL) variable. NLs are known as "non-eruptive CVs" or CVs that have not been observed to undergo CN or DN type outbursts (Dhillon, 1996). NLs have been found to accrete material at rates between 10^{-8}–10^{-9} $M_{\odot}$/year, very similar to DN in outburst but much higher than DN in quiescence.

If the WD has a magnetic field, and depending on the strength of that field, the accreting material may or may not form a disk and will follow magnetic field lines from the magnetosphere radius, R_{μ}, to the poles of the WD. In the process, magnetic braking slows the spin of the WD until it is tidally locked with the donor star, and the spin period is the same as the orbital period (Warner, 2003). This type of system is called a Polar or an AM Her star. A moderately strong magnetic field can result in a slower magnetic braking process, which leaves the WD with a spin period slower than its birth spin, but still faster than the orbital period (Patterson, 1994). These systems are called Intermediate Polars (IPs) or DQ

Her stars, and can also have a truncated, outer disk before magnetic pressure dominates gravitational pressure and the matter follows field lines on to the WDs poles.

NS or BH systems in which the donor is a WD are called Ultra Compact X-ray Binaries (UCXB). When the primary itself is a WD, the system is called an AM Canum Venaticorum (AM CVn), named for the prototypical system. These all have orbital periods below 70 minutes, sometimes as short as 5 minutes (Nelemans & Jonker, 2010). In order to fit inside an orbit this fast, the disk has to be quite small and due to the extremely compact sizes of these systems, they are optically faint. The only possible components of these binaries are WDs, NSs, BHs, and the cores of evolved giant stars whose hydrogen has been stripped in the CE phase.

Stellar remnants are not the only sources of X-rays throughout the cosmos. RS Canum Venaticorum (RS CVn) stars are cool, late-type, close binaries with deep convection zones, high rotation and active magnetic fields. Contact binaries sharing a common envelope that show eclipses are commonly referred to as W Ursa Majoris (W UMa) stars. Algol systems form when enough matter accretes from a more massive star to move the companion up to a bluer spectral class, all the while evolving off the main sequence. This results in a system with a less massive, more evolved star and a more massive, less evolved star. Single M dwarf stars (red dwarfs) and K stars can also have large flares and coronal mass ejections that emit X-rays. The X-ray luminosity for these objects is closely related to the spin period of the star and for most stars, including the Sun, X-rays are emitted at some level and can be detected if they are close enough to Earth.

Currently, models predicting binary populations have large uncertainties and often do not agree with one another. Models predicting the populations of compact objects with and without companions can differ by orders of magnitudes (Kalogera (1999); Pfahl et al. (2003); Ivanova et al. (2005)). One of the largest uncertainties in modeling comes from the CE phase of binary evolution. The energy lost in ejecting the envelope strongly influences

mass and period distributions of LMXBs (Pfahl et al., 2003). It is in this phase that the system loses much of its angular momentum, allowing the formation of a close binary (Taam & Sandquist, 2000). Predicting the correct distribution of X-ray sources in our Galaxy is a very difficult task for theorists.

1.2 Previous X-ray Surveys

Previous surveys of Galactic X-ray sources, such as ChaMPlane (Grindlay et al., 2005), have concentrated on the Galactic Plane or the Galactic Center region (Muno et al., 2003). The reason for this is that source density is much higher here, so telescope time can be used more efficiently (Muno et al., 2003). The extinction is so high in the disk of the Milky Way ($A_V \sim 30$) that the search for counterparts in this region is conducted in the infrared. Establishing an optical/infrared counterpart is a necessary first step for characterizing the properties of most X-ray emitting objects. Surveys of this type have run into problems with source crowding, mainly because so many possible counterparts are present for each detected X-ray source that it is difficult and time consuming to identify the true counterpart. Successful identifications have occurred largely in low extinction windows (Mauerhan et al., 2009; Hong et al., 2012). ChaMPlane is a serendipitous survey relying on existing deep exposures of the Galactic Plane and Bulge regions, with exposures from 20 - 100 ks (Grindlay et al., 2005), and using follow up data from optical ground based telescopes. The Bulge Latitude Survey (BLS) is conducted by the ChaMPlane team and extends above and below the Galactic Center in narrow strips at $|l| < 0.35°$ to $|b| < 1.5°$. The BLS measured the fall-off of the faint X-ray point source population with height above and below the plane of the disk. Revnivtsev et al. (2006) used a 1Ms Chandra pointing of the Galactic Ridge to show that the X-ray emission from this region is actually made up of many weak X-ray admitting point sources, mainly CVs and single stars.

Studies of X-ray sources in Globular Clusters (GC) can escape the problem of high extinction, but the crowding of possible counterparts is much worse and the formation mechanism in GCs is different than in the rest of the Galaxy (Heinke, 2010). LMXBs in GCs are formed primarily through dynamical processes such as tidal capture between NSs and single stars or between single stars and binaries (Clark, 1975). The binary does not remain intact throughout the entirety of binary evolution which is usually seen in the sparser Galactic population. They cannot, therefore, be used as a probe of binary evolution elsewhere. Because of the age and lack of any post-birth star formation in GCs, the stars contained in GC LMXBs are exclusively low mass. BHs should sink to the center of the cluster due to dynamical friction and dynamic interactions should eject all but one of these. GCs are therefore not a good place to search for BH candidates, though Strader et al. (2012) had a surprising result of finding 2 possible BHs in the GC M22 in the Milky Way identified through radio observations. The crowding of possible counterparts is too high to estimate their masses through spectroscopy, however.

Some surveys focus on high energy X-rays because they are affected less by absorption than lower energy X-rays (Hands et al., 2004; Sugizaki et al., 2001). Surveys with instruments like the INTErnational Gamma-Ray Astrophysics Laboratory (INTEGRAL) at the energies > 17 keV suffer from very poor angular resolution ($\sim$12') compared to the focusing X-ray telescopes at lower energies (Krivonos et al., 2012). These surveys focus primarily on HMXBs because the counterparts are so luminous, but the low angular resolution in X-rays severely limits their sensitivity since there could be ambiguous counterparts.

1.3 Neutron Star Equation of State

The nature of the end state of NSs is not very well understood and has been a problem with no clear solution as of yet. Neutron stars contain material at densities unlike anything found

on Earth, fitting 1.4–2.0 times the mass of the Sun in a sphere with a radius of only 10–15 kilometers. Material at this density offers an excellent probe of the strong nuclear force in regions of phase space that are simply unattainable here on Earth (Lattimer & Prakash, 2001). There are many different ideas about how material behaves at these densities, but so far there are not enough systems with known parameters to constrain the Equation of State (EoS) of neutronic material to any high degree (Özel et al., 2009). One reason in particular is that some measurement must be made of both the mass and the radius of the neutron star, or some relationships between the two (Özel et al., 2009). These parameters have been only weakly constrained for a handful of systems (Özel et al., 2010a). Alternatively, the maximum NS mass varies depending upon the model used, so finding heavy NSs would eliminate some EoS models. Indeed, a 1.97(4) $M_\odot$ NS, which is a millisecond pulsar (a rapidly rotating NS) (MSP), has been identified since this project began by Demorest et al. (2010) along with a 2.01(4) $M_\odot$ MSP containing a WD companion (Antoniadis et al., 2013). This level of certainty rules out some "soft" equations of state. There is still, however, merit in measuring more NS masses both to fill out a mass distribution and because there is a chance we could find a higher mass NS. Figure 1.2 shows some of the proposed EoS predictions for mass-radius relationships of NSs. The EoSs that do not reach close to 2 $M_\odot$ have been eliminated by the Demorest et al. (2010) and Antoniadis et al. (2013) measurement.

1.4 Mass Determination Methodology

Tidal stresses circularize orbits quickly compared to the lifetime of the system, so orbits of Roche lobe accreting systems should be circular. The most useful form of Kepler's 3$^{\rm rd}$ law that is used for mass determinations is:

$$f(M_1) = \frac{M_1 \sin^3 i}{(1+q)^2} = \frac{K_2^3 P_{\rm orb}}{2\pi G} \tag{1.5}$$

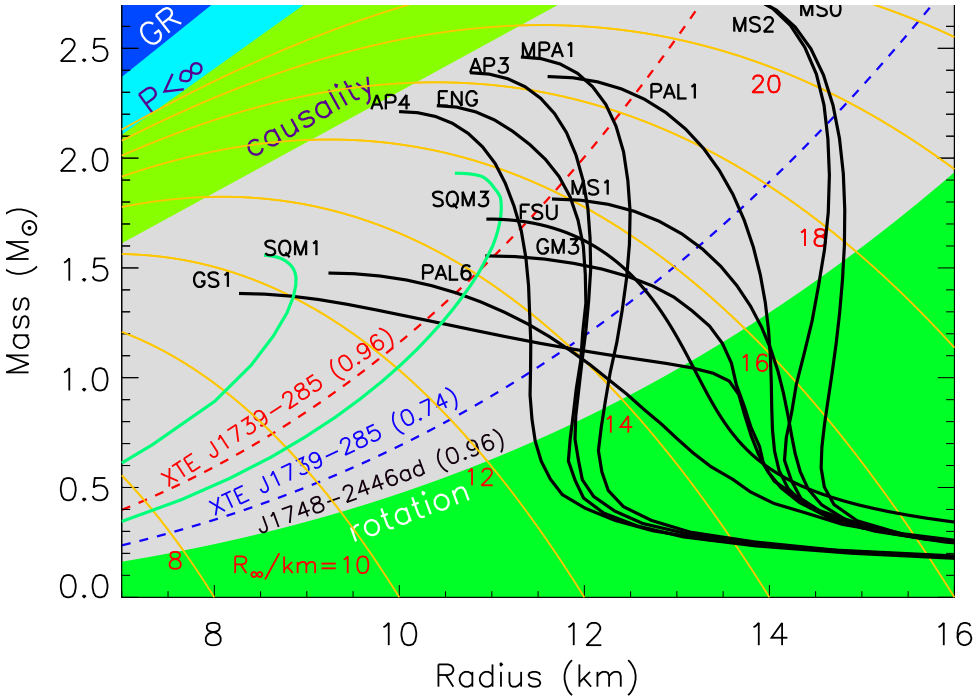

Figure 1.2: A plot of various NS EoS predictions for both maximum NS mass and the predicted mass-radius relation. Figure reproduced from Lattimer & Prakash (2007).

where $P_{\rm orb}$ is the orbital period and K_2 is the semi-amplitude of the radial velocity curve from the donor star. The inclination angle, i, can be constrained by comparing model light curves to the observed light curve, but it is still difficult to determine for most systems. Kepler's 3$^{\rm rd}$ law becomes a lower limit on the mass of the compact object, referred to as the mass function.

This equation is crucial in setting limits on the compact object mass and is extremely easy to calculate. The mass function, $f(M_1)$, only depends on the observables $P_{\rm orb}$ and K_2 which are both directly measurable from the radial velocity curve. Many systems have been classified as a BH based solely on their mass function being larger than 3 $M_\odot$, the assumed maximum mass for a NS. The most convincing case for determining systems parameters in a LMXB is V404 Cyg (Casares et al., 1992) where they find a lower limit on the mass

function of 6.08(6)[1] $M_\odot$. It is also important to note that the same tidal stresses which should circularize the orbit should also lock the rotational period of the companion in sync with the orbital period of the system, much like the Moon is tidally locked to the Earth. This "tidal locking", combined with the fact that the companion's radius is approximately equal to the Roche lobe radius, R_L, is important in that it means the rotational broadening of absorption lines $v \sin i$ is related to the radial velocity semi-amplitude K_2. Rotational broadening of the donor absorption lines occurs when the donor is rapidly rotating. Photons emitted from the side spinning toward our line of sight are blueshifted and those spinning away from us are redshifted due to the Doppler effect. All the light collected from our detector from a given spectral feature is blended producing a net broadening of the absorption lines. The relation between rotational broadening and the mass ratio is given by (Wade & Horne, 1988):

$$\frac{v \sin i}{K_2} = 0.46[(1+q)^2 q]^{1/3} \tag{1.6}$$

A direct measurement of $v \sin i$ and K_2 will allow q to be deduced, and in turn, we can further constrain the dynamical masses of the system. Together with measured ellipsoidal modulations, we can potentially derive i, K_2, $P_{\rm orb}$ and q yielding complete constraints on the dynamical masses of the object and its companion via Equation 1.5.

Eclipsing, interacting binaries are the ideal systems because they offer concrete constraints on the inclination of the system. For a perfect, flat-bottomed eclipse, we know that the system must be near 90° to our line of sight and therefore that $\sin i \approx 1$, $\frac{d(\sin^3 i)}{di} \approx 0$ and the remaining uncertainties that exist in the inclination angle do not propagate through to the mass estimate. It is also important to note that this is independent from the light curve models used to find inclination angles from ellipsoidal modulations.

[1] I use this notation to show the 1σ error on all measurements throughout this work instead of "$\pm$ 1σ"

1.5 The Chandra Galactic Bulge Survey: Survey Design

The Chandra Galactic Bulge Survey (GBS) is a multi-wavelength survey aimed at conducting a census of X-ray sources in the Galactic Bulge (Jonker et al., 2011). The GBS was specifically designed to avoid the problems of crowding and extinction present in previous surveys of the Galactic Center, while giving up as little as possible in the way of source density. The GBS makes use of both optical and X-ray imaging of two $6^\circ \times 1^\circ$ strips located 1.5° above and below the Galactic Plane, cutting out the region $b < 1^\circ$ to avoid copious amounts of dust in the Galactic Plane. An extinction map of the observed regions and detected sources are shown in Figure 1.3. Since its inception, the GBS has grown to include follow-up IR, UV, and radio observations. The X-ray sources were detected with the Chandra X-ray Observatory (CXO) which is a focusing telescope using grazing reflections from parabolic mirrors to focus the X-rays and operates in the soft to hard X-ray regime spanning $0.5-8\,\mathrm{keV}$. The resolution of CXO is quite good, getting down to ∼0.6" positional error for sources close to the optical axis. For observations of sources that are more off-axis, the resolution lowers to ∼10" at 10' off-axis using the formula in Hong et al. (2005). Most GBS sources have positional errors on the order of 1–3".

X-ray observations in the GBS are intentionally shallow (only 2ks exposures). This stems from the fact that the objects we are primarily interested in, active and quiescent LMXBs (qLMXBs), are typically more luminous in X-rays than other types of sources which give off X-rays such as RS CVn stars and CVs. By keeping X-ray observations shallow, we maximize the proportion of LMXBs to other X-ray sources giving us a higher chance at detection than it would otherwise be. Previous surveys have been deep and narrow "pencil beam" surveys, whereas the GBS is a wide, shallow survey. One of the primary goals of the GBS is to constrain models of binary evolution, particularly regarding the CE phase, by conducting a census of LMXBs in the Galactic Bulge and constraining the dynamical masses

of the binary systems. Jonker et al. (2011) predicted that we would find ∼120 new qLMXBs with confirmed optical counterparts. When these systems are in quiescence, the donor star should make up ∼1/2 of the continuum light which means that ellipsoidal variations should be visible for these systems.

The X-ray observations were made in 2 main epochs, the first being the northern 3/4 of the area which found 1234 X-ray sources (Jonker et al., 2011), though there were 18 duplicates that made it through screening leaving 1216 unique X-ray sources (Hynes et al., 2012). Observations of the last southernmost section of the survey area bring the total to 1640 X-ray sources (Jonker et al., 2014). I will be focusing on the counterparts to the 374 sources discovered in the southern 1/4 of the survey and 50 sources in the northern portion of the survey.

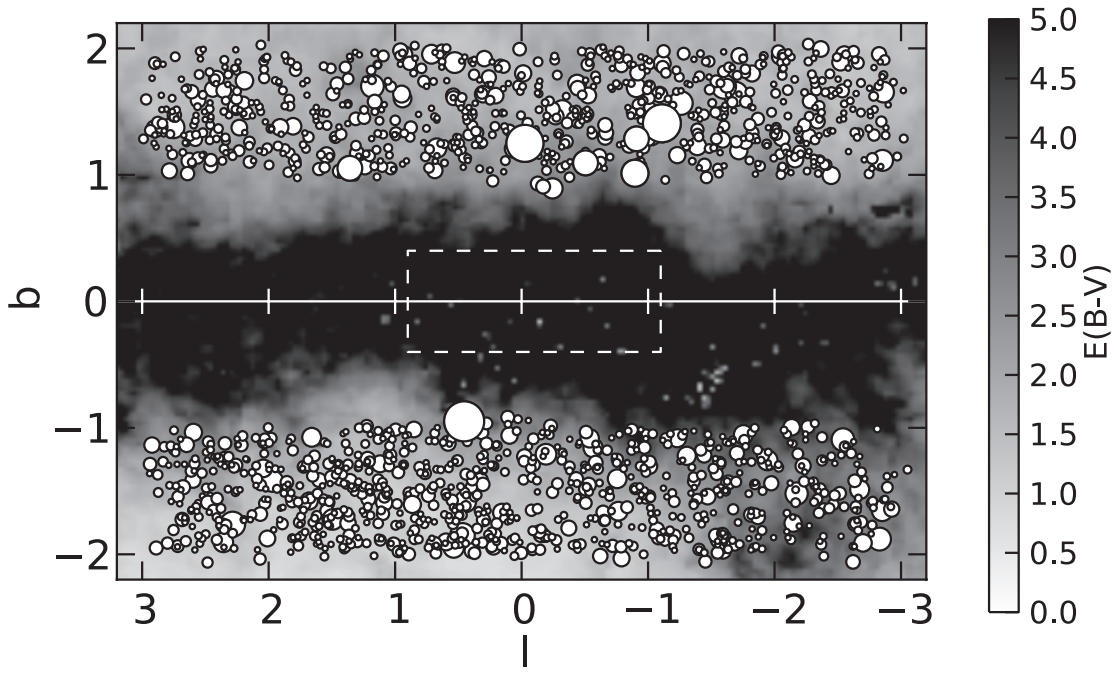

Figure 1.3: An extinction map of the GBS region and observed X-ray sources (white circles) using reddening values from Gonzalez et al. (2012) in the Galactic Plane. The size of the circle is proportional to the X-ray brightness of the source.

The GBS aims to expand the known number of Galactic XRBs, including discovery of the first Galactic eclipsing black hole binary (BHB). By increasing the number of known LMXBs, we are bound to increase correspondingly the number of LMXBs for which mass determinations are possible. Filling out the BH mass distribution also has consequences for models of the history of our Galaxy (Kalogera, 1999). Currently, there are only 23 sources that are confirmed to be BHBs and out of these 23, 16 have some constraint on the mass ratio, q (Özel et al., 2010b). This is a large enough population to raise questions about the lack of BHs with M $<$ 5 $M_{\odot}$. In particular, the mass gap between the most massive NSs and the least massive BHs, if real, is a puzzle that has serious implications for supernova models and binary evolution. It has been suggested by Farr (2012) that the mass gap is a result of systematic errors in estimating the inclination angle of BHBs through ellipsoidal modulations. This uncertainty could be removed by finding eclipsing BH systems as $\sin i \approx 1$ for these. There are currently no known eclipsing BHBs in our galaxy, though there is an eclipsing HMXB in M33 (Orosz et al., 2007). Since known stellar mass BHs have all been discovered in outburst and followed into a fainter quiescent state, it is possible that the accretion disk rim blocks the view of the outburst originating in the inner accretion disk (Narayan & McClintock, 2005). In quiescence, the disk rim is thinner which would allow a more direct view of the central accretion disk (Nowak et al., 2001).

At Galactic Center latitudes, we observe the extinction to be $A_V \leq 5$ so observing in the r' and i' filters lowers this extinction since shorter wavelengths are more affected by scattering than longer, redder wavelengths. To be more precise, $A_{r'} = 0.84 A_V$ and $A_{i'} = 0.6 A_V$ according to Schlegel et al. (1998).

The spectroscopic follow-up campaign for the optical counterparts is being led by Peter Jonker and Manuel Torres at SRON in Utrecht, Netherlands and the European Southern Observatory (ESO). They have collected spectra with the Very Large Telescope (VLT), the New Technology Telescope (NTT) and both the Magellan and Gemini telescopes in

Chile. Danny Steeghs and Sandra Greiss at Warwick, UK, are investigating IR counterparts primarily using the Vista Variables in the Via Lactea Survey (VVV). Thomas Maccarone at Texas Tech University is matching serendipitous UV and radio observations to GBS sources. The population synthesis used for the GBS's population estimates were produced by Gijs Nelemans and his students at Radboud University, Netherlands. I am searching for optical variability of GBS counterparts and combining this with optical spectroscopy to constrain dynamical masses using data collected with my advisor Dr. Robert Hynes at Louisiana State University and Dr. Chris Britt at Texas Tech University.

1.6 Importance of Photometric Variability

Optical variability is a key tool in correctly identifying the optical counterpart to an X-ray source, identifying high inclination systems via eclipses, and constraining orbital parameters such as period and inclination angle. Almost all the optical counterparts of X-ray sources are expected to be variable, except for emission from massive stars, isolated NSs, and coronal emission from nearby, low mass, MS stars.

Accreting systems such as LMXBs and CVs are far more likely to be optically variable than normal binaries. Accretion is ultimately driven by angular momentum loss from either magnetic braking, gravitational wave radiation, or by nuclear evolution of the donor star. Small timescale changes in brightness (i.e. outbursts or flares) can be driven by UV radiation from the disk heating the companion's atmosphere and causing an increase in the mass accretion rate (Ritter et al., 2000). The radius of the companion gets puffed up and allows more material to overflow the inner Lagrange point. This scenario is referred to as irradiation-induced mass transfer. Outbursts and flares can also be caused by instabilities in the accretion disk as material is accreted directly on to the WD rapidly as it is transported inward in short bursts. Local changes in the accretion rate and in the disk can cause ape-

riodic variability or flickering in the light curve. Periodic variability on the orbital period can be caused by several mechanisms within the binary system: ellipsoidal variations caused by deformation of the companion surface as it orbits the compact object, a "hotspot" on the disk created where the accretion stream impacts the disk, the face of the companion being heated by X-rays and becoming more or less visible to our line of sight as it orbits the compact object, or by partial or total eclipses of either the disk or the companion star itself.

Ellipsoidal variations are especially important in constraining a system. When a companion star is near enough to its more massive partner, gravitational tidal effects deform and elongate the companion star along a radial line towards the primary. The companion star ultimately ends up being shaped more or less like a tear drop, with the pointed end at the L_1 Lagrange point. As the companion star orbits, its projected cross-sectional area changes with phase. When it is directly in our line of sight to the primary, a minimum of its surface is visible, while at right angles to our line of sight, a maximum of its surface is visible. The light we see is therefore modulated with the phase of the system exhibiting unequal minima with a period 1/2 that of the orbital period. The amplitude of ellipsoidal modulations depends on the inclination angle of the system and, to a lesser extent, the degree of tidal distortion. This distortion depends on the mass ratio, q, of the system in question.

Based on calculations from Jonker et al. (2011), we expect to find on the order of 10 new BH LMXBs which would greatly improve the mass-distribution of stellar-mass BHs in the Galaxy. This would represent an increase in the population of known Galactic BHs by $\sim 50\%$. There is currently a deficiency of high inclination Galactic BH systems, which is probably due to selection effects in finding outbursting systems. The idea is that to be able to see the X-ray outburst from the disk, the disk itself cannot be in the line of sight obscuring and reprocessing the X-rays (Narayan & McClintock, 2005). Since we are identifying many systems while they are in quiescence instead of finding them in outburst, and because the disk is much thinner in quiescence than in outburst (Nowak et al., 2002), we neatly escape

this problem and expect to find 15–20% eclipsing systems. To date, we have not confirmed any eclipsing BH systems, although we do have several candidates currently being analyzed.

1.7 Classification of X-ray Sources

Different types of systems that produce X-rays do so by very different mechanisms, which produce different energy levels of X-rays compared to optical light. The ratio of the energy being emitted in X-ray wavelengths to the energy being emitted in optical wavelengths is an important indicator which can help distinguish between different source categories. It is independent of distance, since the brightness drops off as $\frac{1}{r^2}$ for both. Therefore, the X-ray to optical flux ratio, $\frac{F_X}{F_{opt}}$, can be used as a diagnostic tool. Actively accreting LMXBs and UCXBs have $\frac{F_X}{F_{opt}} \sim 100$. HMXBs and IPs have $\frac{F_X}{F_{opt}} \sim 1$. Non-magnetic CVs in quiescence have $\frac{F_X}{F_{opt}} \sim 1/100$ while RS CVns, Algols, and W UMas can be even lower. X-ray emission from lower main sequence stars ($\sim$FGKM stars) is ubiquitous and originates from a high temperature corona confined by magnetic field lines generated by a combination of a dynamo effect from the star's rotation and a convective envelope. F_X is limited to $\sim 10^{-3} \times F_{Bol}$, and tends to drop as stars spin down and age. For most stars, the energy is emitted at optical wavelengths so $F_{opt} \leq F_{Bol}$, but for red dwarfs, whose spectrum peaks in the infrared $F_{opt} \ll F_{Bol}$, so $\frac{F_X}{F_{opt}}$ can be significantly higher than 10^{-3}. For close binaries like RS CVns and W UMas, the stars in the binary are spun up faster than an isolated star of the same spectral type and the dynamo effect generating the corona and X-ray emission is stronger than for an isolated star (Rosner et al., 1985). A high $\frac{F_X}{F_{opt}}$ is immediately interesting because it cannot be produced by any kind of active star. For this work, we define the optical flux as:

$$F_{opt} = \nu F_\nu = F_{\nu r' 0} \times 10^{-0.4 m_{r'}} \times \frac{c}{\lambda_{cent}} \tag{1.7}$$

where $F_{\nu r'0}$ is the flux density of a magnitude 0 star for the SDSS r' filter, designed to be 3631 Jy, and $\lambda_{\rm cent}$ is the central wavelength of the filter used (Gunn et al., 1998). For accreting systems, if an orbital period can be determined, $P_{\rm orb}$ constrains the size of the companion via Kepler's 3rd law and Equation 1.3, i.e. $\frac{P_{\rm orb}}{2\pi} = \sqrt{\frac{a^3}{G(M_1+M_2)}}$ since $R_2 = R_{\rm L}$. Typically, systems accreting by Roche lobe overflow that have orbital periods of days have an evolved companion. Those with periods of hours have a main sequence companion, while orbital periods of minutes imply a UCXB. For MS stars, mass and radius are more tightly related, leading to the homology relation $\rm M_2 \approx 0.11 P_{hr}\ M_\odot$ (Frank et al., 2002).

Light curve morphology and spectroscopy are critically important, since, for accreting binaries, it can tell us whether the systems light is being dominated by the disk or the companion. For example, if no ellipsoidal modulations are present and only flickering is seen, the disk is outshining the companion or the system has a low inclination.

A stellar spectrum can tell us not only an approximate effective temperature, but also approximate elemental abundances and how fast it is moving, both in its orbit and rotation. For quiescent systems, the spectrum should be primarily that of the companion star rather than the accretion disk and so can be used to determine the spectral type of the companion and constrain the donor mass.

Emission line Spectroscopy of individual sources is also a vital tool in characterizing objects. The relative strength of emission lines from different elements and ionization states can discriminate between qLMXBs and CVs, and partially discriminate between CVs and IPs. Lines can be broadened by Doppler shifting as the emitting regions move in the system. The Full Width Half Maximum (FWHM) of each line is therefore a measure of velocity dispersion in the emitting regions. The distance from the rest frame line emission position and the central point of the line profile is the mean velocity of the emitting region along the line of sight. For absorption features from the donor, observing the variations in the radial velocity at different phases allows the construction of a radial velocity curve and the

measurement of the semi-amplitude, K_2. The radial velocity of the emission lines does not, in general, provide the semi-amplitude of either of the components, but on average they provide the system's velocity relative to Earth.

Spectroscopic studies of the interstellar absorption features are useful for placing constraints on distances to objects. A well-known tracer of dust and gas is the absorption doublet NaI D $\lambda\lambda$5890,5896. Dust and gas is everywhere in the universe so one would expect to encounter it along any line of sight. The dust both reddens and absorbs radiation from objects and the amount by which this is achieved depends on the column density, chemical composition, and grain size (Draine, 2003). The doublet strength correlates with the amount of dust along the line of sight and recently Poznanski et al. (2012) have shown that there exists a quantifiable relation between the equivalent width of the doublet lines and the extinction along the line of sight. We can then get a distance estimate using the distance modulus and the calculated extinction.

All of these properties together can distinguish between different types of X-ray sources. Each source class is listed with its distinguishing characteristics in Table 1.1 along with references.

1.8 Intermediate Polars

A particularly important subclass of CVs in X-ray selected data sets is magnetic CVs (mCV). Magnetic CVs are formed when the WD possesses a strong magnetic field that may or may not interact with an accretion disk. The strength of the magnetic field determines whether a CV is an intermediate polar (IP) or a polar. IPs are a subclass of mCVs in which the magnetic field of the WD is strong enough to disrupt the accretion disk or, in the case of polars, can completely prevent disk formation. A late-type star fills its Roche lobe and begins

to transfer matter to the magnetic WD where the field lines force the accreting material to flow onto one or both of the magnetic poles in "accretion columns".

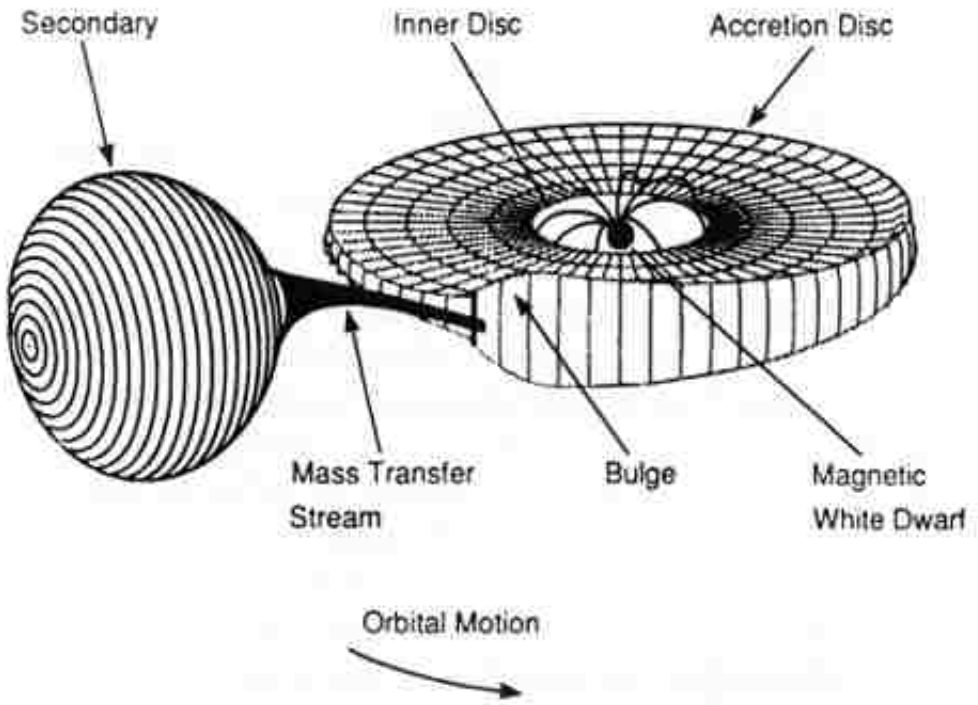

Figure 1.4: The basic structure of an intermediate polar. Photo reproduced from www.nasa.gov

The basic idea behind this magnetically-channelled accretion can be summed up as follows. As material in the disk is transferred inward due to viscous spreading and frictional torques, the magnetic energy density, $\frac{B^2}{8\pi}$, will exceed the local kinetic energy density of the gas, ρv^2, within a certain radius. At this radius, the infalling plasma will be lifted from the disk and guided along field lines on to the poles of the WD (Patterson, 1994). This radius is called the magnetospheric radius, R_μ. In the case where an accretion disk is present, R_μ is smaller than the circularization radius, $R_{\rm circ}$, the radius of the orbiting material around the WD. If $R_\mu > R_{\rm circ}$, then a diskless IP can form. Figure 1.4 shows an artists depiction of the structure of an IP with a truncated disk.

IPs have orbital periods that span from 1.35 hours (V455 And) to about 48 hours (GK

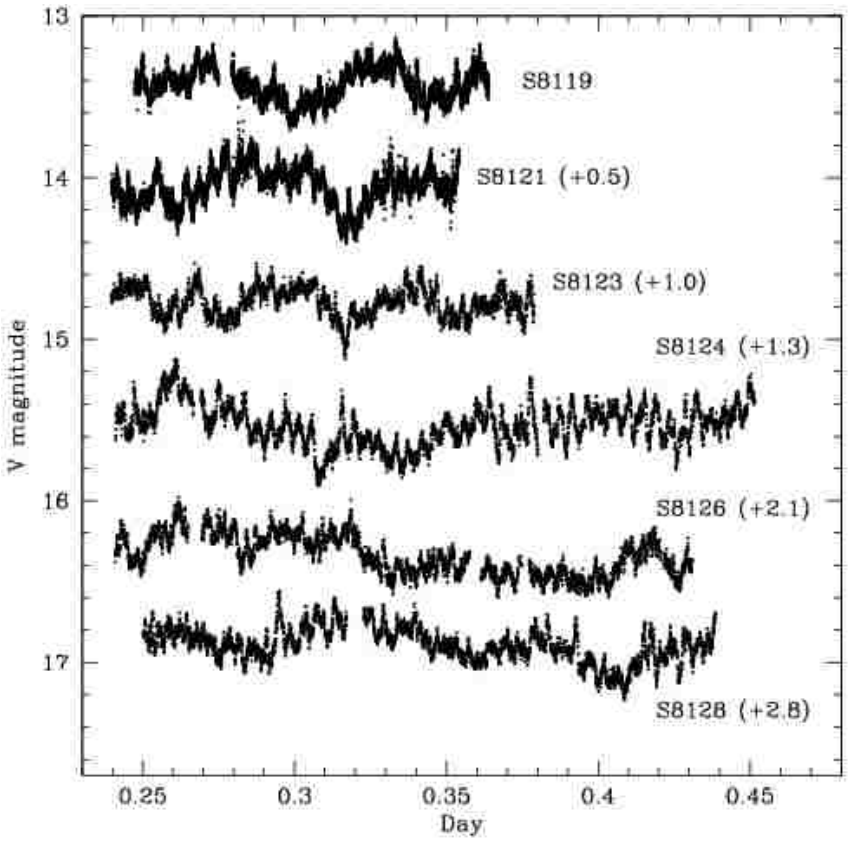

Figure 1.5: The light curve of CC Scl reproduced from Woudt et al. (2012). Individual light curves were taken with the Sutherland High-speed Optical Camera (SHOC) at the South African Astronomical Observatory. Each observing run is identified with an S#### identifier and brackets which indicate a brightness offset.

Per) with WD spin periods, P_{spin}, in the range of 33 secs (AE Aqr) to 4000 secs (EX Hya). The spin period of the WD is governed by two torques: the accretion torque from the angular momentum of the accreted material and the magnetic braking torques from interactions with the WD magnetosphere with the companion star (Warner & Wickramasinghe, 1991). For strong enough braking torques, i.e. strong magnetic fields $> 10^7$ Gauss, the WD will synchronize with the orbital rotation leading to $P_{spin} = P_{orb}$. Synchronized rotation is a fundamental characteristic of polars. In the case of weaker magnetic field strengths, i.e. IPs with $B < 10^7$ Gauss, the WD is spun up to near co-rotation with the inner edge of the accretion disk where the spin period is determined by the magnetosphere radius, R_μ, which

is a function of the magnetic moment of the WD, μ, and the mass transfer rate, $\dot{M}$. For IPs, P_{spin} is always less than P_{orb}. The peak in the spin distribution of IPs roughly follows the relation $P_{orb} \sim 10 \times P_{spin}$ for systems with $P_{orb} < 5.0$ hours (Scaringi et al., 2010).

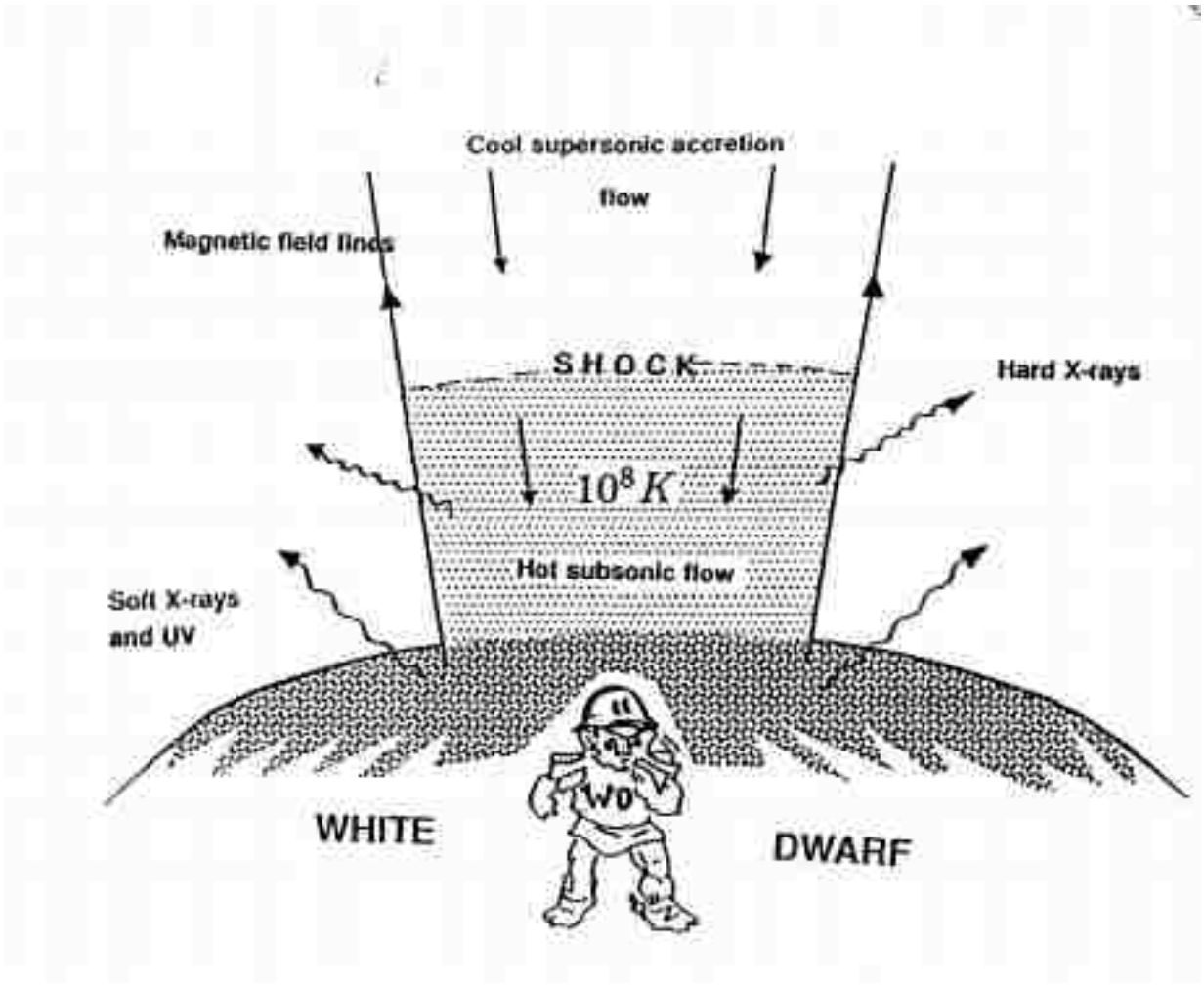

Figure 1.6: Schematic view of the surface, shock region, and magnetic field lines at the pole of a mCV. Reproduced from Patterson (1994).

As the WD spins on its axis, the "bright spot" above the poles can produce modulations coherent to the WD spin period at UV, optical, and X-ray wavelengths. These modulations are vital for helping to classify the system as an IP. The P_{spin} can usually be seen superimposed on the optical light curve if the time resolution is sufficiently small. As an example,

Figure 1.5 shows the light curve of CC Scl from Woudt et al. (2012) and the 389.49 s spin period modulation. A fraction of the energy released from the funneled material at the poles can also fall upon structures in orbit around the WD and result in a third periodicity in the light curve. This frequency occurs at frequencies close to the WD spin frequency. The frequency of this reprocessed light is known as the "orbital sideband" frequency and is found from the relation: $\omega_{\rm repro} = \omega_{\rm spin}$ - $\omega_{\rm orb}$, although sidebands can be produced as multiples of the orbital and spin periods as well.

A substantial portion of the energy emitted in IPs is produced above both the magnetic poles in a shock region. The field strength above the poles is strong enough to steer the ionized gas at very high, supersonic speeds of 3000–10,000 km s^{-1} compared to the sonic speed in the gas that does not reach above ∼100 km s^{-1} (Patterson, 1994). A depiction of this scenario can be seen in Figure 1.6. A "shock" region forms above the poles and the infalling gas can reach temperatures of $\sim 10^8$ K. The average X-ray spectrum from IPs is expected to be very hard (>2 keV) although softer X-ray emission (<0.1 keV) is possible. Most of the soft X-rays get absorbed by interstellar material or the cooler, outer region of the disk and re-radiated to longer wavelengths.

The optical spectrum of an IP usually consists of a continuum with superimposed emission features including the Balmer lines of hydrogen, ionized helium, and CaII. The specific emission features that exist in IPs differ from object to object, but generally include lines dominated by disk features. The lines tend to be broad with widths in excess of ∼1000 km s^{-1} and can show a double structure which is caused by the orbital velocity of the gas in the disk itself. In almost all the confirmed IPs, optical time series spectroscopy shows pulsations in the HeII emission lines along with several other emission lines. These pulsations are attributed to the photoionization of the disk material by the central X-rays originating from the accreting poles and beaming on optically thin regions in the disk plane (Harlaftis & Horne, 1999).

1.9 Classical and Dwarf Novae

Classical novae (CNe) and dwarf novae (DNe) are two more subclasses of CVs that show very different outbursts and utilize different outburst mechanisms. For CNe, accretion happens via Roche lobe overflow where the donor is low-mass MS star. The material from the donor star piles up on the surface of the WD creating a hydrogen-rich layer which will eventually ignite in a violent outburst. The CN explosion is due to a thermonuclear runaway (TNR) on the surface of the WD once enough material has been accreted and the base of the accreted envelope has reached a critical pressure. These explosions are violent enough to eject matter at high velocity with the envelopes enriched in carbon, nitrogen, and oxygen nuclei relative to the Sun (Shara, 1989). The typical CN light curve shows an eruption that can reach between 2–8 magnitudes above its quiescent brightness (see Figure 1.7). CNe, by definition, have had only one *observed* eruption in the past. If more than one has been observed then we call this a recurrent nova (RN). The range of brightness during eruption is correlated with the rate at which the nova fades after maximum brightness. The largest amplitude eruptions which contain the shortest duration are called the fast novae, whereas, the lowest amplitude eruption brightness that last for many years are in the category of slow novae (Warner, 2003).

Contrary to CNe, DNe contain outbursts that occur in the accretion disk and not on the WD surface. When material accumulates in the quiescent disk, the surface density increases. The material is heated above the ionization temperature of hydrogen and the gas in the disk becomes much more viscous (Frank et al., 2002) releasing viscous energy and increasing temperature. At some point, the ionization temperature of hydrogen is reached. The energy release from the increase in viscosity causes a heating wave to propagate throughout the disk, ionizing the remainder of it. The high viscosity disk then accretes at a much higher rate, dumping material onto the WD. This scenario is observed as a sudden brightening of

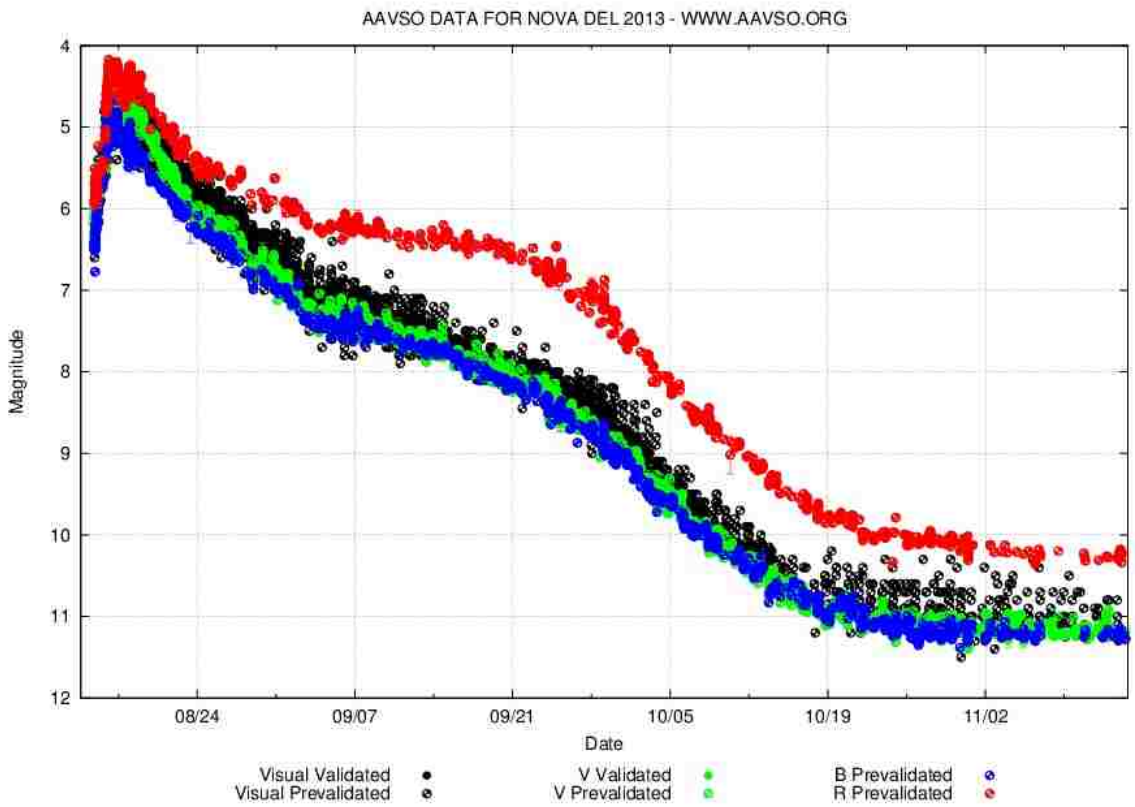

Figure 1.7: The light curve of Nova Del 2013 = V339 Delphini; a typical CN light curve. Reproduced from the AAVSO website.

roughly 2–5 magnitudes and decline to the original brightness over the course of days to weeks (Warner, 2003). The recurrence times of DNe are, on average, ∼10 days to tens of years with a well-defined time scale for each object. The light curve of the typical DN SS Cyg can be seen in Figure 1.8.

1.10 Slowly Pulsating B-type stars

Pulsating stars form a class of variables stars where the star itself is out of hydrostatic equilibrium: the gravitational inward pressure is not fully balanced by outward radiation pressure. A scenario occurs where the stars radius starts shrinking, causing the core to heat up, and in doing so, increased nuclear burning releases increased energy in the core in the

form of radiation. This radiation pressure then causes the radius to increase and slow the nuclear burning and radiation generation. The cycle then continues to repeat itself over and over. This pulsating cycle causes brightening and dimming in the light curve of such systems due to the surface area of the star increasing and decreasing with the oscillation frequency. The oscillations can be characterized as either p-mode (frequencies on the order of ∼30 minutes) or g-mode (frequencies on the order of ∼day or longer) referring to pressure and gravity modes, respectively. Oscillation frequencies uncovered in photometric studies have frequently been used in precision mode identification to interpret the interior makeup of stars (Saesen et al., 2013) through the use of asteroseismologic techniques.

Slowly pulsating B stars (SPB) are a subclass of pulsating variable stars. SPBs are typically mid- to late-type B stars that show photometric periods from 0.5–5 days and masses ranging from 4.0–7.0 M (Waelkens, 1991). The effective temperature range of known SPBs is between 10,000–20,000 K with dense frequency spectra showing low-amplitude, multi-periodicities. The oscillations are high-order, low-degree, gravity mode (g-mode) pulsations that are driven by the κ-mechanism of the Fe opacity bump at T $\approx 1.5\times10^5$ K (Dziembowski et al., 1993). The seismic modeling of SPBs relies on simultaneously fitting the observed frequencies and the empirical values of the f-parameter (Walczak et al., 2012). The non-adiabatic complex f-parameter is defined as the ratio of the radiative flux change to the radial displacement of the photosphere. With the derived values of f and the observed frequencies, available opacity data can be tested along with the chemical composition and the overshooting efficiency of convective cores (Walczak et al., 2012). To perform accurate and precise mode identification, models that deal with cases where non-linear, tidal interactions must be further developed and refined.

The existence of SPBs and their close relation to the δ Scuti stars provides an excellent test bed for probing the deepest layers of the stellar atmosphere through the use of asteroseismology. Mid- to late-type B stars are not known as strong X-ray emitters and have

been shown to emit X-rays in ∼10 % of B3–B9 stars sampled in surveys (Berghoefer et al., 1997). The presence of X-rays coming from the region of a $V = 10$ magnitude B-type star (in the GBS survey) made this optical counterpart intriguing since the X-rays were most likely originating from an unseen companion.

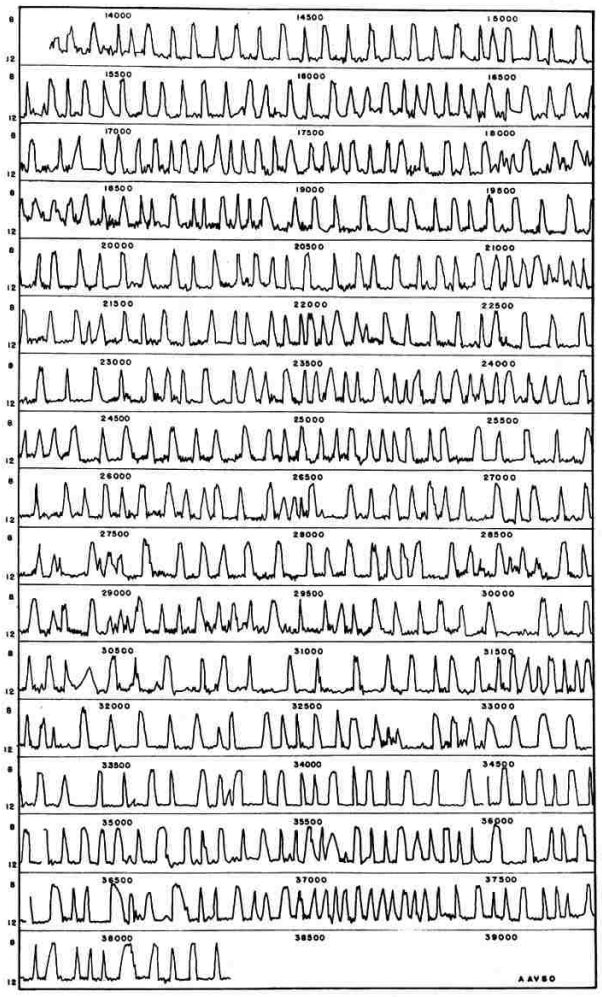

Figure 1.8: The light curve of SS Cygni, a typical DN light curve. This light curve is reproduced from the AAVSO website and spans 1896-1963.

Table 1.1: This table presents a rubric by which X-ray sources can be identified using optical and X-ray properties from existing X-ray data and optical follow-up. References: (1) Warner (2003); (2) Echevarria (1988); (3)Silber (1992); (4)Hynes et al. (2004); (5)Zurita et al. (2003); (6)Remillard & McClintock (2006); (7)Marsh et al. (1994); (8)Menou et al. (1999); (9)Lasota (2001); (10)Casares et al. (1991); (11) Grindlay (1999); (12)Shara et al. (2005); (13)Grindlay (2006); (14)Nelemans (2005); (15)Véron-Cetty & Véron (2000); (16)Güdel (2004); (17)Schmitt et al. (1995); (18)Dempsey et al. (1997); (19)Kupfer et al. (2013); (20)Nelemans et al. (2006); (21)Hynes et al. (2012)

Category	$\frac{F_X}{F_{opt}}$	Optical Spectral lines	$\lvert RV\rvert$ offset ($\mathrm{km\,s^{-1}}$)	Possible Variability	References
CV	0.01 - 1	$\frac{\mathrm{HeI4471}}{\mathrm{H}\beta} = 0.22 \pm 0.09$[1], $\frac{\mathrm{HeII4686}}{\mathrm{H}\beta} < 0.4$	< 500	Flickering, sinusoidal, ellipsoidal, DN	1,2,3,11,13
IP	0.1 - 10	0.17 ± 0.04[1], $\frac{\mathrm{HeII4686}}{\mathrm{H}\beta} > 0.4$	< 600	Flickering plus reprocessed X-ray pulsation, rare DN	1,2,3,11,12
qLMXB (NS)	0.1 - 1	$\frac{\mathrm{HeI4471}}{\mathrm{H}\beta} = 0.12$[3], He II absent [3]	< 1000	Flickering, ellipsoidal, flares on timescale of minutes or longer	7,8
qLMXB (BH)	0.01 - 0.1	$\frac{\mathrm{HeI4471}}{\mathrm{H}\beta} = 0.12$[3], He II absent [3]	< 1000	Flickering, ellipsoidal, flares on timescale of minutes or longer	5,7,8
LMXB	≥ 100	$\frac{\mathrm{HeI4471}}{\mathrm{H}\beta} = 0.3$[3], $\frac{\mathrm{HeII4686}}{\mathrm{H}\beta} = 0.8$[3]	< 1000	Flickering, disk dominated, outbursts on timescale of a week to months, reprocessed thermonuclear bursts in case of NS primaries	4,6,9,10
UCXB	10^3 - 10^5	C/O-He/N emission, H deficient	< 3000	Flickering	20
AM CVn	1	He I+II emission, no H	< 1000	Flickering, $P_{orb} < 1$ hour Outbursts < 4 magnitudes	14, 19
AGN	10 - 1000	Broad or narrow emission lines from both allowed and forbidden transitions	> 1000	Aperiodic variability on a timescale of days or longer	15
RS CVn	0.001 - 0.01	Ca II H & K, Mg II emission	< 100	Sinusoidal, P_{Orb} days	16,18
W UMa	10^{-3} - 10^{-2}	Broadened stellar absorption features of F, G, K stars	< 300	Broad eclipses of nearly equal depth, can appear ellipsoidal, $P_{orb} < 1$ day	16
Flare Stars	10^{-3} - 1	M,K stellar spectra	< 100	Sinusoidal variations & flares on timescale of minutes, P_{orb} days	17
Coronal	10^{-6} - 10^{-3}	F,G stellar spectra	< 100	not variable in optical	16
Wind emission	10^{-6} - 10^{-4}	O,B stellar spectra	< 100	Irregular or none	16,21

[a] Average and standard deviation of reported EW ratios in Echevarria (1988)

[b] For systems where EW(Hβ) > 20 Å. This is not a definitive test, as it is based on tens of systems. The defining characteristic of IPs is an X-ray spin period for the WD that is less than the orbital period. Our X-ray observations are too shallow to permit detection of a spin period in most cases.

[c] Reported values are average of observed EW ratios for the systems A0620-00 and V404 Cyg in quiescence and outburst, respectively.

2. Observations

This chapter describes the different instruments used to make X-ray and optical observations, along with descriptions of the archival photometric databases. I also describe the spectrograph and spectroscopic data that I have personally reduced and used. The chapter concludes with a subsections on using the data acquired for analysis and interpretation.

2.1 X-ray Data

2.1.1 Chandra X-ray Observatory

The Chandra X-ray Observatory (CXO) is a focusing X-ray telescope sensitive to X-ray photons between 0.1 and 10 keV, which relies on a low grazing angle to reflect and focus incident X-ray photons from a cylindrical parabolic mirror. These focused photons then strike the instrument being used. The GBS observations consisted of 2 ks exposures using the AXAF CCD Imaging Spectrometer (ACIS) instrument on the CXO, which is sensitive between 0.2 keV and 10 keV. ACIS consists of 10 X-ray CCDs, of which our observations use the I0-I3 CCDs (Garmire, 1997). Within ACIS, incident X-ray photons strike the CCD, promoting many electrons above the Fermi gap in proportion to the energy of the photon. The CCD array measures the location of the photon as it is read out. Since the image is in focus, the position of the photon on the CCD chip measures the direction on the sky it came from. In the case of high X-ray photon flux, two or more photons may be counted as a single event with an energy equal to the sum of the indistinct photon energies. In effect, multiple low energy photons are measured as a single high energy photon. This photon pileup results in a distortion of the spectrum for the brightest sources.

The X-ray observations were collected and analyzed by Peter Jonker and others in Jonker

et al. (2011) and Jonker et al. (2014). X-ray sources in the survey area were initially found using the CXO. Pointings are constructed to avoid duplication with the *CHAndra Multiwavelength Plane* (CHAMPLANE) Bulge Latitude Survey (BLS) (Grindlay et al., 2010). Initial observations covered only 3/4 of the proposed survey area (Jonker et al., 2011), though the rest of the Southern portion of the survey has now been completed (Jonker et al., 2014). All X-ray sources are shown in Figure 1.3. In the original observations 1234 X-rays point sources were identified. An effort was made to screen for duplicate X-ray positions automatically before publishing the source catalog in Jonker et al. (2011), but using more conservative astrometric error estimates in Hong et al. (2005), 18 of the 1234 sources in the original catalog were found to be duplicates leaving 1216 unique X-ray sources (Hynes et al., 2012). When we include more recent observations of the remaining survey area, the total number of unique X-ray sources in the GBS amounted to 1640 (Jonker et al., 2014). The CXO sources identified in the first group of X-ray observations are officially named with the prefix "CXOGBS J" and the RA and DEC coordinates, but for ease of use, we refer to these with the prefix "CX" followed by an ID number given in descending order of X-ray brightness starting with 1. The sources in the second group of CXO observations are denoted with the prefix "CXB" and numbered in the same way, again starting with 1. This work will discuss both CX and CXB sources, with the majority focusing on the CXB sources.

The GBS catalog of X-ray sources includes only those with 3 or more photons observed in a 2 ks observation. For faint sources with so few photons, the X-ray spectrum is impossible to measure with any accuracy. We do have 93 CX and 27 CXB sources with 20 or more photons, which allows X-ray color to be measured as the ratio of the difference of soft X-rays (0.3 keV–2.5 keV) to hard X-rays (2.5 keV–8 keV) divided by the total number of counts, which is also known as the hardness ratio. If all photons are high energy, hardness is +1, while if all photons are in the low energy band, hardness is −1. The estimation of X-ray flux, F_X, we have for faint sources is uncertain by at least Poisson statistics which is $\propto \sqrt{N}$,

but have added uncertainties in assuming the shape of the X-ray spectrum of the source and the amount of absorption. To estimate the uncertainty in the photon count for each source, we use the method in Gehrels (1986) that $\sigma_{\rm N} = 1 + \sqrt{\rm N + 0.75}$. Assuming a power law spectrum with photon index $\Gamma = 2$ and hydrogen column density $\rm N_H = 10^{22}$ atoms $\rm cm^{-2}$, each photon corresponds to roughly 7.75×10^{-15}ergs $\rm cm^{-2}\,s^{-1}$ (Jonker et al., 2011). The power law of $\Gamma = 2$ is assumed because the spectral shape of a BH qLMXB softens as it decreases in luminosity from the low-hard state as the contribution from inverse-Compton scattering decreases, but reaches a plateau at $\Gamma = 2.08 \pm 0.07$ (Plotkin et al., 2013). Inverse-Compton scattering happens when a photon interacts with a high energy electron and picks up some of the electron's energy.

For other types of sources, the emission mechanisms are different and different spectral models are used to estimate a more accurate $F_{\rm X}$. If there is evidence from other wavelengths that an object belongs to a certain source class, I recalculate the $F_{\rm X}$ using one of these models with the WebPIMMS tool[1]. As an example, for IPs, the X-rays are produced by a curtain of material crashing onto the magnetic pole of a WD and emitting Bremsstrahlung radiation. CVs often have a soft, thermal X-ray spectrum so I use Bremsstrahlung radiation with a characteristic temperature of 25 keV.

For individual sources, we can use reddening maps from Gonzalez et al. (2012) for the X-ray source position to get a better estimate of $N_{\rm H}$ by using the relationship $N_{\rm H} = 5.8 \times 10^{21} \times A_{\rm V}$ atoms $\rm cm^{-2}$ in Bohlin et al. (1978) or $N_{\rm H} = 1.79 \times 10^{21} \times A_{\rm V}$ atoms $\rm cm^{-2}$ from Predehl & Schmitt (1995). The two relations are within errors of one another since $A_{\rm V} \approx 3.1 \times E(B-V)$. The values for these maps were derived from red clump stars (a position on the H-R diagram whose luminosity and color is more or less independent of metallicity or age) at the Bulge distance, while the actual X-ray source may be a foreground object rather than in the Galactic Bulge. These relationships therefore do not offer great confidence in estimating

[1]http://heasarc.gsfc.nasa.gov/Tools/w3pimms.html

the X-ray flux without some information on the likely absolute magnitude, and distance, of the object in question. It is also important to remember that, as discussed in Chapter 1, variations in the relative abundance of elements causes changes in the relationship between $E(B-V)$ and N_H between different lines of sight.

2.1.2 95% Confidence Region Error Circle

In order to match probable optical counterparts to the X-ray source positions from the GBS X-ray source catalogue of Jonker et al. (2014), we calculated the 95% confidence region error circle using the equation:

$$\begin{aligned} P_{\rm err} = 0.25'' + \frac{0.1''}{\log_{10}(c_{\rm n+1})}\left[1 + \frac{1}{\log_{10}(c_{\rm n+1})}\right] \\ +0.03''\left[\frac{D_{\rm offset}}{\log_{10}(c_{\rm n+2})}\right]^2 + 0.0006''\left[\frac{D_{\rm offset}}{\log_{10}(c_{\rm n+3})}\right]^4 \end{aligned} \tag{2.1}$$

from Hong et al. (2005). Here, $P_{\rm err}$ is the 95% confidence positional error expressed in arcseconds. The term $D_{\rm offset}$ is the Chandra off-axis angle and $c_{\rm n}$ are the number of X-ray counts collected per source from Chandra. Given that this is a 95% confidence error circle, this means that 5%, or 1 out of every 20 sources, may lie outside the calculated error circle. The error circle was then plotted over the appropriate image and examined to see whether there is an optical counterpart visible that would coincide with the detected X-ray source.

2.2 Photometric Data

2.2.1 DECam

The GBS area has been observed in the optical several times since 2010. Britt et al. (2014) describes the Mosaic-II observations in detail and will not be covered here. Instead, we focus on the observations acquired using the Dark Energy Camera (DECam) on the 4.0 m

Blanco telescope at the National Optical Astronomical Observatories' (NOAO) Cerro Tololo International Observatory (CTIO). The first observing run took place in 2013 with 2 nights imaging the southern strip of the GBS area in the SDSS r' band. The second observing run took place in 2014 and also consisted of 2 nights covering the northern strip of the GBS area in the SDSS i' band. The analysis in this dissertation focuses on 374 sources in the southern strip and 50 sources in the northern strip for a total of 424 sources.

We used 2 nights in June of 2013 with DECam to measure optical variability in the r' band which covered the magnitude range $12 < r' < 23$. I accompanied my advisor Robert Hynes to CTIO to collect this data. I was a Co-investigator (Co-I) on this proposal which was given the PropID of 2012B-0617 and titled *Classifying X-ray sources from the Chandra Galactic Bulge Survey.*

I successfully proposed for the 2014A semester to gather variability information on the northern strip of the GBS using the i' band. This proposal was titled *Completing the DECam View of the Galactic Bulge Survey* and given the PropID of 2014A-0399.

We observed with DECam on the CTIO Blanco 4.0 m telescope from June 10 to June 11, 2013 in the SDSS r' band. We imaged the southern strip of the survey covering ∼800 X-ray sources, of which I will be focusing on the 374 CXB sources. The SDSS r' images comprised of 2×90 second followed by 2×1 second exposures to account for the faint and bright sources in the field, along with bias and flat field images for calibrating. The second observing run took place from June 30 to July 1, 2014 in the SDSS i' band on the CTIO Blanco 4.0 m telescope using DECam. In a similar manner, the SDSS i' images comprised of 2×90 second followed by 2×1 second exposures. The i' data set contains 50 sources that were analysed. The complete data set consists of 424 unique sources. The images were calibrated using the *American Association of Variable Star Observers* (AAVSO) Photometric All-Sky Survey DR7 (APASS) and carry an average calibration uncertainty of 0.05 magnitudes. The

data were reduced with the NOAO DECam pipeline and were acquired through the NOAO science archive.

DECam has a pixel scale of 0.27 arcsec/pixel. The pixels are 15 μm in size with a gain of 4 e^-/ADU and readnoise of 7 e^- RMS. The CCDs remain linear up to ∼50,000 ADU and begin to saturate around ∼65,000 ADU and have a readout time of 20–30 seconds between pointings. DECam is a honeycomb shaped mosaic of 62 science CCDs, 8 wave-front sensing CCDs, and 4 guide CCDs and pre-amplifiers. The imager covers a field of view (FoV) of 2.2 degrees using $2K \times 4K$ CCDs totalling 520 million pixels with small gaps (∼150–200 pixel) between chips.

The projected DECam pointing with the X-ray sources overlayed is shown in Figure 2.1. We used 8 pointings to cover the entire GBS survey area, 16 with dithering. We dithered our observations between cycles to observe targets that may have fallen on chip gaps in one or the other pointings. We labeled each of the pointings as 1A, 2A, 3A and 4A with the dithered pointings being 1B, 2B, 3B and 4B for both the northern and southern strips in Figure 2.1. We cycled through each field randomly each night (which included dithers) to prevent aliasing the period with our duty cycle. The aliases result from the sampling frequency and the intrinsic frequency causing unwanted beat frequencies in the data. Sources most often have an average of 45 observations per night with the lowest being 10 observations (which is rare) and the highest being 109 observations per night.

Most sources have 1" X-ray localizations and candidate optical counterparts, many of which are already known to be variable. The existing partial coverage variability survey of the GBS, performed originally with the Mosaic-II instrument (Britt et al., 2014), identifies many sources as variables with no clear period. This was from a typical sampling of 2–5 observations per night, enforced by the relatively small field of Mosaic-II. With the use of DECam's FoV of 2.2 degrees, one survey strip area can be covered in 4 pointings as opposed to 64 with Mosaic-II. This increased our sampling rate from 2-5 times to 28-56 times per target

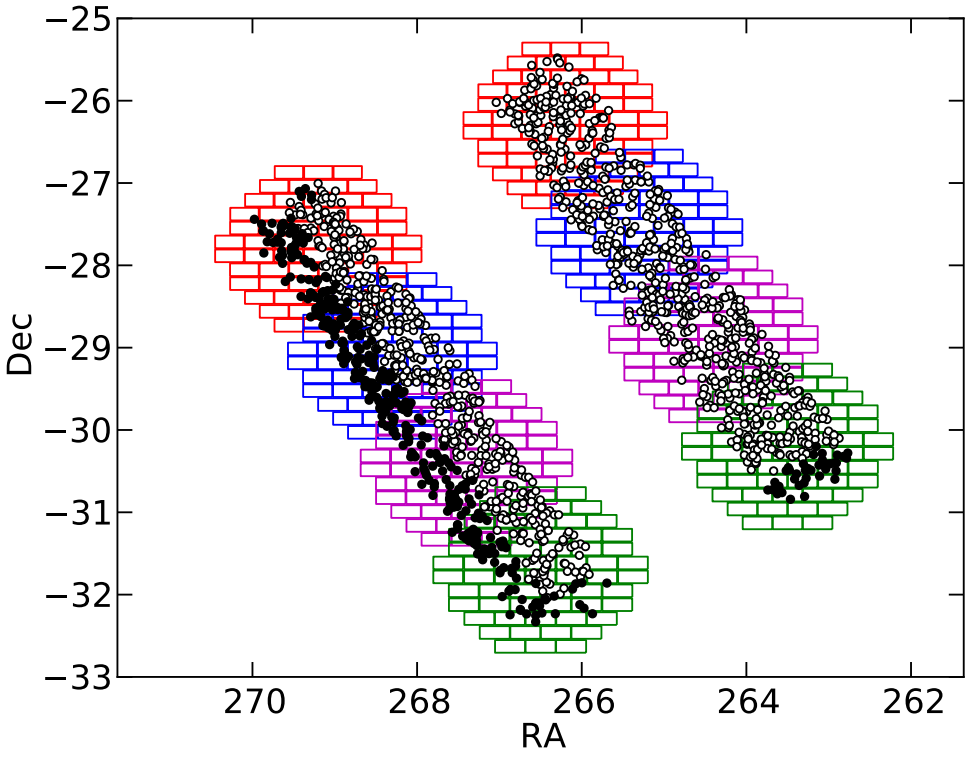

Figure 2.1: Pointings for the June 2013/2014 4.0 m DECam observing runs. The two "strips" are denoted as the northern and southern strips.

per night (on average), which includes dithering and dramatically improves our sensitivity to short period binaries. The data acquired already demonstrates a vast improvement on the detectability of short-period variables compared to the Mosaic-II data. As an example, we show the comparison light curves of CX44 using the Mosaic-II and DECam photometry in Figure 2.2.

2.2.2 SMARTS 0.9 m

For the GBS source CX514 (see Chapter 5), we obtained data from the 0.9 m *Small and Moderate Aperture Research Telescope System* (SMARTS) telescope at CTIO. We carried out the observations from June 1 to June 7, 2012. The telescope is equipped with a $2K \times 2K$

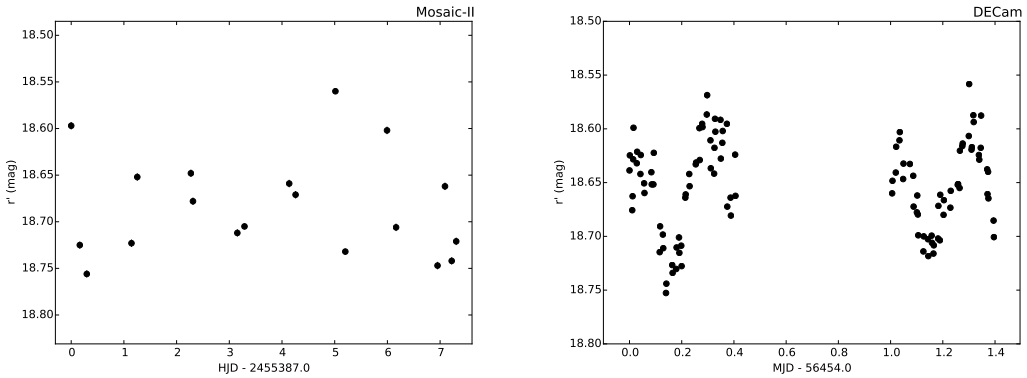

Figure 2.2: A comparison of the Mosaic-II and DECam data for the GBS source CX44 showing an ellipsoidal modulation which was not seen in the Mosaic-II data.

pixel CCD and a pixel scale of 0.401 arcsec/pixel. The data is read out by an amplifier at each of the 4 corners of the chip. Each amplifier has a slightly different gain which also depends on gain index selected. We used index 2 to reduce readout time from 53 seconds to 32 seconds. The gain values of the amplifiers are, on average, 2.6 e^-/ADU with this index. The CCD saturates at $\sim$ 65000 ADU.

2.3 Online Archival Data

2.3.1 ASAS-3

We obtained archival photometry from the All-Sky Automated Survey (ASAS-3) (Pojmanski, 1997) which uses a combination of two wide-field telescopes, each equipped with 200/2.8 Minolta telephoto lens and 2K×2K AP-10 CCD cameras located at the Las Campañas Observatory (LCO) in Chile. The telescopes cover 8.8°×8.8° of the sky through the V and I filters and the FoV is 2.2°×2.2°. The ASAS-3 telescopes each have an exposure time of 180 seconds imaging the southern hemisphere with dec $< +28$ degrees, which is approximately 10^7 stars brighter than 14 magnitude. The data available for each object in the ASAS database are graded on a scale from A–D, with A being the best quality. When using the

ASAS-3 catalogue, we always performed our final analysis using data that had a grade of either A or B.

2.3.2 OGLE-IV

The online database from the *Optical Gravitational Lensing Experiment* (OGLE) (Udalski et al., 2012) has provided us with archival photometry for several of our sources in the GBS survey. OGLE is an optical monitoring program originally aimed at searching for dark matter with microlensing phenomena. The Magellanic Clouds and the Galactic Bulge are the most natural locations to conduct such a search due to the large number of background stars that are potential targets for microlensing. Over the years, OGLE has had upgrades to the CCDs and telescopes used. Now, OGLE is in its fourth phase (OGLE-IV) using the 1.3 m Warsaw Telescope at Las Campañas Observatory in Chile. The CCD has a 32 chip mosaic camera with thin $2K \times 4K$ pixels per chip and a 0.26 arcsec/pixel scale and $1.4^\circ \times 1.4^\circ$ FoV. The telescope is fully automated and scans the sky in the standard V and I-band filters with a magnitude limit between 13–21 in the I-band and exposure times of 150 seconds each.

Udalski et al. (2012) have presented a catalogue of 209 variable objects which are very likely (and in several cases have been shown to be) optical counterparts to the X-ray sources detected in the GBS. The optical counterpart candidates were searched based on the X-ray source position with a radius of 3.9". Udalski et al. (2012) provide the astrometric and photometric information for all selected objects and their preliminary classifications. Photometry of the candidates is available from the OGLE Internet archive.

2.4 Historical Plate Archives

For the CV evolution project outlined in Chapter 6, the use of archival magnitudes is crucial in establishing long term light curves with $\sim$100 year timelines. Several plate archives

exist around the world with plates dating back to the late 1800s for which telescopes and astrographs have imaged large portions of both the northern and southern skies. Described below are two such plate archives in which data were obtained, analysed, and published in Johnson et al. (2014a). The comparison stars that we used for magnitude comparison all had modern B-band magnitudes from the APASS survey, so the derived magnitudes are all approximately in the Johnson B magnitude system. All the plates are in the B magnitude system (they were the original source for the definition of the system) with an essentially zero color term.

2.4.1 Harvard College Observatory Astronomical Plates

The collection of astronomical plates at the Harvard College Observatory (HCO) contains ∼500,000 plates taken between the mid 1880s and 1989 (with a gap from 1953-68). The majority of these are direct blue plates, taken with a variety of refractors having focal scales of 60-600 arcsec/mm. Coverage is excellent in both hemispheres of the sky, with the southern hemisphere having perhaps the advantage. A few thousand direct plates, mainly blue, were taken with the 1.5 m reflectors located in both northern and southern hemispheres. These have a focal scale of 26 arcsec/mm.

We have measured (or searched for) all the B-band magnitudes at HCO for the CN V603 Aql (see Chapter 6). These plates cover the years from 1889–1989. The plates used from HCO consisted of the RB Patrols, DSB and DSR Damons, AM/AK/AX and B plates with limiting magnitudes quoted[2] as 15, 15, 12–14 and 17, respectively. The 1σ measurement uncertainty is ∼0.15 mag on average for these plates.

[2]http://tdc-www.harvard.edu/plates/plates.html

2.4.2 Sonneberg Astronomical Plates

The astronomical plates contained in the Sonneberg Astronomical Observatory (SAO) number around 240,000 and date from the mid 1880s to about 2013. A combination of astrographs and Schmidt telescopes comprise the majority of the plates each with a FoV between $3.8^\circ \times 3.8^\circ$ and $26^\circ \times 26^\circ$. These plates are also direct blue plates in the B-band system with plate limits between 13.5 and 18.5. The plates used for the analysis of V603 Aql span the years 1934–2004 and all have near-zero color terms to correct for. The 1σ measurement uncertainty is $\sim$0.15 mag on average for these plates as well.

2.5 Liverpool Telescope Spectroscopic Data

I have also examined optical spectra of one selected counterpart to a GBS source, CX514, using the 2.0 m unmanned fully robotic Liverpool Telescope at the Observatory del Roque de Los Muchachos on the Canary island of La Palma, Spain. This analysis has been published in Johnson et al. (2014b).

A star's spectrum can be extracted in multiple ways, most commonly and in this work, by laying a slit across the field to isolate light from stars of interest on one axis on the CCD, then splitting that light into different colors with a diffraction grating or grism. The second axis on the CCD is then composed of different wavelengths of light. Some instruments select stars with optical fibers placed over the star, leading the light to a CCD. These instruments have the advantage of being able to observe multiple targets that are not in a straight line.

Spectra were collected using the *Fibre-fed RObotic Dual-beam Optical Spectrograph*, or FRODOspec instrument[3]. CX514 was observed with both the blue-high grating with a wavelength range of 3800–5150 Å and the red-high grating with a wavelength range of 5700–8050 Å. The dispersion in the blue range is 0.35 Å/pixel with a resolution of 0.8 Å at the central wavelength of 4495.6 Å. The dispersion inherent in the red range is 0.58 Å/pixel with

a resolution of 1.3 Å at a central wavelength of 6827 Å. Exposure times on both sets of observations were 300 seconds each. The spectra were reduced by using two sequentially invoked FRODOspec pipelines. The first pipeline, known as the L1, is a CCD processing pipeline which performs bias subtraction, overscan trimming and CCD flat fielding. The second pipeline, known as the L2, performs the spectroscopic data extraction. The wavelength calibrated spectra have a final accuracy of 0.08 Å. The spectra were then normalized with standard IRAF tools and packages by dividing by a spline fit to the continuum of order 10. The FRODOspec pipeline and instrument specifications are described in detail online[3].

2.6 DECam Analysis

2.6.1 Optical Data Reduction

CCDs are an important tool in astronomy but also many other areas of science and technology. They operate by having a grid of electrodes held at alternating potentials creating charge trapping potential wells next to a semiconductor. When a photon of an energy greater than the Fermi gap strikes the semiconductor it promotes an electron. The electrons are held in the potential well of one of the electrodes, which constitutes a single pixel. At low numbers of electrons, the CCD responds linearly to new photons; twice the photons yields twice the electrons. Once the number of electrons begins to "fill" the potential well of the pixel, however, the response of the CCD weakens and becomes non-linear. Eventually, the potential well of the pixel fills and no more electrons are held. These pixels are said to be saturated. If electrons continue to be promoted in a saturated pixel, they will "bleed" into nearby pixels. The CCD is read out through an amplifier by one column at a time as charge is transferred along the row to the edge of the chip, so the electrons bleed on this axis, forming "bleed trails" when enough overflowing electrons saturate pixels on the same row as the saturated

[3]http://telescope.livjm.ac.uk/Info/TelInst/Inst/FRODOspec

star. The bleeding is constrained to the direction of readout because of insulating layers in between rows.

As with all instruments, CCDs leave a signature on the data that needs to be removed to perform any meaningful analysis. In order to keep a CCD's readout positive, a bias voltage is applied during readout. This value often changes with both time and position on the CCD. To account for the time component, it is common practice to continue reading a CCD out beyond the point when all the data has been collected. This gives a few (usually 16 or 32) extra columns of readout that can be fitted to an nth order polynomial to keep track of changes over time. These extra columns are called the overscan region. To account for position dependence, one can read out the whole CCD without exposing it first. We call this a bias frame.

Electrons can also be thermally excited above the Fermi gap in the semi-conductor used in CCDs (usually silicon) due to random thermal fluctuations. This "dark current" accumulates with time, making it proportional to exposure time. Some pixels ("hot pixels") are more easily excited than others, and this current must be measured and subtracted from each data frame. The DECam instrument, however, is cooled with liquid nitrogen and the dark current is so small ($\leq 2\ e^-\ \mathrm{pixel}^{-1}\,\mathrm{s}^{-1}$) that it can be safely neglected for our 90 s exposures.

The light passing through the telescope is also altered by imperfections and dust on the filter and CCD window. Imperfections on the primary mirror do not actually leave any residual on the image at all, since it is exactly out of focus so the effects are spread out evenly across the image. These effects are multiplicative, and are removed by dividing the object frames by a flat field, which is an exposure of an evenly illuminated screen inside the dome of the telescope or of the twilight sky.

NOAO uses a data pipeline to reduce all the object frames from DECam which makes use of bias frames and flat fields taken during each night of observation (Valdes et al., 2014). It uses calibration files available online to correct for cross-talk between CCDs, ghost-pupil

images, and patches of bad pixels on the CCDs with the use of bad pixel masks known as data quality masks. It also applies a World Coordinate System (WCS) solution to images and roughly estimates the zero-point magnitude based on USNO-B1.0 stars in the field. Since the CCD is so large, there are optical distortions at the edge of the FoV, which is also corrected for in the pipeline. As such, the final pipeline product is a reprojected image, where the pixels are not the original CCD pixels, but are square on the sky.

Each reprojected DECam image contains over $30K \times 30K$ pixels, varying slightly in size with atmospheric refraction corrections applied by the pipeline. In order to save on computation time, I used the WCS in each image to cut out postage-sized stamps around each X-ray source. When we started photometry, we used stamps that were 400×400 pixels. In cases where the stellar field suffered from from very few comparison stars, larger stamps were needed to model atmospheric changes between observations. To organize the large amount of data used by several people, the data for each source was placed in its own subdirectory. Since I was the only one analyzing the 424 sources in my sample and creating light curves, I kept my own log file with descriptions for each source.

3. Stellar Variability

Over the course of the night, the observed brightness of each star changes as the stars rise and set, as the light must travel through changing amounts of air which leads to some atmospheric extinction of light. The amount of air that light must travel through to reach the telescope is measured by the airmass, which is simply expressed as $a = \sec z$, where z is the angle between the star and the zenith. This formulation assumes a flat and infinite Earth, and therefore incorrectly approaches a limit of infinity at the horizon. This prescription is acceptable for the altitude angles at which the telescope operates, which do not extend above an airmass of 3 because of the mechanical limitations of safely operating the Blanco 4.0 m Telescope.

Changes in the weather also change the amount of light seen by each star, as dust and water vapor in the air can reduce the transparency of the atmosphere. Also, the atmosphere can become more or less turbulent as the night progresses and from night to night. Pockets of turbulence in the air move and refract the starlight in different amounts, scattering the light and causing the familiar "twinkling" which is characteristic of starlight. Over a long exposure, these changes in refraction build up to form a roughly Gaussian distribution of light, called the Point Spread Function (PSF). The spatial Full Width at Half Maximum (FWHM) of the PSF is called the seeing and determines the maximum resolution possible for a given observation. The term "good seeing" means the light is more focused on a few pixels, whereas "bad seeing" means the same amount of light from a star is widely distributed across a much larger area causing a smearing out of the PSF. Bad seeing increases noise in an observation due to the fact that more crowding with adjacent stars will cause the PSFs to blend and makes it much more difficult to distinguish fainter stars from the background sky since the peak intensity of the star is reduced. The worse the seeing gets, the more sky

pixels show up in the aperture causing more Poisson noise. Figure 3.1 shows images of the same field from observations in both good and bad seeing.

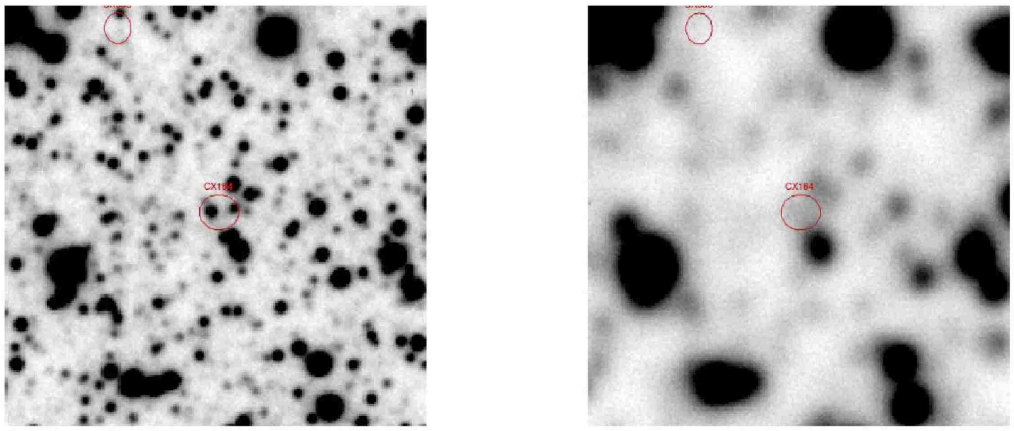

Figure 3.1: Left, the area around one of the X-ray sources in good seeing. Right, an observation of the same field in significantly worse seeing; many previously distinct stars are blended together or altogether lost to the eye as they are swamped by light from the sky and nearby brighter stars.

The changes in seeing affects all stars differently. For example, atmospheric extinction is stronger in the blue end of the spectrum so a bluer star suffers more extinction. We refer to this scenario as "differential extinction" where precise corrections need to be taken in to account, i.e. the color-extinction cross terms.

3.1 Image Subtraction with HOTPANTS

In order to uncover variability and track changes in brightness of the stars within our computed 95% confidence region, we used an image subtraction software package written by

Andrew Becker called the *High Order Transform of PSF ANd Template Subtraction*, or HOTPANTS[4]. The code incorporates an implementation of the Alard & Lupton (1998) algorithm but contains a variety of changes and improvements. To solve the difference imaging problem, we must find a convolution kernel, K, that matches the PSFs of two astronomical images, I (which is referred to as the image) and T (referred to as the template). The images are generally taken under different conditions which include atmospheric transparency, seeing or a mixture of exposure times. Mathematically we want to minimize the function:

$$\sum([T * K](x, y) - I(x, y))^2 = 0 \tag{3.1}$$

by solving for the kernel K. If K can be decomposed into basis functions, then we have a linear least-squares problem which can be solved uniquely by matrix inversion. In this method, the kernel is decomposed into Gaussian basis functions

$$K(u, v) = \sum_n A_n K_n(u, v) \tag{3.2}$$

$$K_n(u, v) = e^{(u^2+v^2)/2\sigma_k^2} u^i v^j \tag{3.3}$$

where i and j are the orders of the spatial variations of the Gaussian and n is the number of Gaussians used in the convolution. By default, HOTPANTS uses $n = 3$ and

$$\sigma_{k1} = 0.7 \text{ pixels}; \quad i + j \leq 6 \tag{3.4}$$

$$\sigma_{k2} = 1.5 \text{ pixels}; \quad i + j \leq 4 \tag{3.5}$$

$$\sigma_{k3} = 3.0 \text{ pixels}; \quad i + j \leq 2 \tag{3.6}$$

[4]http://www.astro.washington.edu/users/becker/v2.0/hotpants.html

With this prescription, an initial kernel is fit with a narrow Gaussian that is allowed to vary to a high spatial order, a broader middle Gaussian varying at a lower spatial order and a wide Gaussian that varies at very low spatial order. We have found that these defaults are not optimal for our DECam images and depend on the average PSF of stars in our images. As a rule of thumb, we set the three Gaussians to approximately the best, medium and worst seeing in our images before running the code. HOTPANTS divides the image up into multiple regions and fits for one convolution kernel within each region. Each region is then divided up into stamps, generally 1 per every 100 pixels (a 2000×4000 pixel image has 20×40 stamps). Due to the size of a single DECam image (∼1.2 Gb), we found that our images were optimal when using a 400×400 pixel (∼1.8 arcmin^2) area of the image and that 5×5 stamps worked the best. Within each stamp, multiple sub-stamps are centered on the individual astronomical objects. Constraints are then placed on the kernel in each stamp (such as using a 3×3, 5×5 or higher matrix depending on the size of the sub-stamp in each region and also the size of the original image). Since a spatially varying function is being fit, we want to try and ensure constraints across the entire image especially at the edges. This is not imperative for the majority of our images since our targets are placed in the center of our stamps.

Data quality masks are fed in to the code which allow it to avoid bad pixels while looking for sub-stamps. This masks allow HOTPANTS to distinguish between completely bad pixels which should be ignored (such as saturated pixels), pixels which might be trusted but do not want to use while fitting for the kernel (such as interpolated pixels) and pristine untouched pixels. The masks are convolved and may be output from the software to be used in subsequent stages of the processing (e.g. differential photometry) that are designed to take advantage of this information.

After the convolved reference image is matched to a subsequent image, the two are subtracted creating a difference image of residual pixels. The residuals should be due to

changes in magnitude of variable stars in each image. Stars of constant brightness should subtract out cleanly. Variables can be easily spotted by creating a variance image of the residuals from each difference image which looks at the spread (or dispersion) of the pixel values around the mean pixel values. An example of a reference image and variance image is shown in the left and right panels of Figure 3.2.

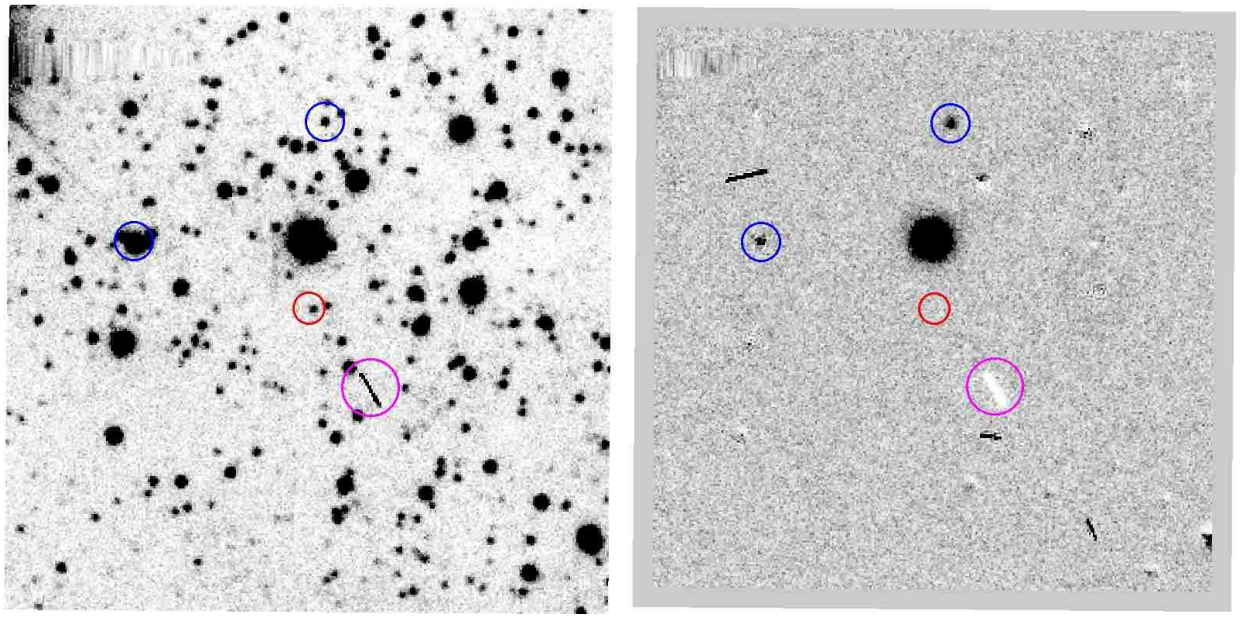

Figure 3.2: An example of a reference image (left) and variance image (right) of one GBS source. The red circles represent 95% confidence region error circles, the magenta circles identify a cosmic ray in the image and the blue circles are random variables in the FoV. The images are 1.35' on a side, North is up and East is left.

Objects can appear to be variable in the variance image when they are not for several reasons. First, non-linear or saturated stars a) do not transform with seeing in the same way that the rest of the sky does and b) have a significant amount of light scattered beyond the edge of the calculated PSF. The latter is usually a problem in bad seeing, but can be corrected by either increasing the size of the transformation kernel or by limiting the observations to those with good seeing. Second, apparent cosmic rays and CCD defects can also cause spurious detections of variability. Third, although the data reduction pipeline

operated by NOAO attempts to correct for it, the cross-talk between CCD chips adds a low amplitude copy of the chip, which is most obvious in the "ghosts" of saturated stars on adjacent chips. These ghosts manifest as marginally higher background in a localized area whose location depends upon the orientation of the CCD and pointing of the telescope.

While working on optimizing the HOTPANTS parameters for the images, we came across difference images that have residual structure that resemble lobes of bright and dark pixels. These structures are referred to as "dipoles" and apparently manifest themselves through differential chromatic refraction (DCR). Photons from the same source but different wavelengths that pass through the same filter of a telescope will have slightly different degrees of refraction and appear to land on different locations of the CCD. The blue photons from a source are refracted the most causing these dipoles. For the r' band, stars will exhibit DCR of > 5 mas at parallactic angle differences > 20 deg[5]. In most cases, the variability of an object is greater than the size of the dipole and shows up as a spherical object in the difference images. Originally, photometry was going to be performed on the subtracted images. When the problem of DCR appeared, we decided to perform aperture photometry on the initial images and use the subtracted images as a visual quick-look for variability.

3.2 Photometry

The first check on whether an object is variable is whether it shows up, shaped like the PSF, in the variance image. These checks are done first by eye after HOTPANTS is run and the variance image is created. If there appears to be an object in the variance image, then we do a check of all the images used in making the variance image to make sure there is nothing falsely contributing to the variability. Several factors that we have come across are artifacts in the chips, cosmic rays landing directly on the target or even asteroids entering the FoV

[5]https://jira.lsstcorp.org/browse/RFC-112

passing in front of the target. If the variability seems genuine, then we make a lightcurve and try and interpret the data.

There are two methods of estimating the magnitude of the source in the reference image: PSF fitting and aperture photometry. The PSF fitting technique uses models such as a 2D Gaussian or Lorentzian function to fit to the PSF of each stellar object. We first build up the PSF by examining several bright stars in the field and then apply the model to our target while subtracting off the background. A very widely known and heavily used task within IRAF[6] called DAOPHOT II uses PSF fitting to estimate magnitudes of individual stars (Stetson, 1987).

The second technique, aperture photometry, will be employed throughout this entire work (except in regions where extreme crowding is an issue and PSF fitting is better suited). Aperture photometry relies on summing the pixel counts within an aperture centered on the star and subtracting the nearby average sky count per pixel and the number of pixels within the aperture. This will result in the raw flux value of the target object which can then be converted to a magnitude and calibrated using the zero point magnitude provided in the header of the image. The fluxes and magnitudes were extracted using the PHOT task in IRAF along with several other tasks including TXDUMP. The photometry routine was automated using my own scripts wrapped around IRAF tools (known as PyRAF) primarily in the PYTHON language. PYTHON is an object-oriented (OOP) scripting language used in many scientific disciplines and has gained a large following in the past decade due to its ease of use and adaptability. The routine does aperture photometry on the target source and at least three different comparison stars in the field to acquire the flux. Then, the instrumental magnitude is calculated and calibrated using either the APASS photometric

[6]IRAF is distributed by the National Optical Astronomy Observatory, which is operated by the Association of Universities for Research in Astronomy (AURA) under cooperative agreement with the National Science Foundation.

standards in the FoV or, in some cases, using the Carlsberg Meridian Catalog 15 (Niels Bohr Institute et al., 2014).

The zero point in the image header is only as accurate as the magnitudes of the fainter stars in the USNO-B1.0 catalog, which are good to ~ 0.5 magnitudes. This does not affect the relative magnitude of data points, only the zero point.

To check that the variability in the light curve is significant, we compare the size of the statistical error bars on each data point to the Root Mean Square (RMS) of the variations in the light curve. Sources that show variations unattributable to statistical noise at the 3σ level are considered variable. Sources with a single observation in outburst or in eclipse are considered significantly variable if the observation in question is 4σ above the mean magnitude and the images do not contain artifacts leading to false variability. The variability criteria for my data set was borrowed from Britt et al. (2014) where they had success in distinguishing between variable and non-variables over an 8 day baseline.

3.3 Period Determination

To search for periodicities in a lightcurve, we use the Lomb-Scargle statistical technique employed in the software package Starlink PERIOD[7], which is better for irregularly sampled data than Fourier analysis. PERIOD is a time-series analysis package designed to search for periodicities in data sets using different analysis techniques. To be considered significant, the candidate period must have a higher power than 99.73% (3σ) of the generated Lomb-Scargle searches at *any* frequency to fairly account for the number of trials used. For most of the searches we ran, the frequency range of 0.5–1000 cycles per day was used with a sampling frequency of 0.0001 cycles per day to account for short period systems ≤ 2 days.

An example of a periodogram is shown in Figure 3.3. The fundamental frequency is

[7]http://www.starlink.rl.ac.uk/

denoted with the letter "f" with the second harmonic being "2f". Several longer frequencies are present labelled as "fs" and "fr".

Binary systems can show ellipsoidal modulations and have an apparent period 1/2 that of $P_{\rm orb}$ or, in other words, they can be periodic at $f_{\rm orb}$ with most of the power in the first harmonic ($2f_{\rm orb}$). The maxima and minima of ellipsoidal variations are often asymmetric with phase due to the orientation of the system in the orbital plane relative to the line of sight. This situation happens because of the presence of a hotspot and gravity darkening which could be counter-balanced by X-rays heating the side of the companion facing the compact object. Star spots are most likely single peaked, but can show variations of the same character as ellipsoidal modulations. If the period seen in the periodogram is $P_{\rm ellip}$, then the phase-folded lightcurve should show some bimodality, where the lightcurve seems to split and follow 2 paths until rejoining, then splitting again.

In cases where lightcurves can be easily modeled by either a single sine wave (or 2 with a 2:1 period ratio for the case of assymetric minima and maxima) or a parabolic function (when calculating times of mid-eclipse), the errors on the period are calculated through χ^2 analysis. To find the best fit function, we look at the reduced chi squared statistic, $\chi^2_{\rm red}$, and the number of degrees of freedom, ν. The relationship can be seen in Equation 3.7:

$$\chi^2_{\rm red} = \frac{\chi^2}{\nu} = \frac{\sum_i^n \frac{(x_i - x_{\rm mod})^2}{\sigma_i^2}}{\nu} \tag{3.7}$$

where x_i and $x_{\rm mod}$ are the observed and model fit data, respectively. The i and n are the beginning and ending data points and the σ_i is the ith data point error. When the errors on the data are known *a priori*, a good fit for a specific function results in $\chi^2_{\rm red} \sim 1$, whereas a $\chi^2_{\rm red} \gg 1$ is a poor model and $\ll 1$ indicates that the data was not fully captured in the function. For a Gaussian distribution of errors, the 1σ confidence region of a single variable occurs when the χ^2 statistic increases by 1.

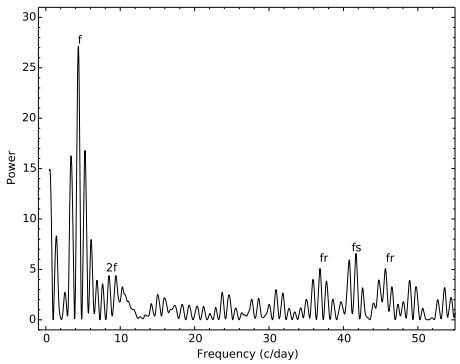

Figure 3.3: An example of a Lomb-Scargle periodogram for CX73. The fundamental frequency is denoted with the letter "f" with the second harmonic being "2f". Several longer frequencies are present labelled as "fs" and "fr".

For light curve morphologies that cannot be easily modeled (such as flickering), I use a bootstrapping method with a Monte Carlo approach to estimate errors on the period. The target data set is copied N times by randomly selecting data points. The data points are allowed to be resampled more than once during the sampling. This results in a data set with some repeated and omitted data points and reduced information. Each data set "copy" was then subjected to fitting an appropriate function to the data and allowing the parameters to vary. The distribution of the resulting fits to the new data sets is the same as the error distribution of the full data set. For calculating the error on the period, I make a new periodogram for each "copy" and calculate the error in the period based on the FWHM of the distribution of periods found. An example of this method is described in detail in Hynes & Britt (2012).

3.4 Variability of Optical Counterparts to GBS Sources

Several types of variability were uncovered during the course of this observational campaign. I have examined all the optical images available for the 424 CXB sources which is comprised

of 374 sources in the southern strip and 50 sources in the northern strip. Fifteen of these sources are spectroscopically analysed in Wu et al. (2015) giving approximate spectral types. Sixteen sources are coincident with $TYCHO-2$ stars (Hynes et al., 2012) and are brighter than $V = 12$. The sample contains 16 saturated stars or stars coincident with a saturated source and this includes nearby bright stars with bleed trails obscuring the target inside the error circle. The saturated subsample overlaps with 12 of the bright $TYCHO-2$ stars from Hynes et al. (2012). Of the 408 sources remaining, 29 contain no visible counterpart with a limiting magnitude of $m_{r'} > 23$, 142 contain visible counterparts within the error circle but are non-variable, and I find a total of 237 sources with some degree of variability.

3.5 Overview of Variability

The sources have been subjected to image subtraction using HOTPANTS (as described in Section 3.1) followed by generating light curves through aperture photometry on the original images. After a preliminary visual inspection of each light curve, I use the following labeling scheme to classify a variable:

Ell = ellipsoidal variations

Ec = eclipsing binary

LPV = long period variable, i.e. longer than our baseline of two days

Flare = flaring events

Per = a periodic type variable that does not fit the other categories

Flick = flickering in the light curve

NC = no visible counterpart within the error circle

NV = a non-variable within the error circle

V = variable star

S = saturated star

The sensitivity of optical variability is quite high and is evidenced by the detection of amplitude changes on the order of hundredths of magnitudes for many of the sources between $11 < r' < 19$. Sensitivity declines and scatter is more apparent for sources between $21 < r' < 23$ especially on the second night of observing where the seeing declined for $\sim$40 minutes towards the end of the night. Variations for which I was unable to recover a period or that comprise aperiodic fluctuations are the type of variability I refer to as "flickering". Out of 237 sources showing variability, about 3/4 show evidence of flickering in the light curve.

Some variable sources will inevitably lie outside the Chandra 95% confidence region, especially when the sample consists of hundreds of objects. In this sample, approximately 21 true counterparts should lie just outside the confidence region with $\sim$12 true variable counterparts falling outside the confidence region based on the observed rate of variability corrected for the absence of a counterpart. Variables showing DN outbursts or morphology similar to CVs or LMXBs would be considered the optical counterpart to the X-ray source if it lies outside the 95% confidence region but close to it.

Some systems will possess more than one of the variable characteristics (such as a long period system having a small flare or flickering), but I use whichever designation is more appropriate for the morphology of the light curve. The breakdown of the presence of counterparts and variability is illustrated in the pie charts in Figure 3.4. The full list of sources with variable counterparts are listed in Table 3.1 with details on each source. The range of $\frac{F_{\rm x}}{F_{\rm opt}}$ (see Section 3.6) accounts for the absorbed and unabsorbed (i.e. 1.0–2.0) flux ratio assuming Bulge distance using the assumptions from Jonker et al. (2011). I use the extinction law of $\rm R_V = 3.1$ from (Cardelli et al., 1989) and the relation between optical extinction and hydrogen column density of Bohlin et al. (1978): $N_{\rm H} = 0.58 \times 10^{22} \times A_V$ atoms cm^{-2}. For the Bulge extinction values, I use the extinction maps from Gonzalez et al. (2011). I then transform these values in to the Sloan r' filter using the properties set forth in Schlegel et al.

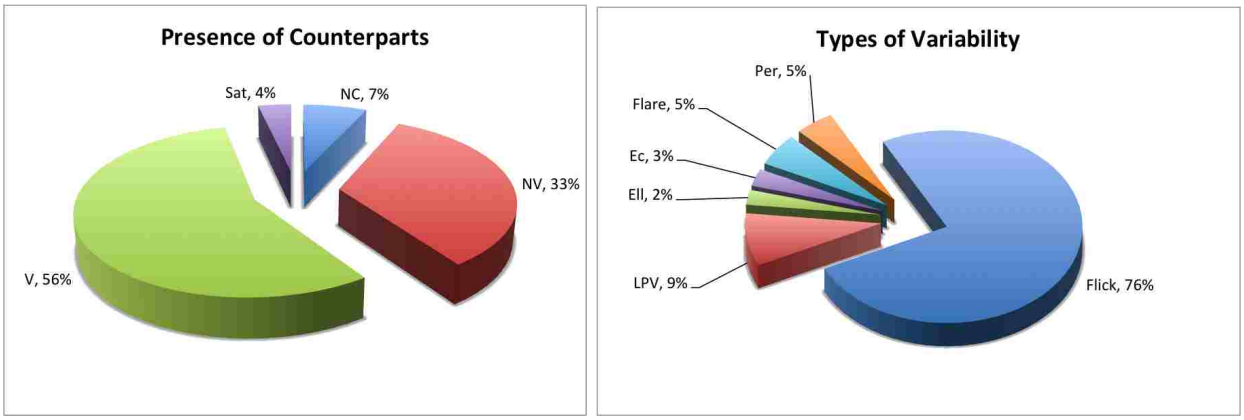

Figure 3.4: Pie charts describing the CXB source statistics. The left chart shows whether a source has a counterpart whereas the right chart shows the type of variability seen in the light curve. The legend for the pie charts is described above in the beginning of Chapter 3.4.

(1998). The optical flux is calculated using Equation 1.7 and the average r' magnitude, $m_{r'}$, from the light curve. Since I do not have exact distances on every source in my sample, the estimated unabsorbed and absorbed flux ratios represent lower and upper limits.

I find that 29 sources have no possible counterpart in the Sloan r'-band where predictions made in Jonker et al. (2011) place this number at 130 sources without an optical counterpart. The predicted number of real counterparts is much higher than that observed for the sample of 424 sources. Sources with large off-axis angles admit larger error bars and the possibility of many counterparts although the true counterpart may be below the limiting magnitude. The average 95% confidence region is $\sim$2.7" based on all the calculated confidence regions for each source. There are 141 sources with an estimated confidence region larger than 3" and 283 with confidence regions less than 3". We greatly improved the number of saturated sources (4%) compared to the previous survey of Britt et al. (2014) (21%). This was achieved by imaging the FoV with 2$\times$1 second exposures which provided detectability down to $r' \sim$12.

The sources with RMS scatter greater than 3 times the statistical error are considered variable and sources with at least 2 data points more than 4σ from the mean magnitude are also considered to be variable. An exception is made for several of the sources based on visual

inspection of their light curves or previous data suggesting variability, these are also include in Table 3.1. For example, two flickering sources in Table 3.1, CXB2 and CXB48, have an RMS scatter is 1.3 and 2.1 times the statistical error, respectively. CXB2 is an emission line source and possible XRB transient (see Jonker et al. 2014 and below) and CXB48 is coincident with a 2XMM source and is a probable main sequence star.

Table 3.1: Variable CXB Source List

ID	**<mag>**	**<err>**	**RMS**
CXB1	16.994	0.002	0.026
CXB2	20.148	0.051	0.067
CXB3	18.880	0.002	0.023
CXB4	11.276	0.010	0.021
CXB8	11.313	0.001	0.017
CXB10	19.670	0.011	0.201
CXB13	14.073	0.019	0.030
CXB14	14.489	0.003	0.019
CXB17	13.095	0.006	0.024
CXB19	17.603	0.007	0.015
CXB23	19.101	0.015	0.043
CXB24	20.566	0.040	0.126
CXB26	19.449	0.042	0.439
CXB30	13.745	0.011	0.053
CXB31	14.405	0.008	0.022
CXB33	12.864	0.015	0.038
CXB34	19.184	0.007	0.016
CXB35	14.016	0.005	0.016
CXB37	20.799	0.049	0.079
CXB38	18.061	0.010	0.019
CXB40	17.565	0.004	0.014
CXB41	13.066	0.002	0.058

Continued on Next Page...

Table 3.1 – Continued

ID	<mag>	<err>	RMS
CXB42	15.136	0.005	0.034
CXB43	17.481	0.035	0.062
CXB44	19.795	0.038	0.052
CXB45	11.689	0.005	0.011
CXB48	18.905	0.036	0.075
CXB49	14.636	0.001	0.012
CXB50	18.766	0.007	0.037
CXB51	18.251	0.021	0.032
CXB52	17.233	0.011	0.015
CXB53	19.505	0.029	0.040
CXB54	15.266	0.043	0.551
CXB55	12.460	0.087	0.069
CXB56	19.253	0.116	0.410
CXB57	17.820	0.023	0.018
CXB58	12.670	0.003	0.123
CXB60	18.447	0.011	0.026
CXB61	15.309	0.003	0.052
CXB62	14.844	0.006	0.016
CXB63	13.256	0.002	0.008
CXB64	17.900	0.005	0.017
CXB65	17.818	0.002	0.005
CXB66	11.887	0.003	0.009
CXB67	14.203	0.002	0.015

Continued on Next Page...

Table 3.1 – Continued

ID	<mag>	<err>	RMS
CXB68	15.751	0.002	0.044
CXB69	16.366	0.003	0.037
CXB71	18.794	0.025	0.188
CXB74	15.180	0.001	0.010
CXB75	15.406	0.002	0.069
CXB77	16.837	0.006	0.045
CXB78	17.106	0.005	0.016
CXB79	19.305	0.012	0.104
CXB82	16.379	0.008	0.024
CXB84	14.275	0.003	0.006
CXB86	19.010	0.015	0.027
CXB87	13.725	0.003	0.026
CXB88	18.059	0.037	0.020
CXB97	12.526	0.004	0.176
CXB98	15.924	0.008	0.016
CXB99	16.884	0.011	0.066
CXB100	16.215	0.014	0.028
CXB101	14.771	0.005	0.017
CXB102	19.176	0.047	0.097
CXB104	19.773	0.037	0.108
CXB105	14.394	0.006	0.018
CXB106	18.073	0.011	0.016
CXB107	17.026	0.074	0.018

Continued on Next Page...

Table 3.1 – Continued

ID	<mag>	<err>	RMS
CXB108	13.741	0.021	0.036
CXB111	14.562	0.007	0.027
CXB113	17.760	0.005	0.040
CXB114	12.244	0.001	0.005
CXB117	18.066	0.001	0.007
CXB118	20.101	0.010	0.068
CXB119	17.110	0.018	0.048
CXB120	13.784	0.002	0.027
CXB123	14.825	0.004	0.189
CXB124	14.789	0.006	0.018
CXB125	19.310	0.005	0.018
CXB126	18.723	0.021	0.017
CXB131	15.231	0.006	0.016
CXB134	17.269	0.003	0.009
CXB135	19.322	0.003	0.037
CXB136	16.198	0.011	0.006
CXB137	18.924	0.012	0.043
CXB139	12.841	0.004	0.010
CXB141	18.956	0.010	0.065
CXB143	15.723	0.009	0.011
CXB145	17.882	0.015	0.025
CXB149	16.186	0.005	0.011
CXB150	17.975	0.007	0.011

Continued on Next Page...

Table 3.1 – Continued

ID	<mag>	<err>	RMS
CXB151	11.5463	0.003	0.007
CXB153	15.853	0.010	0.060
CXB155	17.096	0.001	0.015
CXB158	20.476	0.077	0.362
CXB162	13.618	0.011	0.022
CXB166	18.828	0.015	0.029
CXB168	18.130	0.007	0.039
CXB170	18.890	0.006	0.035
CXB171	16.141	0.017	0.023
CXB172	19.626	0.006	0.044
CXB174	17.439	0.004	0.018
CXB175	19.456	0.073	0.208
CXB176	14.929	0.006	0.025
CXB177	16.765	0.004	0.007
CXB178	18.333	0.009	0.021
CXB179	17.517	0.012	0.032
CXB180	19.694	0.033	0.120
CXB182	17.831	0.007	0.023
CXB183	11.798	0.005	0.023
CXB184	18.128	0.017	0.119
CXB185	15.363	0.021	0.427
CXB186	15.022	0.007	0.016
CXB188	18.036	0.005	0.013

Continued on Next Page...

Table 3.1 – Continued

ID	<mag>	<err>	RMS
CXB190	15.298	0.007	0.026
CXB192	19.064	0.022	0.028
CXB193	17.352	0.004	0.018
CXB194	15.203	0.006	0.027
CXB199	15.289	0.002	0.024
CXB200	11.826	0.004	0.067
CXB205	18.661	0.069	0.204
CXB208	11.516	0.002	0.007
CXB215	17.800	0.001	0.027
CXB216	17.740	0.082	0.260
CXB217	17.621	0.002	0.018
CXB218	16.653	0.009	0.024
CXB220	19.731	0.012	0.026
CXB222	18.079	0.007	0.073
CXB223	18.540	0.011	0.036
CXB224	13.206	0.009	0.025
CXB227	16.927	0.006	0.014
CXB228	15.002	0.012	0.024
CXB230	16.315	0.033	0.035
CXB231	16.521	0.010	0.015
CXB232	16.530	0.009	0.027
CXB234	18.173	0.008	0.021
CXB235	12.947	0.014	0.048

Continued on Next Page...

Table 3.1 – Continued

ID	<mag>	<err>	RMS
CXB236	17.873	0.030	0.096
CXB238	17.430	0.018	0.048
CXB239	15.157	0.006	0.029
CXB241	18.912	0.117	0.079
CXB242	16.884	0.008	0.015
CXB243	15.398	0.015	0.026
CXB244	16.336	0.007	0.018
CXB247	12.321	0.004	0.014
CXB248	17.156	0.002	0.015
CXB249	16.089	0.004	0.022
CXB251	18.251	0.012	0.026
CXB253	18.073	0.018	0.021
CXB254	18.679	0.017	0.023
CXB255	15.433	0.008	0.036
CXB256	12.914	0.004	0.012
CXB257	18.111	0.005	0.028
CXB258	16.451	0.011	0.032
CXB262	18.178	0.021	0.059
CXB263	15.559	0.005	0.068
CXB268	16.673	0.003	0.010
CXB271	19.431	0.005	0.026
CXB272	18.339	0.011	0.015
CXB277	14.547	0.003	0.006

Continued on Next Page...

Table 3.1 – Continued

ID	<mag>	<err>	RMS
CXB278	15.976	0.014	0.017
CXB282	16.868	0.003	0.012
CXB284	13.874	0.009	0.144
CXB289	18.574	0.049	0.125
CXB290	13.218	0.006	0.010
CXB291	16.671	0.004	0.017
CXB292	16.970	0.006	0.006
CXB293	14.980	0.008	0.054
CXB294	17.752	0.028	0.019
CXB295	17.538	0.017	0.018
CXB302	13.256	0.005	0.013
CXB304	18.429	0.022	0.040
CXB307	18.074	0.000	0.005
CXB308	13.323	0.005	0.012
CXB309	19.691	0.000	0.056
CXB311	19.765	5.886	0.025
CXB312	18.359	0.001	0.045
CXB314	19.230	9.631	0.024
CXB315	15.984	0.004	0.010
CXB316	14.846	0.008	0.024
CXB317	20.378	3.005	0.022
CXB322	17.373	0.000	0.021
CXB324	17.131	0.000	0.019

Continued on Next Page...

Table 3.1 – Continued

ID	<mag>	<err>	RMS
CXB326	18.791	0.000	0.035
CXB327	20.806	0.001	0.124
CXB331	14.841	0.007	0.017
CXB332	16.123	0.000	0.008
CXB334	14.994	0.005	0.020
CXB335	16.754	0.012	0.043
CXB336	16.213	0.004	0.098
CXB337	18.101	0.031	0.072
CXB339	18.904	2.990	0.256
CXB341	17.910	6.202	0.017
CXB342	14.217	0.005	0.014
CXB343	17.192	0.006	0.023
CXB346	18.574	0.009	0.046
CXB347	16.567	0.011	0.016
CXB348	17.906	0.009	0.018
CXB349	17.906	0.012	0.023
CXB350	17.281	0.029	0.067
CXB352	16.787	0.002	0.033
CXB355	16.527	0.007	0.066
CXB357	18.507	0.018	0.046
CXB358	16.796	0.005	0.027
CXB359	17.604	0.012	0.169
CXB360	17.255	0.028	0.026

Continued on Next Page...

Table 3.1 – Continued

ID	<mag>	<err>	RMS
CXB361	17.629	0.018	0.211
CXB362	19.022	0.027	0.040
CXB364	15.777	0.011	0.010
CXB367	20.003	0.069	0.155
CXB370	18.090	0.007	0.026
CXB371	17.252	0.005	0.012
CXB372	15.996	0.015	0.010
CXB373	16.653	0.012	0.022
CXB376	16.070	0.003	0.005
CXB377	15.427	0.008	0.033
CXB378	16.871	0.003	0.032
CXB379	15.321	0.002	0.014
CXB383	17.575	0.003	0.014
CXB384	16.289	0.007	0.017
CXB385	19.549	0.012	0.016
CXB386	21.695	0.079	0.158
CXB389	19.869	0.031	0.034
CXB393	20.087	0.010	0.047
CXB395	15.785	0.015	0.041
CXB397	13.652	0.006	0.021
CXB399	14.280	0.019	0.047
CXB400	19.893	0.001	0.187
CXB405	14.625	0.003	0.028

Continued on Next Page...

Table 3.1 – Continued

ID	**<mag>**	**<err>**	**RMS**
CXB406	19.429	0.001	0.032
CXB407	19.041	0.001	0.029
CXB409	17.599	0.008	0.030
CXB410	15.976	0.003	0.021
CXB414	18.177	0.023	0.721
CXB419	16.561	0.010	0.034
CXB420	18.025	0.034	0.126
CXB423	18.929	0.001	0.008

Note: The first column refers to the CXB ID number from Jonker et al. (2014), column 2 is the average magnitude of the light curve, column 3 is the average statistical error on the magnitudes, and column 4 is the RMS scatter of the magnitudes in each light curve.

3.6 Individual Sources

In this section, I address individual variable sources contained in Table 3.1 and the possible nature of their inherent variability.

3.6.1 CXB2

CXB2 was classified as a broad Hα emitter based on Gemini/GMOS spectra (Wu et al., 2015) and having a FWHM $\geq$ 800 km s^{-1}. The strong, broad Hα emission most likely originates from an accretion disk and it is worth noting that no donor lines were present in the spectra. In the 2ks exposure by Chandra, we find 147 X-ray counts in the 0.3–8.0 keV range making CXB2 a very X-ray bright source. The hardness ratio of -0.18 $\pm$ 0.02 (Jonker et al., 2014) makes CXB2 a soft X-ray source and is labelled as an X-ray transient. This object shows flickering in the light curve of $\sim$0.3 magnitudes. A period of P = 0.112(3) days was found during a period search although scatter is still present once folded on this period. The light curve and phase-folded light curve can be seen in Figure 3.5. The $\frac{F_{\rm x}}{F_{\rm opt}}$ = 8.0–23.0 which can point to an AGN or IP although flickering is not consistent with an AGN scenario.

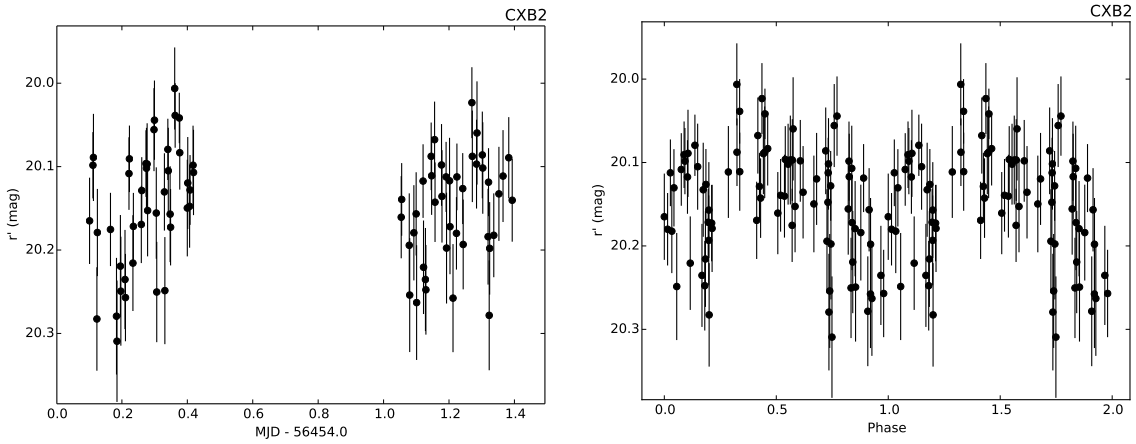

Figure 3.5: DECam light curve for CXB2 (left) and phase-folded light curve (right) folded on P = 0.112(3) days.

3.6.2 CXB10 = MACHO 401.48296.2600

CXB10 shows very active flickering in the light curve (Figure 3.6) by $\sim$0.8 magnitudes over the course of two consecutive nights. The VIMOS spectrum of CXB10 shows broad, double peaked Hα emission (FWHM $\approx$ 1600 km s^{-1}) and HeI λ6678 emission (private communication with M. A. P. Torres). CXB10 is coincident with the variable source MACHO 401.48296.2600, where MACHO is the *MAssive Compact Halo Object* search to look for microlensing events in the Galactic Bulge, the LMC and SMC (Alcock et al. 1996). Using the MACHO database, Cieslinski et al. (2004) have shown that this source is a DN candidate showing 3 outbursts over a range of 1676 days which reach a maximum of $\Delta V = 3.5$ magnitudes above the quiescent level of $V = 19.7$ (see Table 1 of Cieslinski et al. 2004). We also find that CXB10 has an $\frac{F_{\rm x}}{F_{\rm opt}} = 2.0$–$6.0$, placing in the regime of IP or CV and lending further support to the claim of a DN.

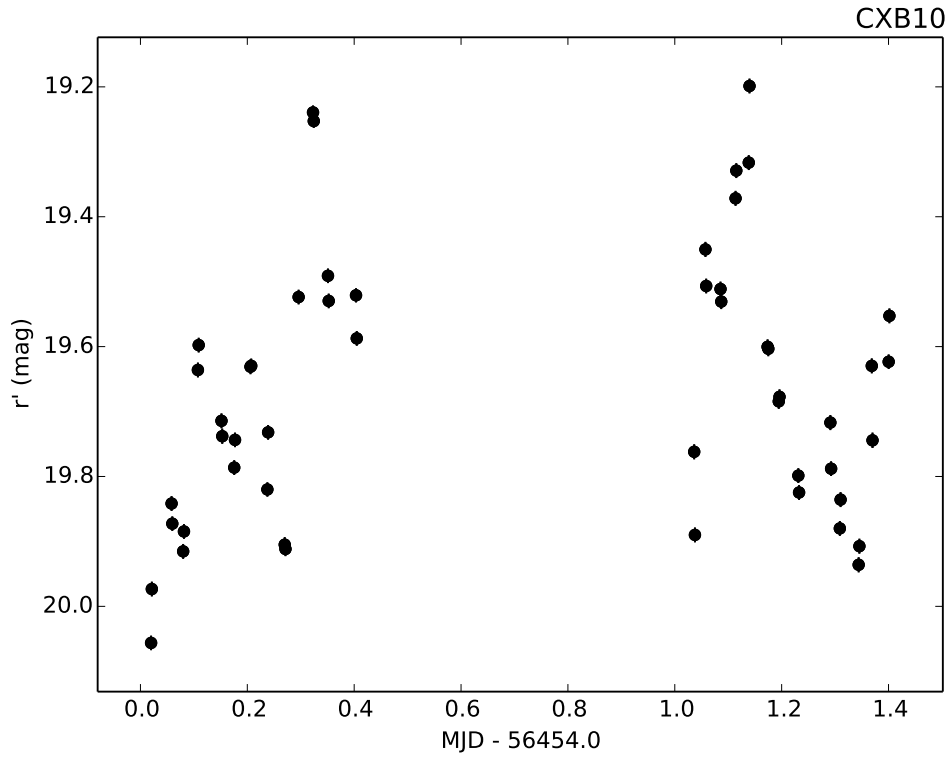

Figure 3.6: DECam light curve of CXB10.

3.6.3 CXB26

CXB26 is labeled as a flaring variable in Table 3.1 although the more appropriate designation would be an outburst. The DECam light curve in Figure 3.7 shows a $\sim$1 magnitude rise from the first night where the rise halts halfway through the second night. An increase in brightness over the span of approximately (at most) $\sim$1 day is not unheard of for DN outbursts where rise times can be as short as a few days (Warner, 2003). Figure 3.7 shows a reference image (left) and the variance image (right) of CXB26 highlighting the outburst. CXB26 is considered to be likely associated with the OGLE source *OGLE BUL_SC3 563176* which is identified as a CV. In their paper, Wu et al. (2015) showed that the spectra of CXB26 was devoid of any emission lines that would indicate an accretion disk but claim that it could be a hidden accreting binary. The $\frac{F_{\rm x}}{F_{\rm opt}} = 0.9$–$2.0$ which places CXB26 in either the qLMXB or CV category. Based on all the evidence, CXB26 is most likely a DN.

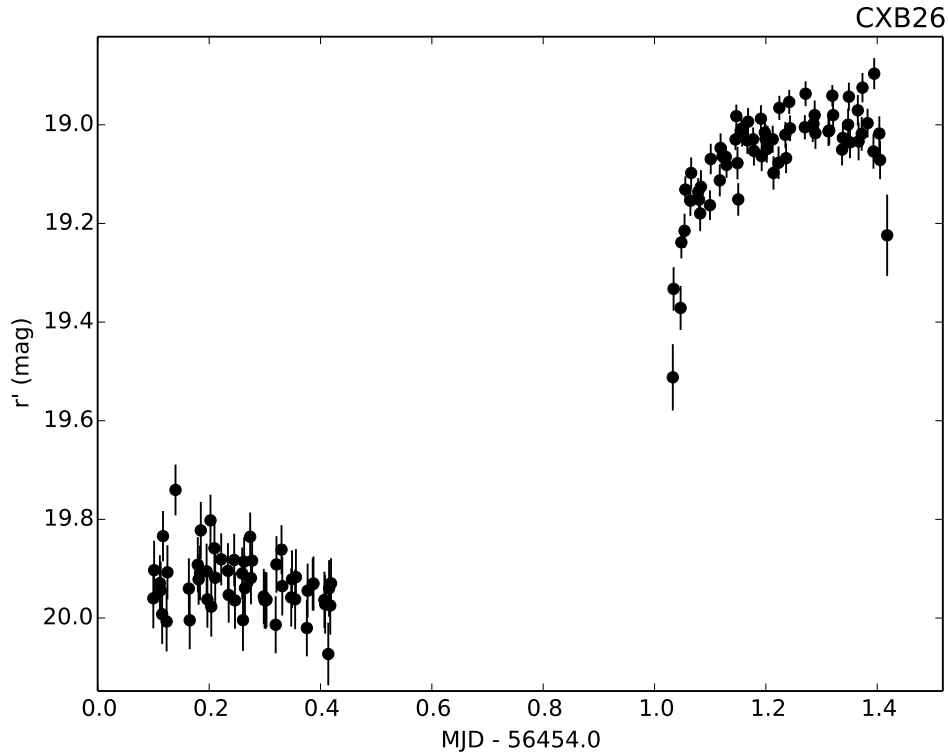

Figure 3.7: DECam light curve of CXB26.

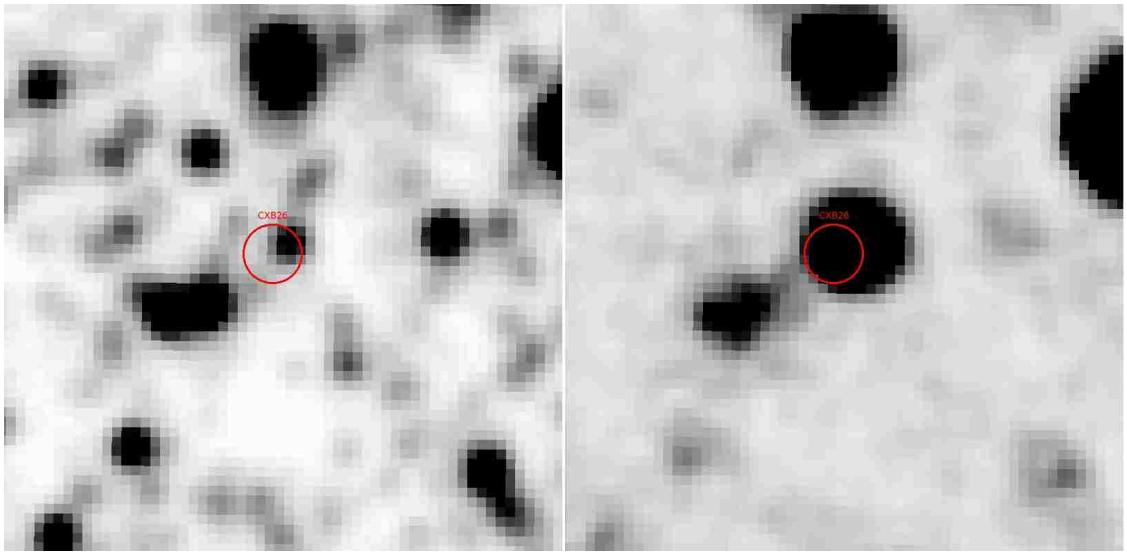

Figure 3.8: The reference image (left) and the variance image (right) of CXB26. North is up, East is left and the image sizes are 15.5" on a side.

3.6.4 CXB30

CXB30 is a periodic variable showing a sinusoidal modulation on a P = 0.523(3) day period. The left and right panels of Figure 3.9 show the light curve and phase-folded light curve of CXB30, respectively. The light curve shows an amplitude of $\Delta r' = 0.2$ magnitudes and appears to be stable over both nights. Conservative estimates for the $\frac{F_{\rm x}}{F_{\rm opt}}$ span the range 0.004–0.01. The period, light curve morphology and $\frac{F_{\rm x}}{F_{\rm opt}}$ all point to CXB30 as being a possible low inclination W UMa star.

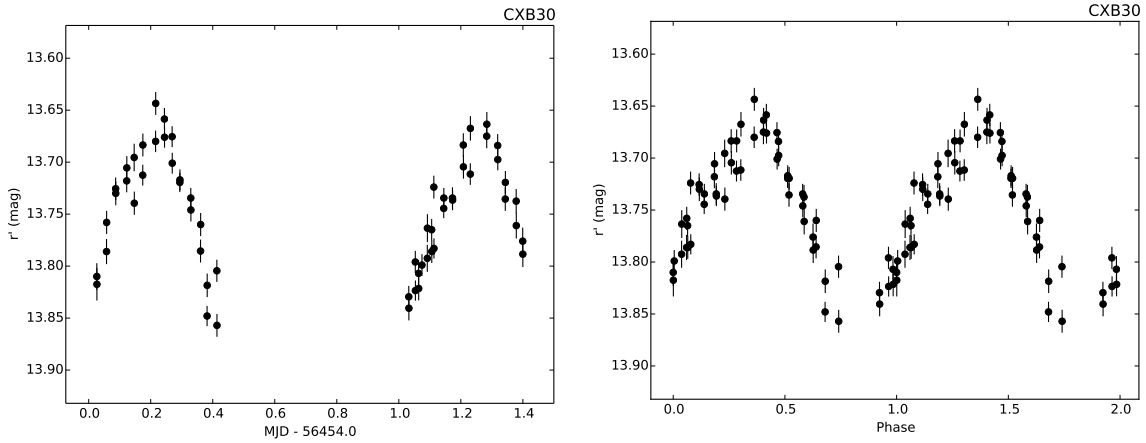

Figure 3.9: DECam light curve of CXB30 (left) and the phase-folded light curve (right) folded on P = 0.523(3) days.

3.6.5 CXB41

CXB41 appears as an LPV in the DECam data brightening by ∼0.17 magnitudes over two nights and is shown in Figure 3.10. In an attempt to constrain the period of this system, I fit a simple sine wave function to the data allowing all the parameters to vary. The best fit shows a minimum period of ≥ 5 days but we caution that this period assumes the maximum of the light curve is reached on the second night and follows the trend from the first night. I point out that this could be an ellipsoidal light curve where a simple sine wave would not be appropriate for the data but a combination of two sine waves. The $\frac{F_{\rm x}}{F_{\rm opt}} = 0.001$–$0.006$ making it an RS CVn candidate. In this scenario, a 5 day period is quite typical.

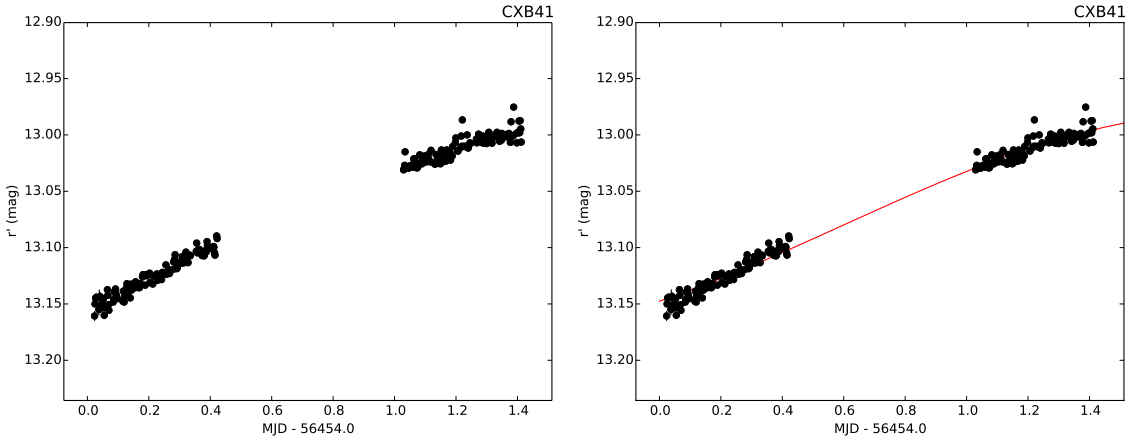

Figure 3.10: DECam light curve of CXB41 (left) and a simple sine wave fit to the data with a minimum period of 5.01(5) days.

3.6.6 CXB48

CXB48 is included as a flickering variable and is coincident with $2XMM\ J175534.1-291136$ (Lin et al. 2012). The light curve and finder chart is shown in the top and bottom panels of Figure 3.11. The red error circle in the finder chart is the CXO pointing and the white error circle is the XMM pointing. The other stars in or on the error circle were not variable. The light curve shows significant flickering of $\sim$0.3 magnitudes and no period was recovered. The $2XMMi-DR3$ catalogue (Lin et al. 2012) has this source marked as "star" which they define as "star, probably main-sequence star". I find a $\frac{F_{\rm x}}{F_{\rm opt}} = 0.2$–$0.7$ which rules out the idea of a main sequence star, but falls in the category of qLMXB or CV. Spectroscopy could immediately provide evidence of a qLMXB if emission lines are seen with a lack of HeII λ4686.

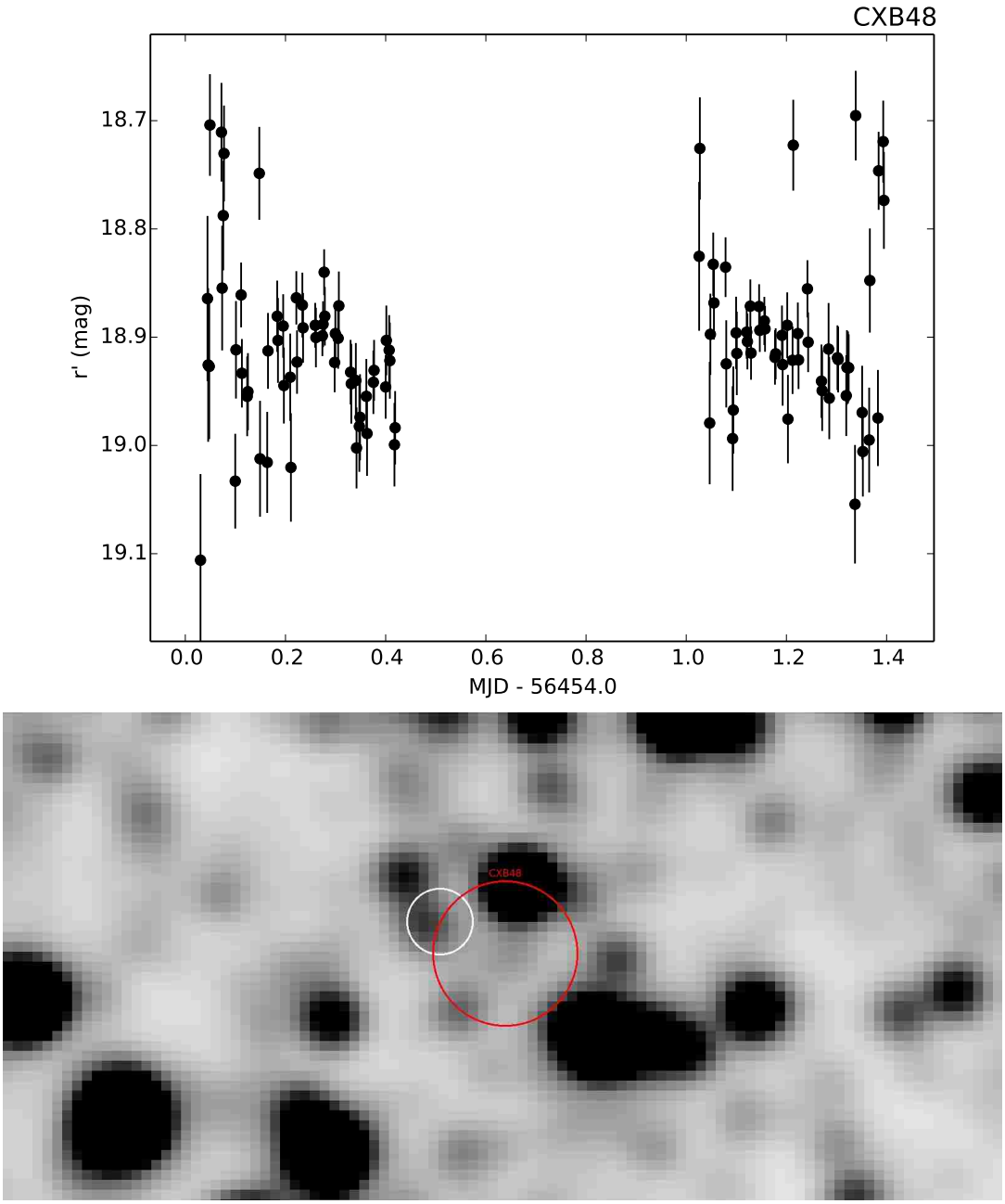

Figure 3.11: DECam light curve (top) and finder chart (bottom) for CXB48. The red circle is our Chandra pointing and the white circle is the XMM pointing. North is up, East is left and the image is 26"×14".

3.6.7 CXB58 = ASAS 175420-2938.3

CXB58 is an eclipsing variable where the ingress of one eclipse is caught on the first night with a minimum eclipse depth of $\Delta r' \approx 0.55$ below the average quiescent magnitude of $r'_q = 12.61$. CXB58 appears in the ASAS catalogue of photometry as ASAS 175420-2938.3 where it was observed from 2001 until 2009 in the V-band. The eclipsing nature is recovered in the ASAS data and a period search concluded in finding a 2.2479(4) day period. Figure 3.12 shows both the DECam light curve (left panel) and the phase-folded ASAS light curve (right panel). There is significant flickering outside of the eclipses in the ASAS data by $\Delta V \approx 0.2$ magnitudes which is not present in the DECam data. The $\frac{F_{\rm x}}{F_{\rm opt}} = 0.0006$–$0.001$ and the eclipsing, detached light curve are suggestive of a coronally active star in a binary.

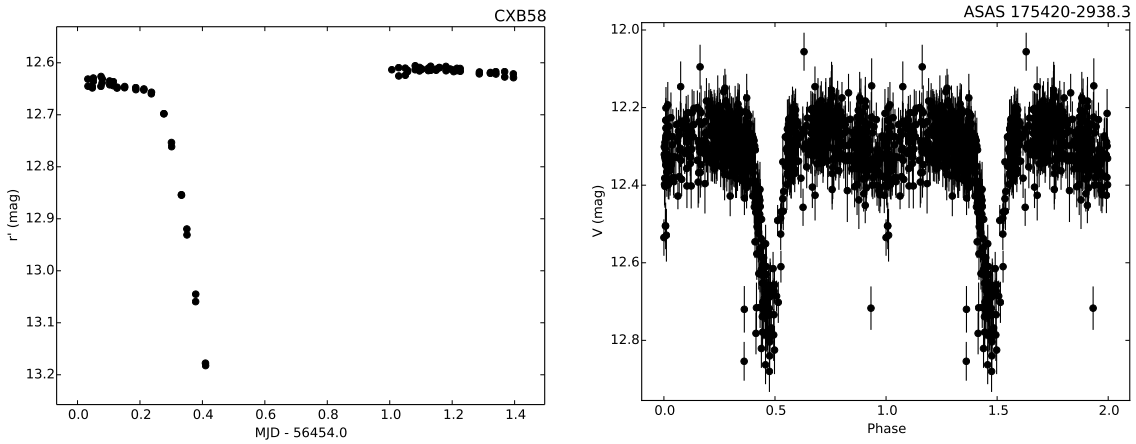

Figure 3.12: DECam light curve of CXB58 (left) and the ASAS phase-folded light curve (right) folded on P = 2.2479(4) days.

3.6.8 CXB64

CXB64 is classified as a flickering variable source with an RMS scatter of 0.017 and a $\Delta r' = 0.08$ magnitudes. Wu et al. (2015) have shown that CXB64 is a narrow Hα emitter with a FWHM ≤ 200 km s^{-1}. CXB64 is quite possibly a chromospherically active early-to-mid M-type star based on spectroscopic features including the presence of the TiO band. The $\frac{F_{\rm x}}{F_{\rm opt}} = 0.1$–$0.4$ would place CXB64 more in the regime of accreting binary where a qLMXB, IP or CV would be possible. A chromospherically active M dwarf can have a high $\frac{F_{\rm x}}{F_{\rm opt}}$ since most of the flux is in the IR and the optical flux is quite low. A complete time series spectroscopic followup with radial velocities would clear up this discrepancy.

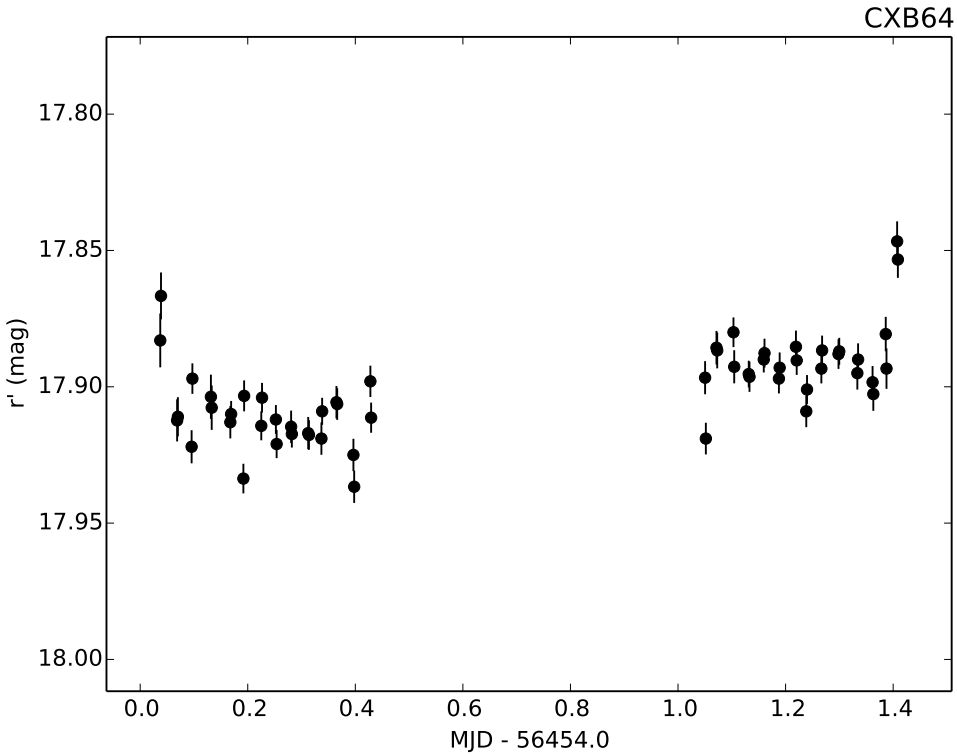

Figure 3.13: DECam light curve of CXB64.

3.6.9 CXB68

CXB68 is LPV where an apparent minima was caught at the end of the first night before increasing in brightness by ∼0.13 magnitudes. We fit a simple sine function to CXB68 (assuming that it is a sinusoidal light curve) to find an approximate period on the data and let the parameters vary. The fit yields a period of P = 2.702(7) days and can be seen in the right panel of Figure 3.14. The $\frac{F_{\rm x}}{F_{\rm opt}} = 0.01$–$0.05$ which is consistent with an RS CVn system.

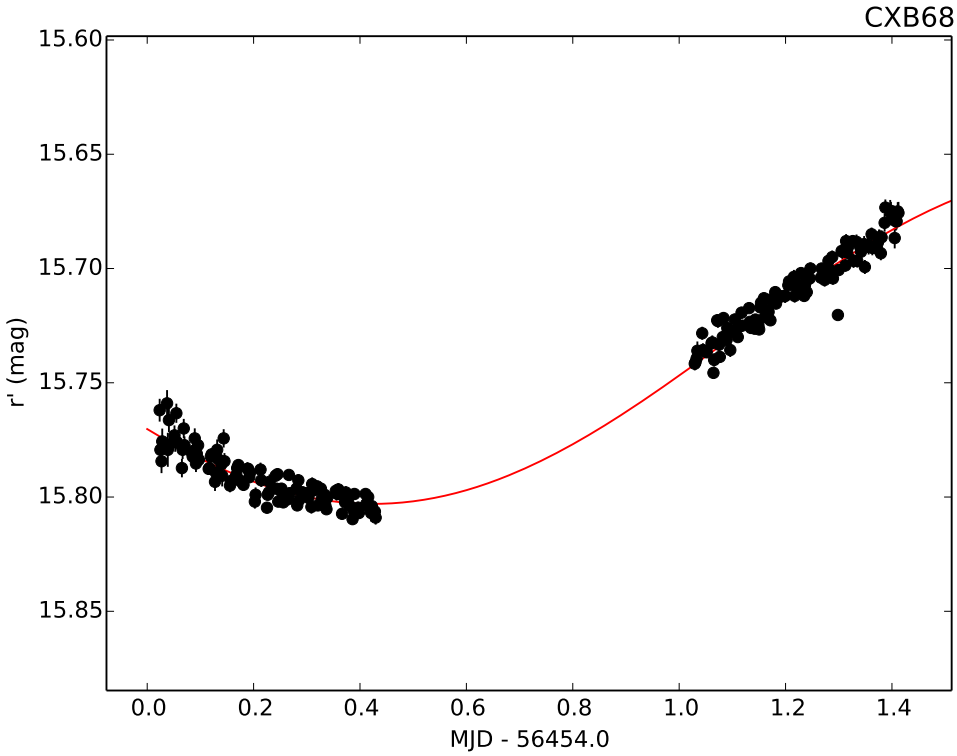

Figure 3.14: DECam light curve of CXB68 and best fit with a period of P = 2.702(7) days.

3.6.10 CXB77

CXB77 appears to be a LPV with decline of ∼0.15 magnitudes on the first night and then a brightening of ∼0.06 magnitudes the second night. A simple function would be tough to fit to the data since the light curve does not appear to be sinusoidal but possibly a combination of functions. The $\frac{F_{\rm x}}{F_{\rm opt}}$ = 0.03–0.1 and is consistent with a qLMXB with a BH primary or a CV but also an active star with a complex starspot morphology is possible.

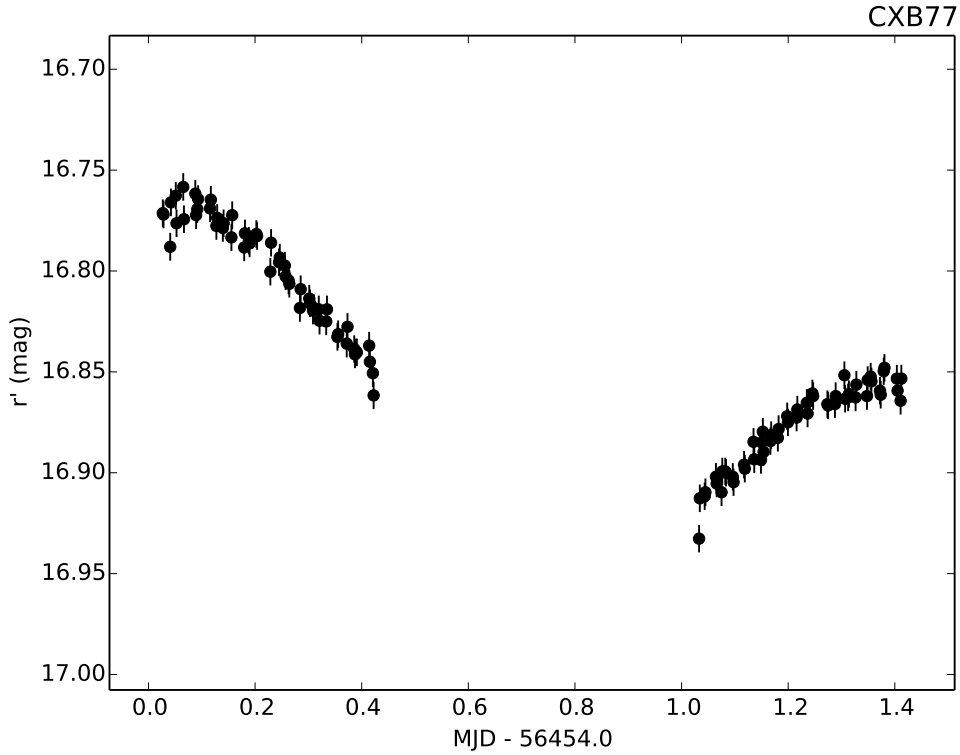

Figure 3.15: DECam light curve of CXB77.

3.6.11 CXB82

CXB82 shows flickering and a brightening on the second night by ∼0.05 magnitudes. Wu et al. (2015) have classified the optical counterpart as a G9 star. The residual spectra of CXB82, after optimally subtracting the best-fit stellar templates, show Hα emission features which fill in the stellar Hα absorption features (see Figure 8 of Wu et al. 2015). This "hidden" Hα emission could be explained by an accreting binary where the disk is just bright enough to completely fill in the Balmer absorption features from the companion. The $\frac{F_{\rm x}}{F_{\rm opt}} = 0.01$–$0.04$ and makes CXB82 a candidate qLMXB or a CV.

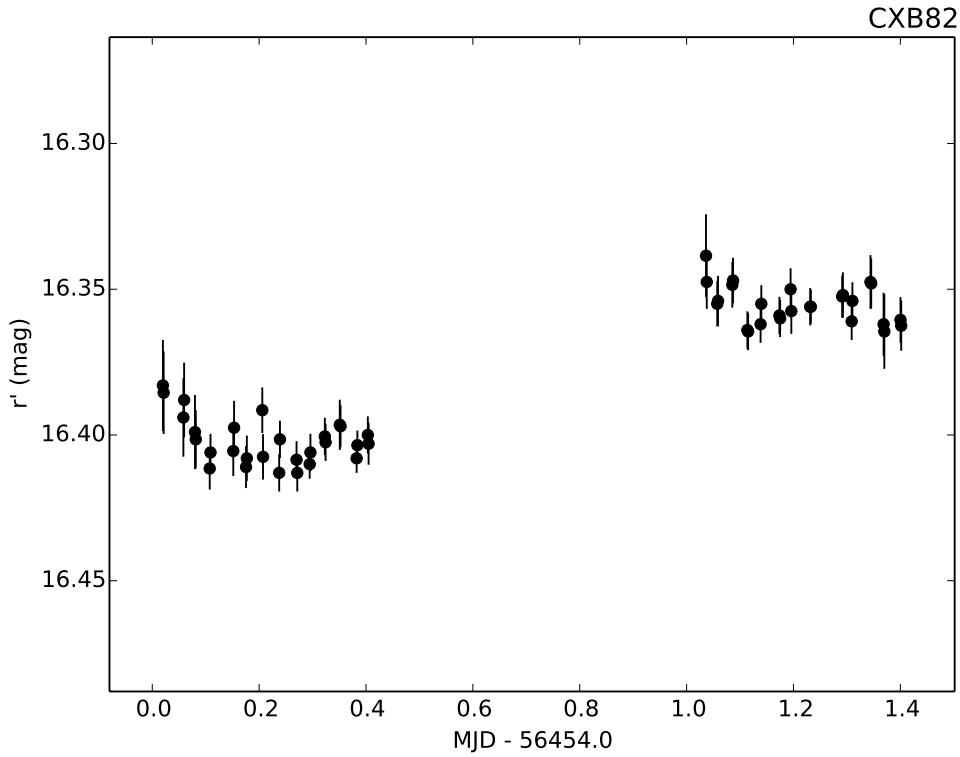

Figure 3.16: DECam light curve of CXB82.

3.6.12 CXB97 = V1723 Sgr

CXB97 is associated with $V1723$ Sgr, a known W Uma contact binary. The light curve and phase-folded light curve can be seen in the top panels of Figure 3.17. We recover a period of P = 0.29545(2) days. CXB97 also appears in the ASAS database as ASAS 175903-2729.3 with coverage from 2001 until 2009 where the phase-folded light curve is shown in the bottom panel of 3.17. The $\frac{F_{\rm x}}{F_{\rm opt}} = 0.0004$–$0.001$ where the unabsorbed flux ratio is more characteristic of W UMa systems meaning that CXB97 could be closer than Bulge distance.

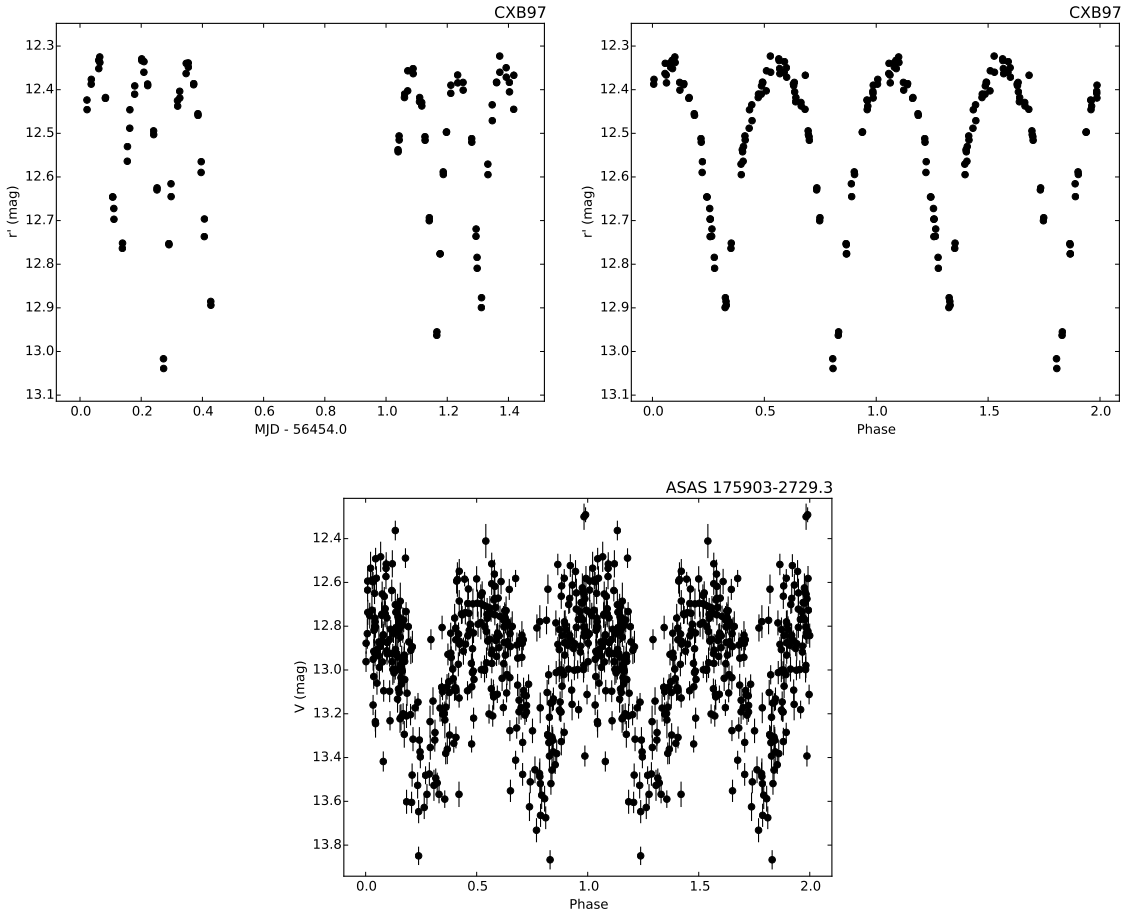

Figure 3.17: DECam light curve, DECam phase-folded light curve and ASAS phase-folded light curve of CXB97 on P = 0.29545(2) days.

3.6.13 CXB99

CXB99 is increasing in brightness by ∼0.2 magnitudes with an average of ∼0.07 magnitude flickering over both nights. Wu et al. (2015) spectrally classify CXB99 as a K2V type star showing weak, narrow Hα emission with FWHM $\leq$ 200 km s^{-1}. After subtraction with the K2V template spectrum, the Hα appears to be stronger indicating that it may partially be filling in the Hα absorption line lending support to an accreting binary. The $\frac{F_{\rm x}}{F_{\rm opt}}$ = 0.02–0.07 which suggests either a qLMXB or a CV, although an active star with chromospheric activity cannot be fully ruled out.

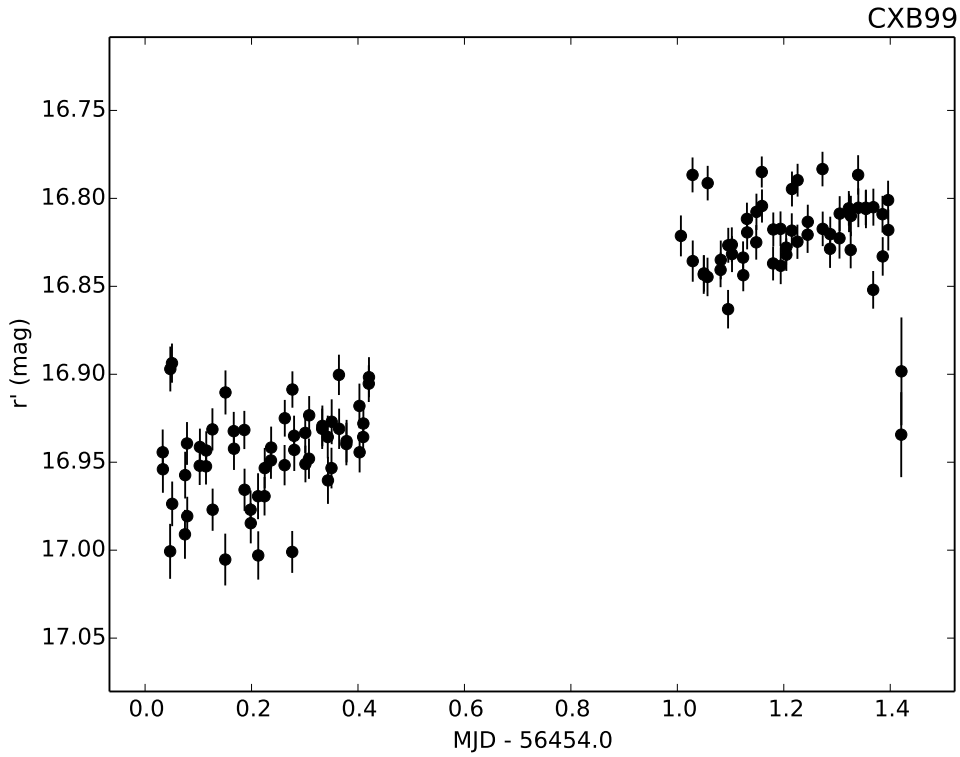

Figure 3.18: DECam light curve of CXB99.

3.6.14 CXB113

CXB113 is a periodic variable with a P = 1.1758(5) days (Figure 3.19). The light curve has an amplitude of ∼0.13 magnitudes in the r' band. The OGLE source *OGLE BUL_SC37 9614* is coincident with CXB113 and the phase-folded I-band light curve can be seen in the bottom panel of Figure 3.19. The spectra of CXB113 agree well with an M4V–M5V star (Wu et al., 2015) and is possibly chromospherically active or in a binary based on the weak, narrow Hα emission line. The $\frac{F_{\rm x}}{F_{\rm opt}}$ = 0.05–0.2 and based on the light curve and spectroscopy, CXB113 is most likely an active star. According to the relation $M_2 = 0.11 \times P_{\rm orb}$(hours) (Frank et al., 2002), a $P_{\rm orb}$ = 1.1758 days = 28.22 hrs is too long for a Roche lobe filling M4V–M5V star.

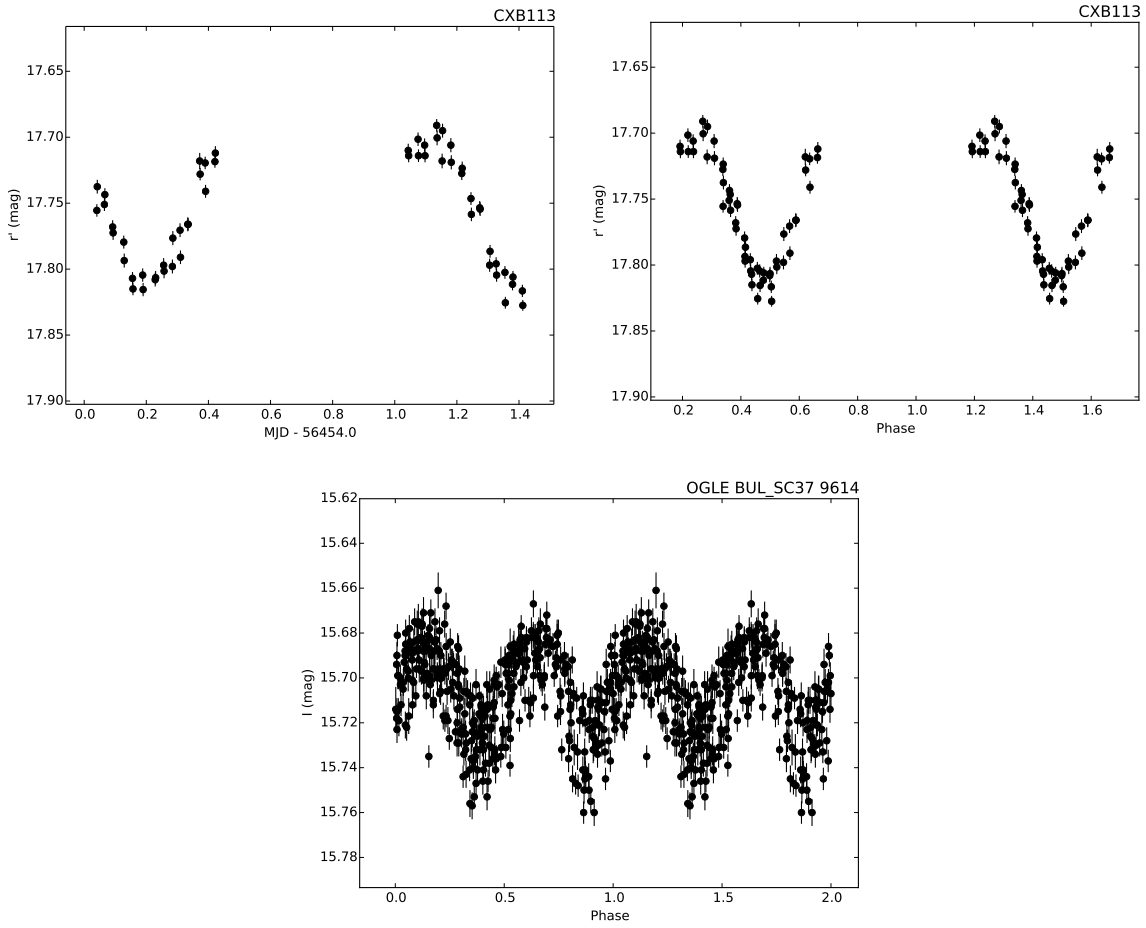

Figure 3.19: DECam light curve and phase-folded light curve of CXB113 (top panels). OGLE phase-folded light curve of CXB113 = *OGLE BUL_SC37 9614* (bottom panel). P = 1.1758(5) days for both folds.

3.6.15 CXB120

CXB120 appears as an ellipsoidal variable with a period of P = 0.427(1) days. Both light curves can be see in Figure 3.20 with a $\Delta r' = 0.1$ magnitudes and unequal minima. The $\frac{F_{\rm x}}{F_{\rm opt}} = 0.001$–$0.003$ which would indicate a flare star or, more likely, a W UMa.

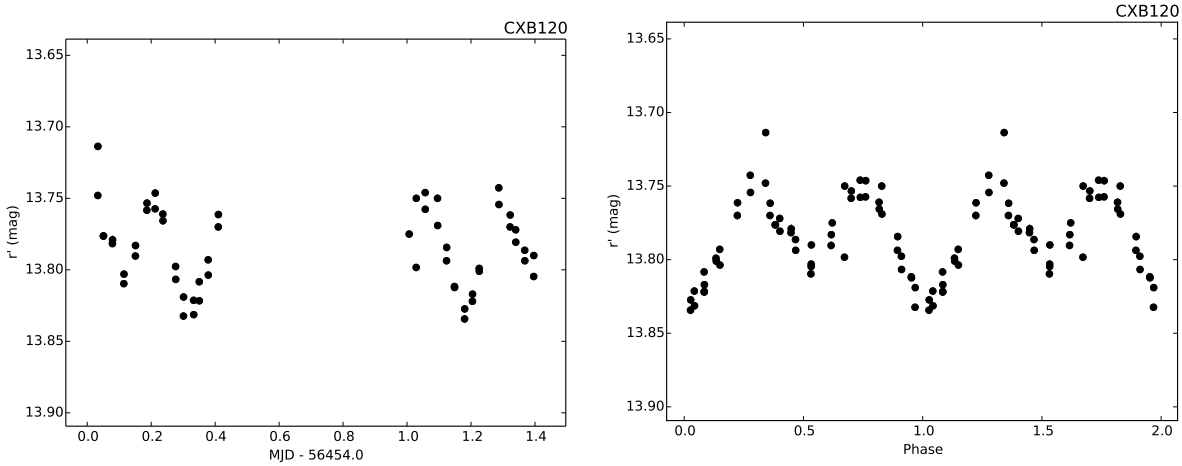

Figure 3.20: DECam light curve and phase-folded light curve of CXB120 folded on P = 0.427(1) days.

3.6.16 CXB123

CXB123 is an eclipsing binary with a period of P = 0.776(2) days. The eclipse depths are 0.65 magnitudes for the secondary and 0.85 for the primary eclipse with eclipse durations lasting about 2.6 and 2.8 hours. The light curve and phase folded light curve can be seen in Figure 3.21. The light curve resembles a detached, eclipsing binary with grazing eclipses from the companion. The $\frac{F_{\rm x}}{F_{\rm opt}}$ = 0.003–0.009 is indicative of coronal activity from one, or both, stars in a binary.

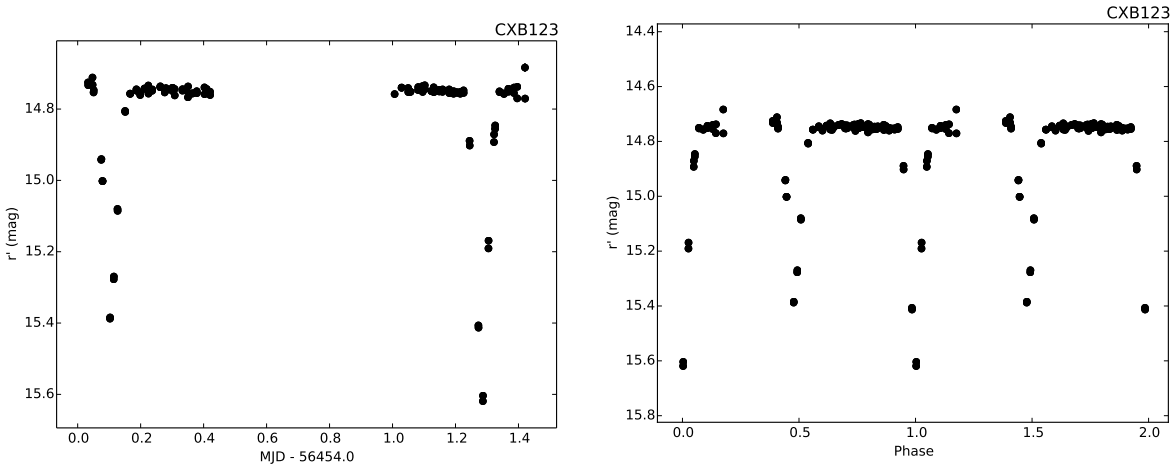

Figure 3.21: DECam light curve and phase-folded light curve of CXB123 folded on P = 0.776(2) days.

Using the morphology of the eclipses we can gain some insight in to the components of the system by making a few assumptions. Let us assume that the $\frac{F_{\rm x}}{F_{\rm opt}}$ constrains the system to coronal activity from late-type dwarf stars only (FGKM spectral type). Looking at the depth ratio of the eclipses, we can use the relation $\frac{\Delta m_{\rm p}}{\Delta m_{\rm s}} = \left(\frac{\rm T_s}{\rm T_p}\right)^4$ (Kallrath & Milone, 2009), where $\Delta m_{\rm p}$ and $\Delta m_{\rm s}$ are the eclipse depths for the primary and secondary eclipse. We assume that the hotter star, which I refer to as $\rm T_s$, passes behind the companion during primary eclipse so all the light during primary is attributed to the cooler star. We also

assume circular orbits and no mass transfer between the components. I find that $\frac{\mathrm{T_s}}{\mathrm{T_p}} = 1.07$. Using homology relations for the lower main sequence, mainly, L $\propto$ M^3 and R $\propto$ M$^{\frac{1}{2}}$ and the Stefan-Boltzmann law:

$$\frac{L_\mathrm{p}}{L_\mathrm{s}} = \left(\frac{R_\mathrm{p}}{R_\mathrm{s}}\right)^2 \left(\frac{\mathrm{T_p}}{\mathrm{T_s}}\right)^4 \tag{3.8}$$

we end up with the relation: $\frac{M_\mathrm{p}}{M_\mathrm{s}} = \left(\frac{\mathrm{T_p}}{\mathrm{T_s}}\right)^2 = 0.873$. I then used Eric Mamajek's online atlas of stellar parameters[8] for approximate effective temperatures and masses that would match the approximate ratios found above. This sample consisted of 45 different dwarf stars ranging from spectral type F0V–M9V. Then I calculated the orbital separation for the best fit combination of stellar components masses, and using the times of ingress and egress for the primary eclipse in the light curve, I calculated radii of the components.

Based on all the assumptions, ratios, and effective temperatures and masses[8], I find that CXB123 can described as a detached binary system having a 1.07 $\mathrm{M_\odot}$ G1V and a 0.94 $\mathrm{M_\odot}$ G8V star with an orbital separation of 4.5 $\mathrm{R_\odot}$ and the found period of P = 0.776 days. The calculated radii of the two components are 1.06 and 0.95 $\mathrm{R_\odot}$ for the G1V and G8V stars, respectively, which are consistent with the parameters in Binney & Merrifield (1998). The caveat is that there may be several different scenarios for combinations of stellar components especially if the system is not circular. The situation described above is the best fit based on the observed parameters from the light curve morphology.

[8]http://www.pas.rochester.edu/∼emamajek/EEM_dwarf_UBVIJHK_colors_T$_{eff}$.txt

3.6.17 CXB137

CXB137 shows aperiodic flickering of up to 0.14 magnitudes on timescales of ∼13.7 minutes. This source appears in Wu et al. (2015) and is noted as having Hα in absorption without a clear spectral classification. The $\frac{F_{\rm x}}{F_{\rm opt}} = 0.1$–$0.4$ making it a candidate qLMXB or CV.

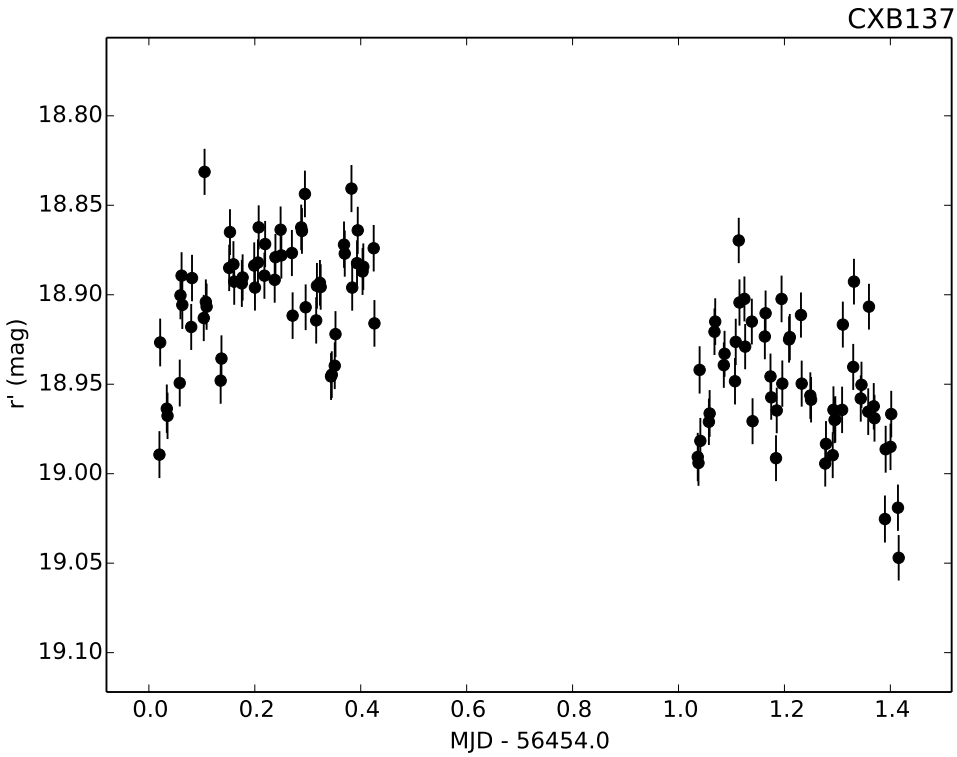

Figure 3.22: DECam light curve of CXB137.

3.6.18 CXB149

CXB149 is a flickering source and has been spectrally classified as a G6 type star (Wu et al., 2015) with residual Hα emission present after optimal template subtraction. CXB149 is coincident with the OGLE source *OGLE BUL_SC3 117676* and was observed from 1997 until 2000 in the I-band. The DECam light curve and OGLE light curve are shown in Figure 3.23. The light curves are uninteresting only showing slight flickering of ∼0.04–0.05 magnitudes on timescales of ∼10–15 minutes in both data sets. The $\frac{F_{\rm x}}{F_{\rm opt}} = 0.008$–$0.03$ and is probably attributed to coronal or chromospheric activity from the late-type G6 star, but a qLMXB or CV cannot be fully ruled out.

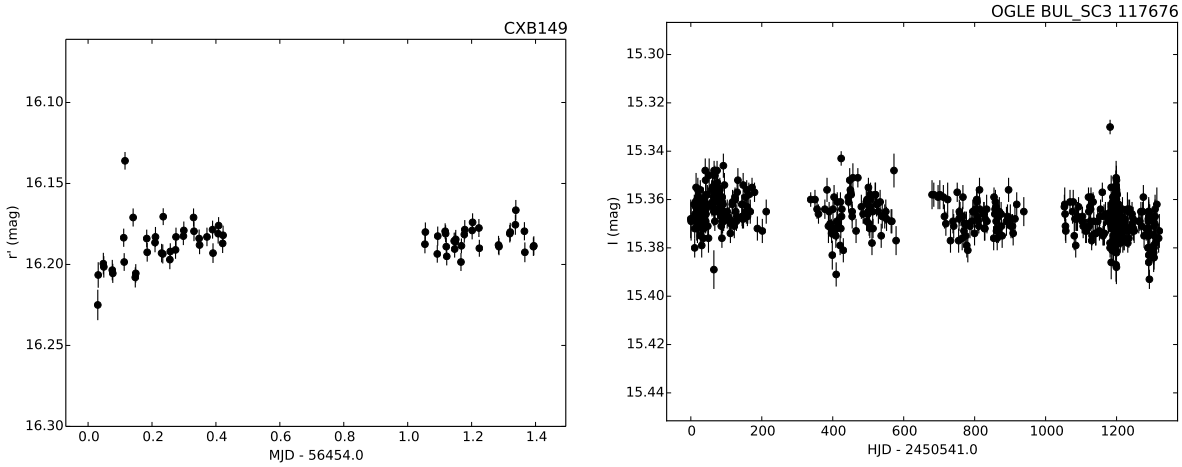

Figure 3.23: DECam light curve (left) and the OGLE light curve (right) of CXB149.

3.6.19 CXB155

CXB155 is a flaring system with two flares caught ∼1.3 days apart reaching a height of 0.07 and 0.06 magnitudes above quiescence. The duration of each flare, Δt, is 1.8 and 1.6 hours, respectively, and typical of active stars. The $\frac{F_{\rm x}}{F_{\rm opt}}$ = 0.02–0.1 and is well within the regime for flaring stars.

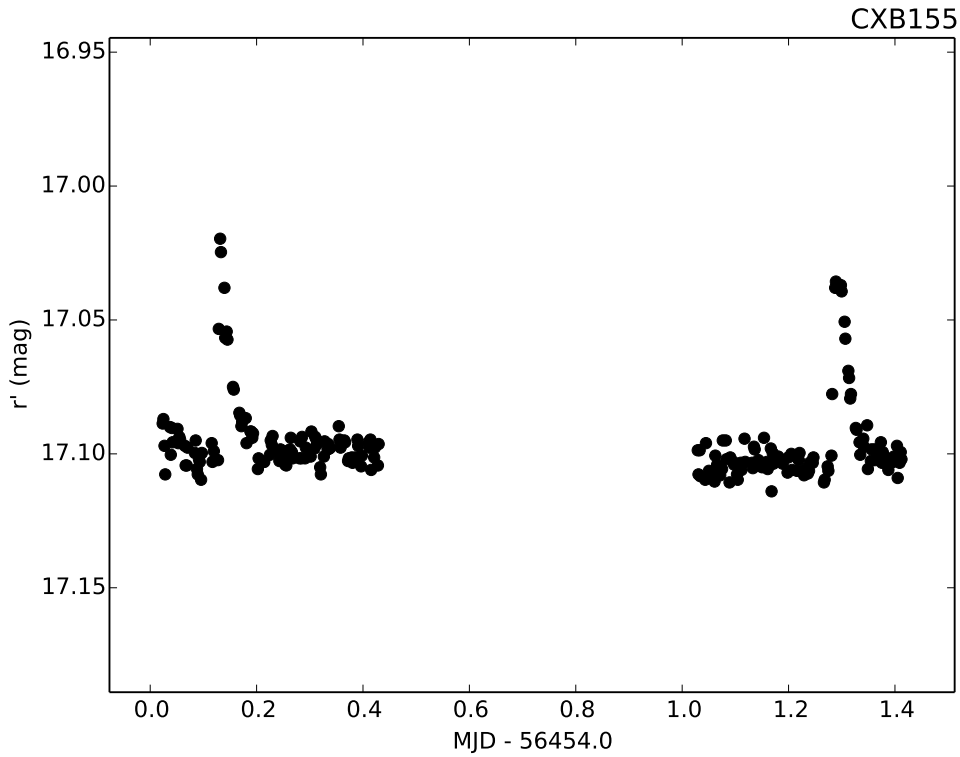

Figure 3.24: DECam light curve of CXB155.

3.6.20 CXB174

CXB174 is classified as a flickering source and spectrally classified as an F4III-type single star in Wu et al. (2015). The light curve (Figure 3.25) shows $\Delta r' = 0.05$ magnitudes with a $\sim$0.1 magnitude flare at the end of the second night preceded by up and down structure. No period was found and the $\frac{F_{\rm x}}{F_{\rm opt}} = 0.02$–$0.07$ which is consistent with flaring stars.

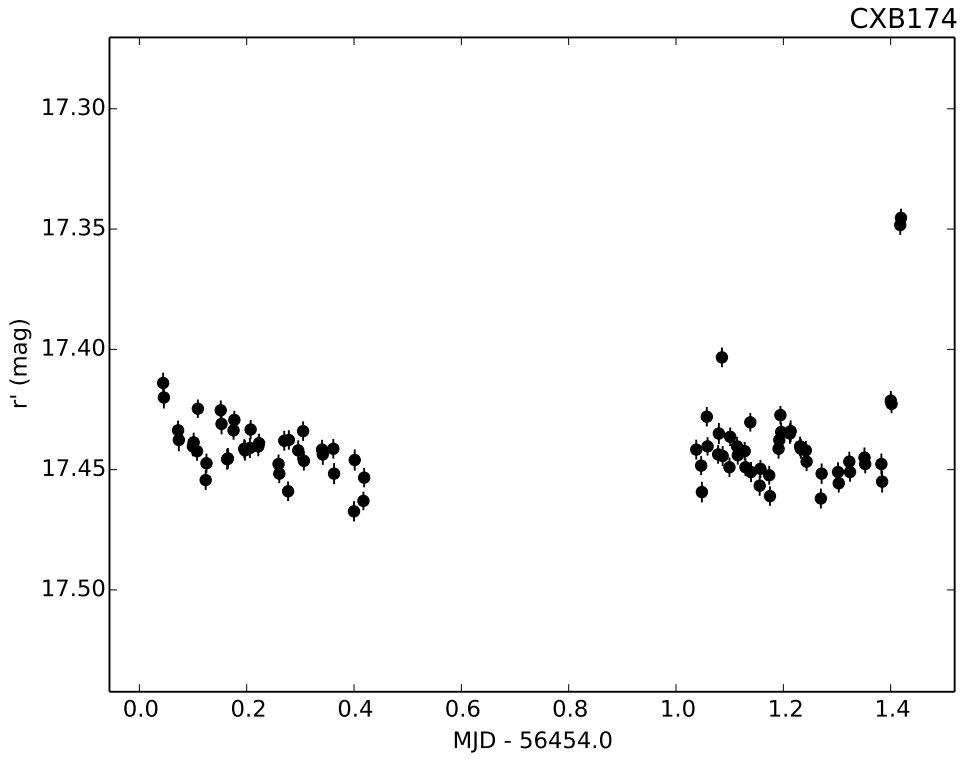

Figure 3.25: DECam light curve of CXB174.

3.6.21 CXB194

CXB194 is a periodic variable with a modulation of 0.385(7) days. Figure 3.26 shows both unequal minima and maxima and a $\Delta r' = 0.12$ magnitude in the phase-folded light curve. The light curve does not resemble a typical contact binary, but a low inclination W UMa is possible. The $\frac{F_{\rm x}}{F_{\rm opt}} = 0.003$–$0.01$ and supports the idea of a W UMa star.

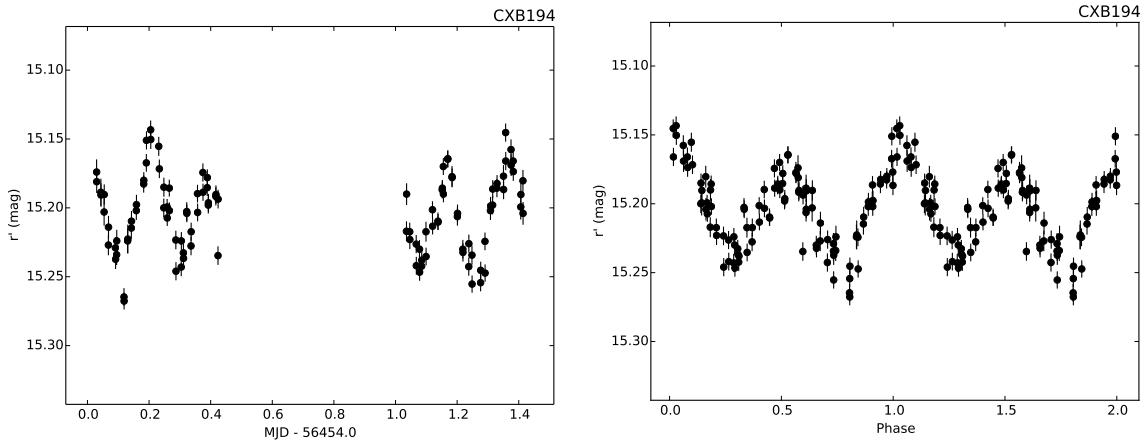

Figure 3.26: DECam light curve and phase-folded light curve of CXB194 folded on P = 0.385(7) days.

3.6.22 CXB199

CXB199 is classified as an ellipsoidal variable based on the DECam light curve in Figure 3.27 (left panel). With an amplitude of $\Delta r' = 0.08$ and a period of P = 0.712(1) days, the phase-folded light curve (right panel of Figure 3.27) shows more of a pulsating star light curve with both unequal minima and maxima. The $\frac{F_{\rm x}}{F_{\rm opt}} = 0.004$–$0.02$ and is reasonable for a W Uma but a qLMXB cannot be fully ruled out without spectroscopy.

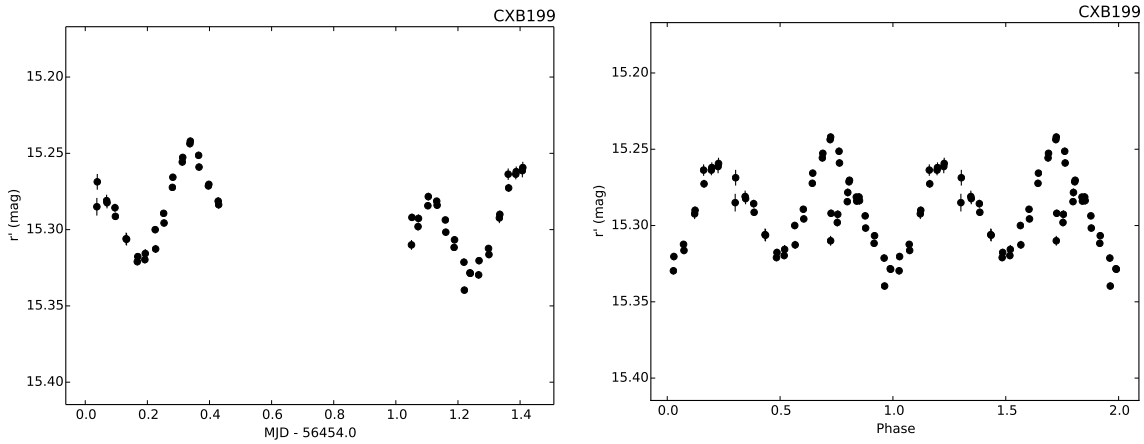

Figure 3.27: DECam light curve and phase-folded light curve of CXB199 folded on a P = 0.712(1) days.

3.6.23 CXB200 = TYC 7376-433-1

CXB200 is an eclipsing system and is aligned with the $TYCHO-2$ star $TYC\ 7376-433-1$ (Hynes et al., 2012). CXB200 is also found in the ASAS catalogue as *ASAS 173352-3050.5*. The DECam light curve in Figure 3.28 shows an eclipse the first night with a depth of ∼0.24 magnitudes and an asymmetric egress. A period search revealed a period of P = 0.363(4) days although the period is more likely twice this value, P = 0.726(4) days. The ASAS light curve is shown in the bottom right panel of Figure 3.28 and shows scatter of up to 0.45 magnitudes in the V-band. I fit a simple parabolic function to the eclipse data and find a time of mid-eclipse to be MJD = 56839.1839(5) (bottom panel of Figure 3.28). The period was recovered from the ASAS data set and it is somewhat different from our DECam data set in terms of overall trends. The primary and secondary eclipses are less pronounced in the V band and scatter is still present. As a further check to make sure the ASAS data was not confused with another star, I provide a finder chart in Figure 3.29 showing the GBS error circle (red), the TYCHO-2 stars in the FoV (cyan) and the ASAS pointings for the data set $ASAS\ 173352-3050.5$ (green). There does not seem to be any confusion with other bright stars in the field, the closest star is 8" away to the NW and has an i' magnitude of ∼16. The spectrum of CXB200 (Figure 3.30) has broad Balmer absorption lines, a very weak G band and no evidence of emission features. I classify CXB200 as an approximate F0–F4 type star. The $\frac{F_{\rm x}}{F_{\rm opt}} = 0.0001$–$0.0006$ and can be explained by normal coronal emission from a late-type star in a binary.

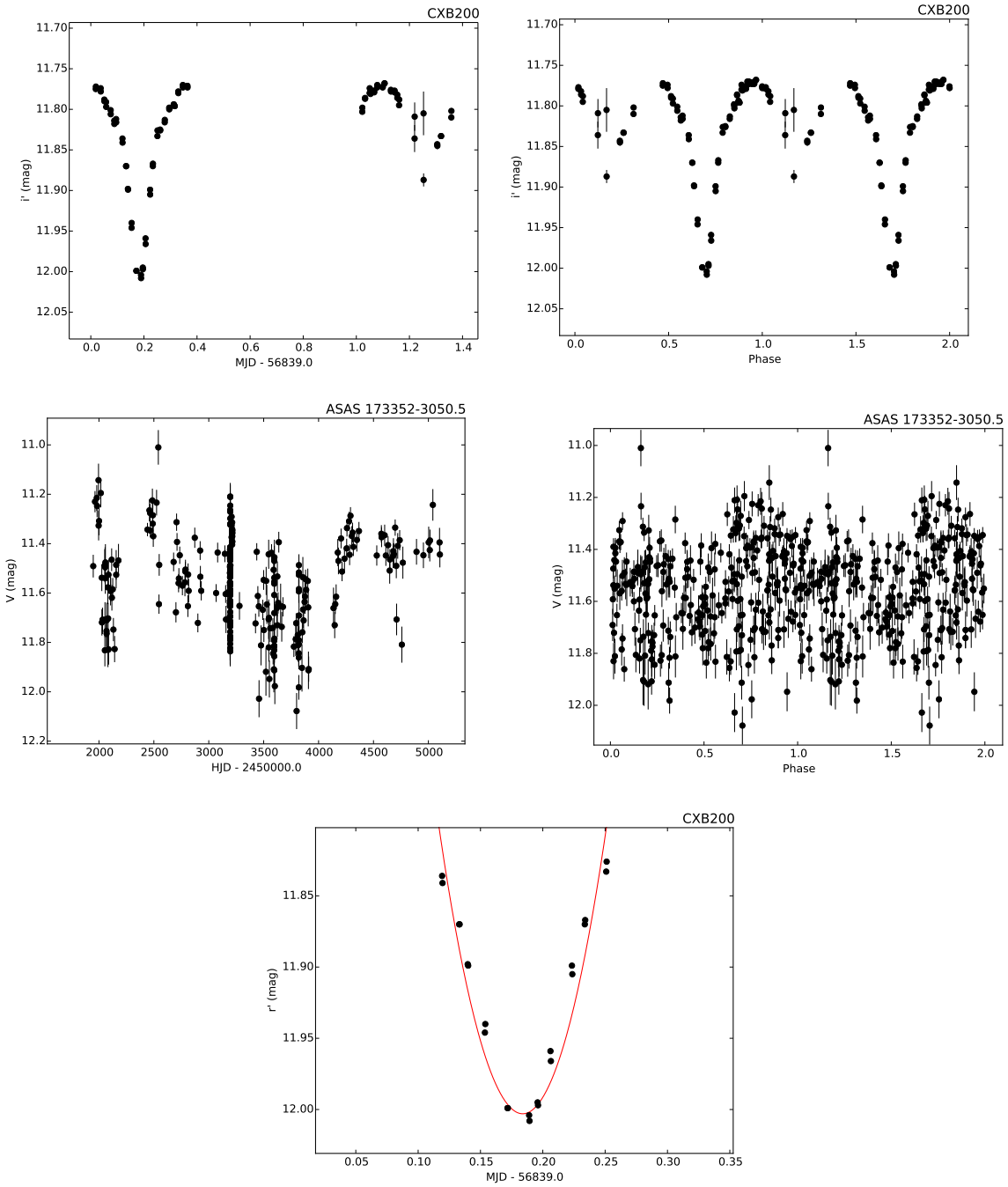

Figure 3.28: DECam light curve (top left) and phase-folded light curve (top right) of CXB200. ASAS light curve (middle left) and phase-folded light curve (middle right). Both phase-folded light curves are folded on P = 0.726(4) days. The bottom panel is a zoom-in and parabolic fit to the eclipse from night 1.

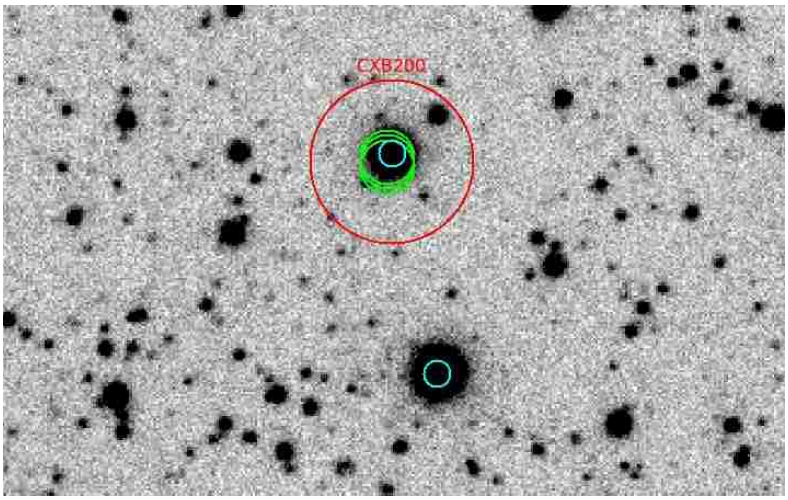

Figure 3.29: Finder chart for CXB200. The red circle is the Chandra GBS pointing and error circle, the cyan circles are TYCHO-2 stars and the green circles are ASAS pointings. North is up and East is left. The image is 85"×54".

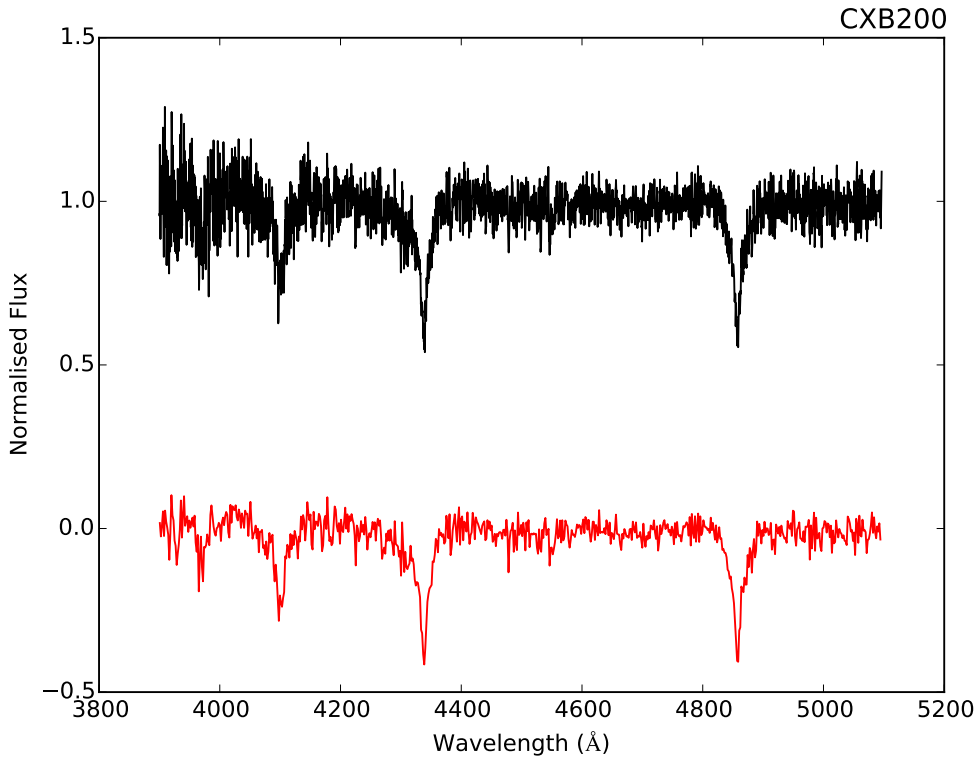

Figure 3.30: CXB200 optical spectroscopy obtained with the 2.0 m Liverpool telescope (see Section 2.5). The red spectrum is binned in bins of 5 and offset downward.

3.6.24 CXB284

CXB284 is an ellipsoidal variable with a period of P = 0.3717(6) days. Figure 3.31 shows unequal minima with $\Delta r' = 0.41$ and 0.39 magnitudes. The $\frac{F_{\rm x}}{F_{\rm opt}} = 0.001$–$0.004$ and further supports my claim that CXB284 is a definite W Uma contact binary.

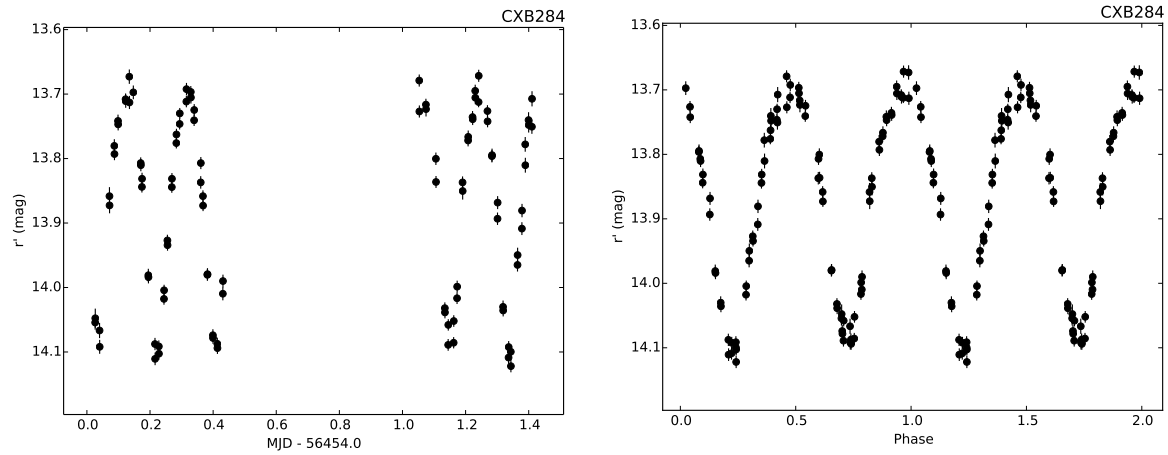

Figure 3.31: DECam light curve and phase-folded light curve of CXB284 folded on P = 0.3717(6) days.

3.6.25 CXB293

CXB293 is an eclipsing system showing a partial eclipse at the beginning of the second night with a depth of ∼0.22 magnitudes. The DECam light curve and zoom-in of the eclipse are shown in Figure 3.32. I fit a simple parabolic function to the eclipse data from the second night and find the time of mid-eclipse to be MJD = 56455.0408(5) based on the best fit. The $\frac{F_{\rm x}}{F_{\rm opt}}$ = 0.001–0.004 and supports the idea of a possible flaring star or coronally active star in a binary.

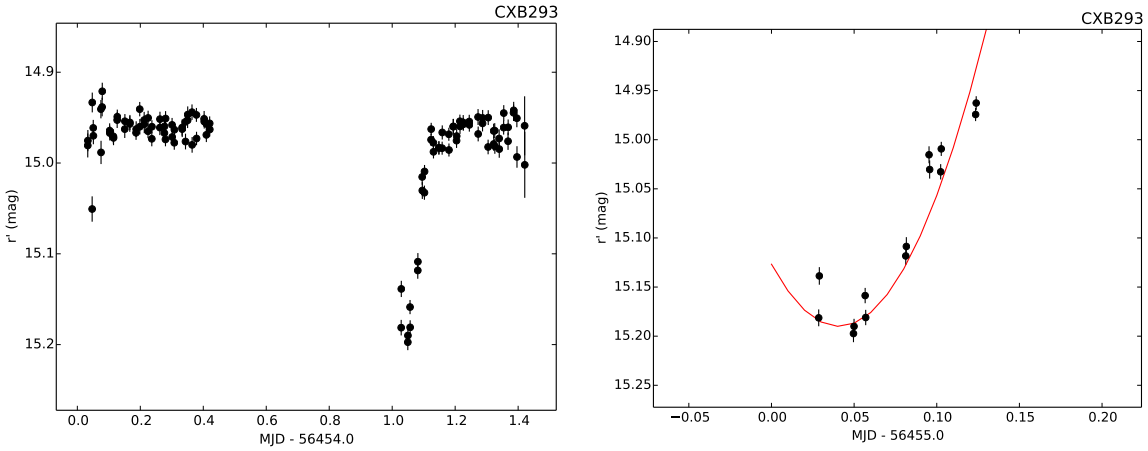

Figure 3.32: DECam light curve and zoom-in on a partial eclipse of CXB293. The red line is a parabolic fit to the eclipse on the second night.

3.6.26 CXB355

CXB355 is an ellipsoidal variable with a period of P = 0.538(2) days and unequal minima (see Figure 3.33). The $\frac{F_{\rm x}}{F_{\rm opt}} = 0.006$–$0.02$ confirming that it is a W UMa type contact binary.

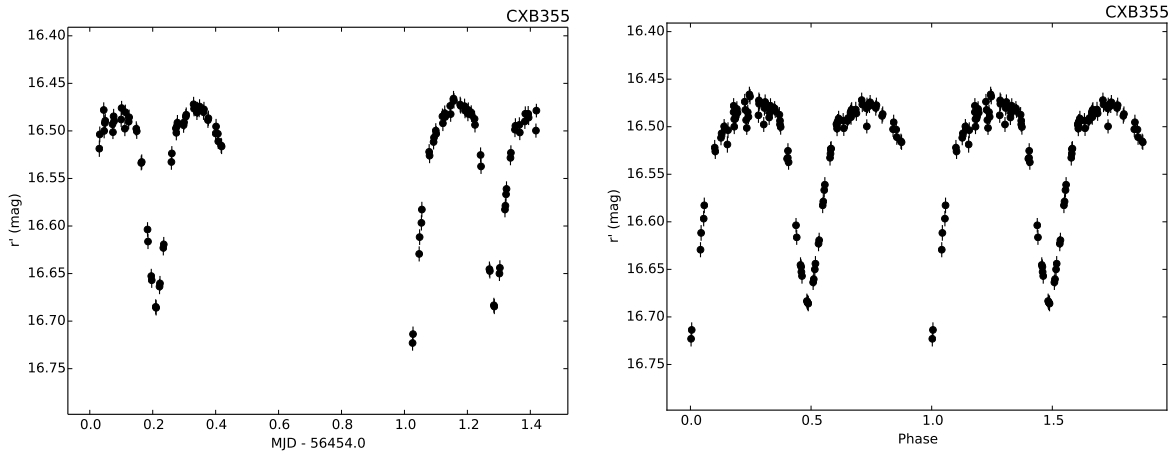

Figure 3.33: DECam light curve and phase-folded light curve of CXB355 folded on P = 0.538(2) days.

3.6.27 CXB405

CXB405 is classified as an eclipsing source based solely on the DECam light curve. The system has a period of P = 0.557(9) days and the phase-folded light curve shows more of a sinusoidal modulation. Both light curves are shown in Figure 3.34. The $\frac{F_{\rm x}}{F_{\rm opt}}$ = 0.001–0.006 and is suitable for an active star with starspots.

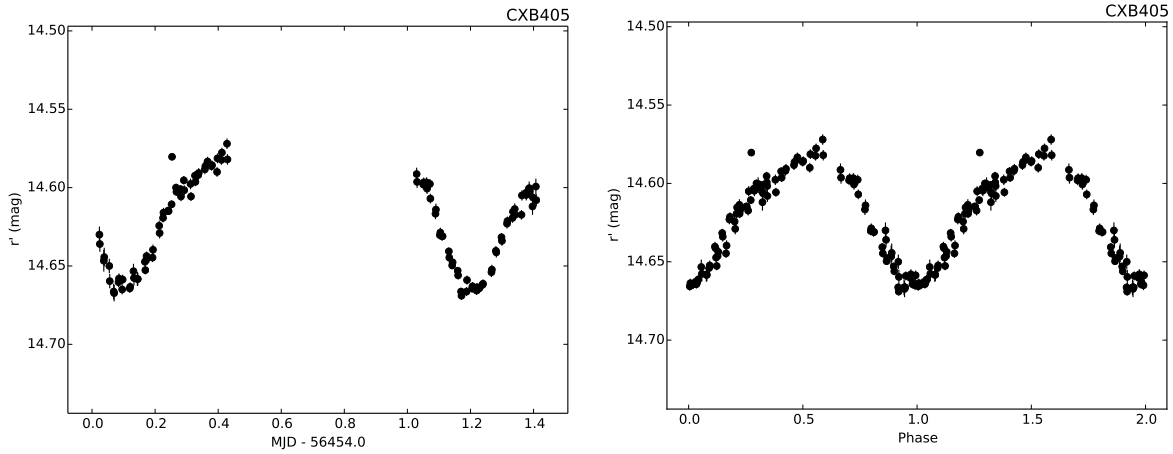

Figure 3.34: DECam light curve and phase-folded light curve of CXB405 folded on P = 0.557(9) days.

3.6.28 CXB409

CXB409 appears as a periodic variable with a modulation on P = 0.388(5) days. The light curve shows an amplitude of $\Delta r' = 0.12$ with some scatter in the beginning of the first night due to seeing. The light curve and phase-folded light curve are shown in Figure 3.35. A striking feature occurs in the second night after the system finishes brightening and abruptly declines in ∼32 minutes. It is possible that we are seeing structure in the optical light from an accretion disk. The spectrum of CXB409 shows late M-type features of an M2III–V star along with very narrow Balmer line emission (Figure 3.36) indicating an interacting binary of some kind. The $\frac{F_{\rm x}}{F_{\rm opt}}$ = 0.02–0.1, CXB409 is a probable active CV or qLMXB. Higher resolution spectra is needed to distinguish between the two.

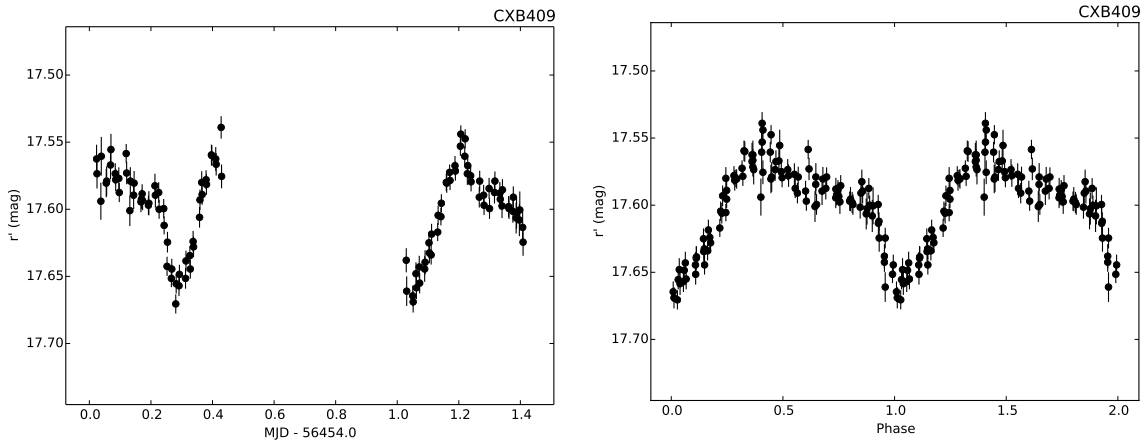

Figure 3.35: DECam light curve and phase-folded light curves of CXB409 folded on P = 0.388(5) days.

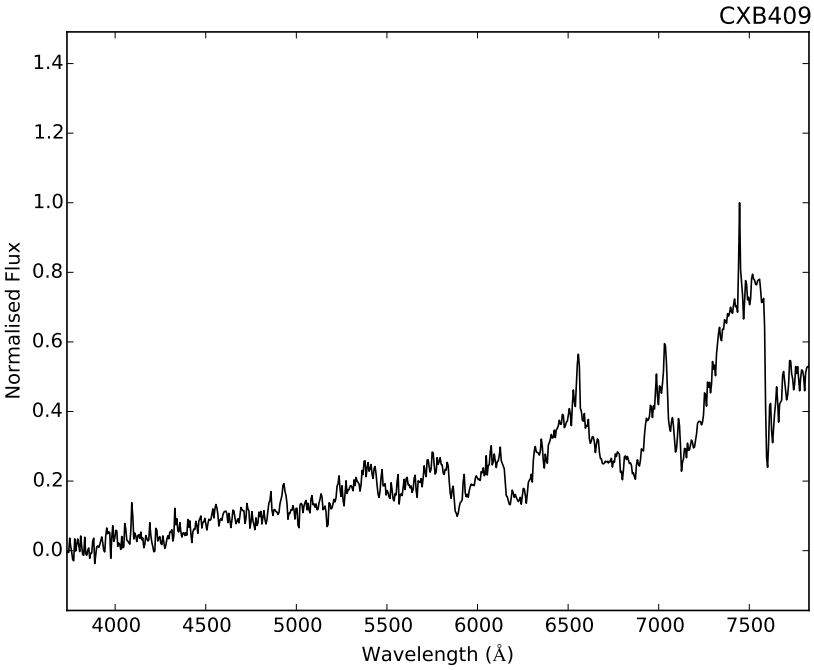

Figure 3.36: EFOSC2 spectrum of CXB409.

3.6.29 An Archival Search for Outbursts

Using the HCO plate archives, I did a search for previous optical outbursts of 4 quiescent LMXB candidates from Britt et al. (2014) and Torres et al. (2014) based on their spectroscopic signatures. All 4 sources (CX377, CX446, CX561 and CX1004) show emission line features in their spectra with CX1004 showing a double peaked Hα emission line profile with a FWHM = 2120 $\pm$ 20 km s^{-1} and a peak-to-peak velocity separation of Δv = 1170 $\pm$ 10 km s^{-1}. The search included the AM/AK plates from 1899-1953 and the RB patrol plates from 1928-1960. I found that in all of the plates I looked through, each target was below the plate limiting magnitude (B = 12-14 for AM/AK and B = 15 for RB) and found no outburst for each of the sources. This is not too surprising seeing as how many LMXBs are transient and alternate long periods of quiescence which can last decades with shorter outbursts lasting weeks to years (Bernardini et al., 2016). The chance of finding a week long outburst would be 7/365 or 1.9% per year. In order to insure that I catch an outburst for a hypothetical year, I would have to look through every 6th plate or $\sim$60 plates per year. The sampling of plates from HCO hinders our search since some years have hundreds of plates and some years have 3 plates for a specific target.

4. CX19: A New Deeply-Eclipsing Intermediate Polar

In this chapter, I discuss the GBS X-ray source CXOGBS J174954.5-294335 = CX19 for which we obtained optical photometry and spectroscopy along with X-ray spectroscopy. We find that CX19 is a deeply-eclipsing IP showing clear eclipses in both the optical and X-ray and, to our knowledge, is the first X-ray selected IP to do so. Figure 4.6 and its accompanying text and analysis were produced by C. Heinke. The VIMOS and FORS2 spectroscopy in Figure 5.1 and the spectroscopic measurements in Table 4.1 with text were supplied by M. A. P. Torres. Much of the text is reproduced from Johnson et al. 2016 (in prep) and contains all original research *except* that which is mentioned above.

4.1 Introduction

There are several main observational characteristics of IPs that define the subclass. In short, IPs are characterized by strong, hard X-ray emission, high-excitation spectra, and stable optical and X-ray pulsations in their light curves. From an optical standpoint, the system should show a stable photometric orbital period which can be determined from the spectroscopic radial velocity curve and/or the photometric modulation. Due to the radial accretion from the magnetic field lines on to the poles of the WD surface, X-ray pulsations or eclipses at the same, or very similar, photometric orbital period should be present. Depending on the geometry of each system and the inclination angle, X-ray eclipses can be full or partial (grazing). To complete the list for inclusion in to the IP subclass from Patterson (1994), there should be pulsations in the HeII emission lines which almost certainly arise from photoionization by the central X-ray source. We also expect to see circular polarization, "beat" or "sideband" frequencies in optical and X-ray light (usually on the low-frequency side of the main signal), and a very hard X-ray spectrum which is often accompanied by a

strong signature of low-energy absorption. These properties are shared among all confirmed IPs, but every property is not required for a system to be labeled as an IP.

4.2 Astrometry

The CXO pointing (OBSID 8742) provided a 95% confidence region with a 0.89 arcsec error circle calculated using equation 2.1. This left two variables within the error circle region, an eclipsing binary and a red giant, both of which have data in the OGLE database. We confirmed the eclipsing binary as the optical counterpart to our X-ray coordinates by using the Chandra Source Catalog (Evans et al., 2010) and a 15 ks CXO pointing (OBSID 9563) which provided a 95% confidence region centered on the coordinates of the eclipsing binary with a 0.39 arcsec error circle. The finder chart can be seen in Figure 4.1.

4.3 Orbital Period and Spin Period

CX19 was first classified as an eclipsing source in Britt et al. (2014). The data therein contained one eclipse point out of 20 data points over eight nights of observations so no orbital period could be found. Using DECam, we uncovered a full eclipse and partially cover two more eclipses over two nights. CX19 also appears in the OGLE-IV fields as an eclipsing source with a reported period of $P_{rep} = 0.3587$ days and an average out-of-eclipse I magnitude of 17.91 (Udalski et al., 2012).

We performed an initial period search on the DECam data using the software package PERIOD[1]. PERIOD is a time-series analysis package designed to search for periodicities in data sets using different analysis techniques. The Lomb-Scargle periodogram of the DECam data is shown in Figure 4.2 a). The DECam data shows a fundamental orbital frequency $f_{orb} = 2.7878(3)$ cycles/day. This frequency corresponds to the orbital period of $P_{orb} = 0.358(3)$

[1]http://www.starlink.rl.ac.uk/docs/sun167.htx/sun167.html

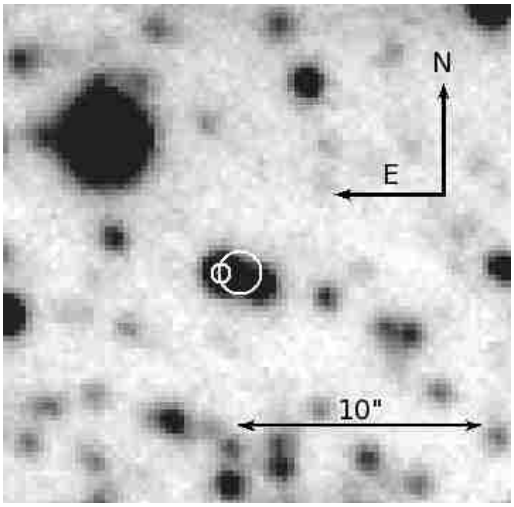

Figure 4.1: Finder chart for CX19. The white circles represent 95% confidence region error circles: the larger circle is the GBS X-ray position and the smaller is the Chandra Source Catalog X-ray position.

days and is consistent with the reported OGLE period (P_{rep} = 0.3587 days) from Udalski et al. (2012). A second fundamental frequency (f_{spin}) was found which turns out to be the WD spin frequency of 171.2915(9) cycles/day or P_{spin} = 0.005838(5) days = 504.4(5) secs.

The OGLE periodogram in Figure 4.2 b) was created after removing data points associated with apparent outbursts (I $\leq$ 17.50) in the OGLE data. We recovered a fundamental orbital frequency of f_{orb} = 2.78781(2) cycles/day and P_{orb} = 0.358704(2) days. This period is consistent with our DECam period to within 1σ and better constrained. We also recovered the WD spin frequency of f_{spin} = 170.3055(5) or P_{spin} = 0.0058718(3) days = 503.32(3) secs.

The light curves and phase-folded light curves for both DECam and OGLE data can be seen in in the left and right columns of Figure 4.3, respectively. The middle panels of Figure 4.3 show the light curves folded on P_{orb} and binned in phase bins of three consecutive data points. After binning the data, we find evidence of a secondary eclipse around phase 0.5 in both our data sets, and is most prominent in the OGLE light curve with an approximate depth of 0.23 mag. The bottom panels of Figure 4.3 show a clear modulation when folded on the P_{spin} with an amplitude of $\Delta r' = 0.3$ and $\Delta I = 0.4$ mag. We point out that upon

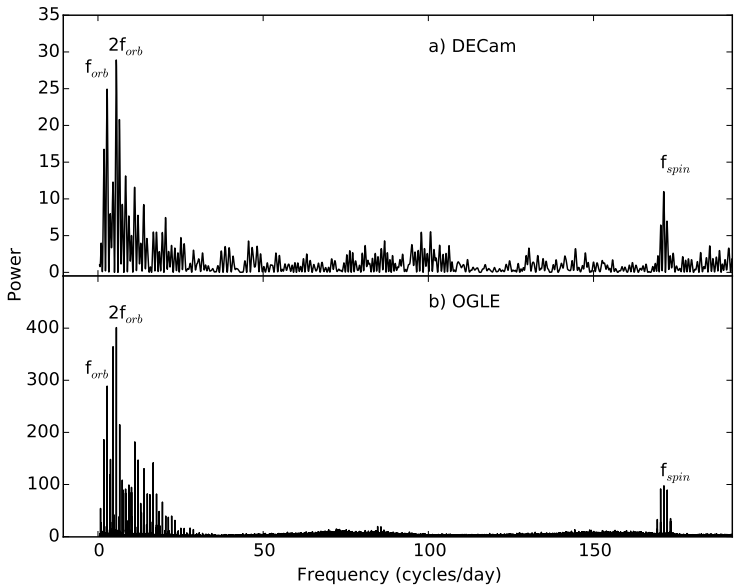

Figure 4.2: The initial Lomb-Scargle periodograms from the a) DECam data and the b) OGLE data. The orbital and spin frequencies are labelled along with the first orbital harmonic ($2f_{orb}$) as the most prominent peak.

inspecting the periodograms around both observed spin periods, we do not find any orbital sideband frequencies, but only frequencies that correspond to aliases. The sparse OGLE sampling leaves ambiguous 1 day aliases and the DECam resolves this ambiguity with the 2 day baseline.

Times of mid-eclipse were derived by fitting a parabolic function to the three eclipse profiles observed during the two nights of DECam observations. The parameters were allowed to vary while the χ^2 was calculated for every distinct set of parameters. In parameter space, we allowed the date, magnitude and width of the parabola to vary in order to find the best fit for the time of minimum of the eclipse using a parabolic function of the form:

$$y = a \times (\mathrm{T_{obs}} - h)^2 + k \tag{4.1}$$

where a is the width of the parabola, h and k are initial guesses for the HJD and magnitude

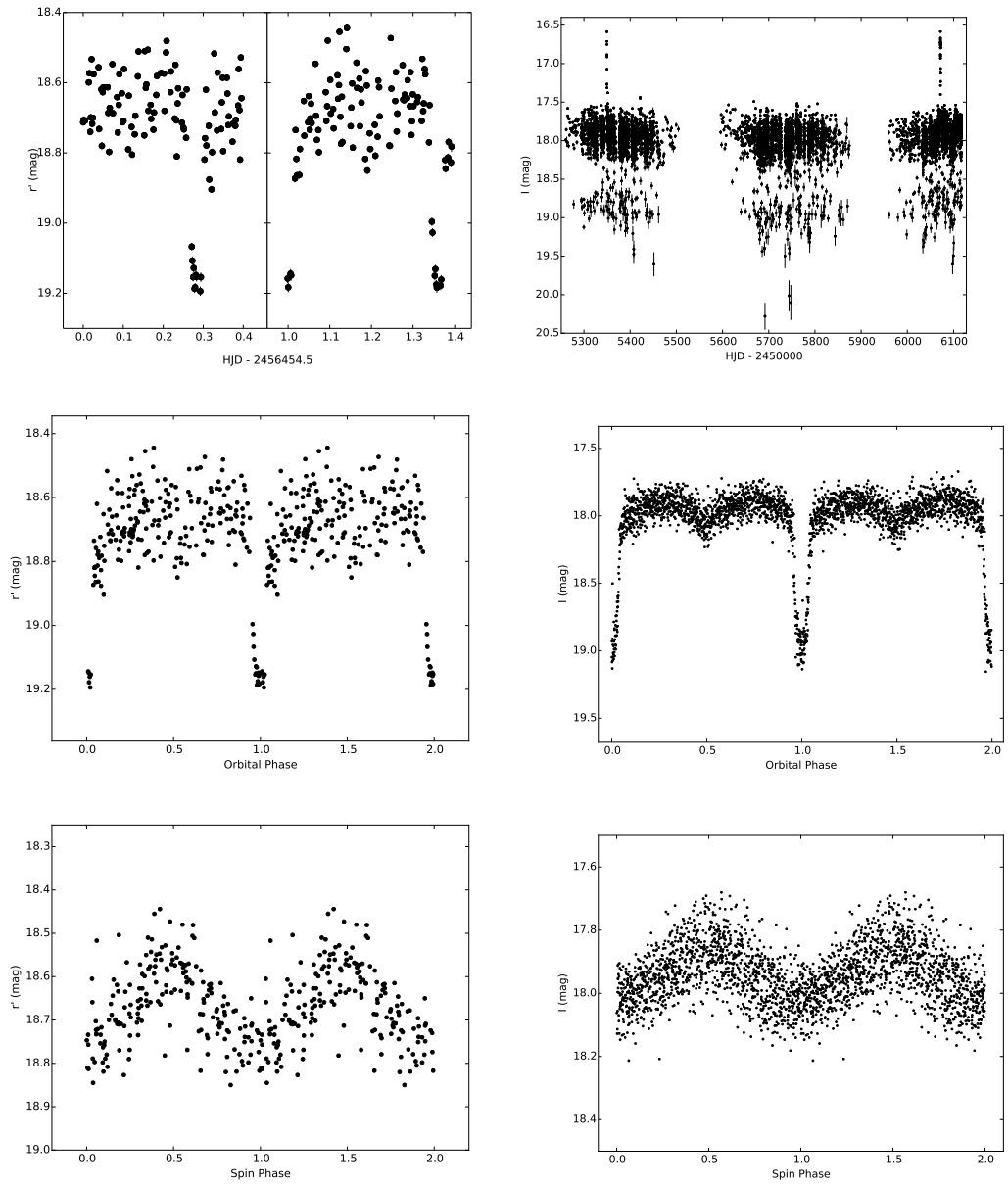

Figure 4.3: CX19 data sets. The left column is the r' DECam data and the right column is the OGLE I-band data. The middle-left panel is folded on $P_{orb} = 0.358$ days is also binned in phase bins of three consecutive data points to show the secondary eclipse more clearly. The bottom panel is the light curve folded on the $P_{spin} = 504.4$ seconds without binning. The I-band OGLE light curve and the phase-folded light curve using $P_{orb} = 0.358704$ days can be seen in the top and middle panel of the right column, respectively. The bottom right panel shows the OGLE light curve folded on the spin period of $P_{spin} = 503.32$ secs. Note that the eclipses have been removed from the spin-folded light curves.

and T_{obs} is the observed HJD for each data point. Our best fits yield the following times of middle eclipse: HJD = 2456454.8144(5), 2456455.5331(5) and 2456455.8940(5).

The spin periods recovered (from DECam and OGLE) differ by about a second. This is probably due to the insufficient sampling of DECam. The middle right panel of Figure 4.3 shows a mean out-of-eclipse I-band magnitude of 17.91(5), an eclipse depth of 1.1 mags and eclipse duration of ∼46 mins. The OGLE light curve is remarkably stable over the 3 year baseline and there does not appear to be any evidence of the source entering a low-accretion state.

Due to the longer baseline of data (OGLE compared to DECam) and the minute differences between periods, we are inclined to adopt the the fundamental parameters of CX19 as P_{orb} = 0.358704(2) days and P_{spin} = 0.0058718(3) days = 503.32(3) secs.

With the refined period from the OGLE data, we then used the parabolic fitting technique described above to fit a function to the phase-folded OGLE data to find the best fit for the epoch, T_0, and ephemeris. With a $\chi^2_{red} = 3.34$ (410 degrees of freedom), we find the best fit to be:

$$\text{HJD(eclipse)} = 2455691.8581(5) + 0.358704(2) \times N \tag{4.2}$$

4.4 Optical Outbursts

Upon inspecting the OGLE data, two optical outbursts were discovered and can be seen in a close-up view in Figure 4.4. Since we do not observe the beginning of the outbursts, we can only place lower limits on the duration and amplitude. The first outburst occurred in 2010 (HJD = 2455349) (left panel of Figure 4.4) with a peak I = 16.58, approximately 1.3 mag brighter than the mean out-of-eclipse brightness of 17.91. From the observed peak until the end of the observation, the outburst lasts ∼6.2 hours. The second outburst occurred in 2012 (HJD = 2456071) (right panel of Figure 4.4) and is similar in observed peak brightness

reaching an I magnitude of 16.60, but lasting for ∼8.6 hours. Given the ephemeris in equation 4.2, we find that the outburst profiles have been superimposed on the eclipse events expected to occur at HJD = 2455349.6544(5) for the first outburst and HJD = 2456071.7256(5) for the second. The dashed lines in Figure 4.4 represent the times of middle eclipse and the x-axis timeframe is about 3 days.

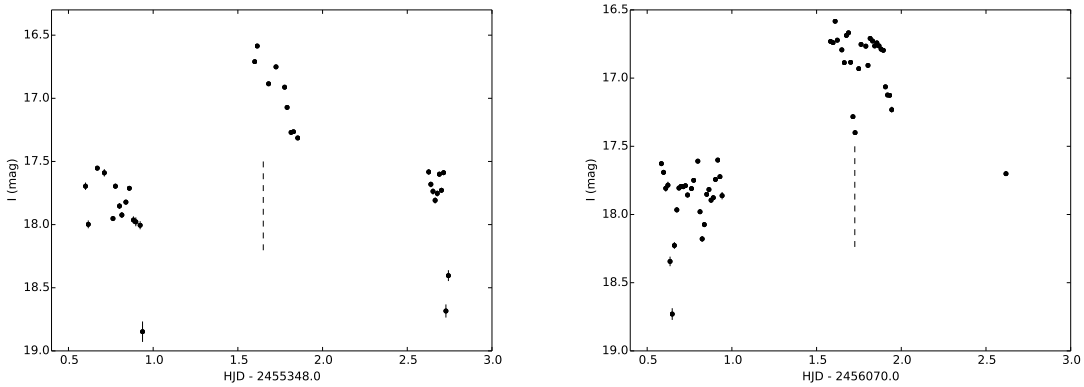

Figure 4.4: The two outbursts seen in the OGLE data in 2010 and 2012 (top and bottom panel, respectively). The dashed lines represent where the times of mid-eclipse occur using Equation 4.2.

Optical outbursts such as those seen in Figure 4.4 have also been observed in several magnetic CV systems, most notably in the IPs TV Col and V1223 Sgr (van Amerongen & van Paradijs, 1989). V1223 Sgr has shown outbursts lasting <1 day and >1 mag-amplitude, similar to the CX19 outbursts. In the case of EX Hya, outbursts have been observed to reach 4 magnitudes in amplitude lasting for ∼2 days. It is thought that these outbursts are a consequence of *either* an increased mass transfer rate from the secondary star *or* by an instability in the accretion disk itself (Angelini & Verbunt, 1989). The idea behind the short outbursts in IPs can be explained in terms of the magnetosphere radius. As the temperature in the outer disk region rises, the high-temperature region gradually starts moving inwards. The result being that the optical brightness increases to maximum rather quickly before the ultraviolet brightness maximum and is shortened by the inner disk radius, which, in turn,

is shortened by the magnetosphere radius. Similar to CX19, three outbursts were seen in TV Col lasting 6–12 hours in the range of ∼2 mag (Szkody & Mateo, 1984). Angelini & Verbunt (1989) offers the brief explanation of a small disk around a large magnetosphere to account for the short outburst duration. These IP outbursts are very different from DNe outbursts with respect to duration and amplitude and are characteristic of several IPs now. The emission features from IPs are completely dominated by the energy released from the accretion onto the magnetized poles of the WD.

4.5 X-ray Spectrum and Eclipse

After reprocessing the CXO data for each of the three OBSIDs (8742, 8753 and 9563), the X-ray data were extracted from all the event files. We extracted a total of 425 counts in the range of 0.3–8.0 keV, the softest being 0.51 keV and the hardest being 7.68 keV. The majority of counts reside in the hard X-ray regime >4.0 keV. We define the hardness ratio as HR = $(H - S)/(H + S)$, where S and H are the soft (0.3–2.5 keV) and hard (2.5–8 keV) energy band count rates (Jonker et al. 2011). We find a hardness ratio of HR = 0.70 ± 0.03 derived from the distribution of X-ray counts making CX19 a hard X-ray source.

The X-ray light curve is presented in Figure 4.5 grouped in bins of 100 seconds. We uncovered an X-ray eclipse in the middle of the 15 ks exposure (OBSID 9563) which appears to be a total eclipse lasting ∼31 mins. The X-ray light curve shows variability by a factor of ∼2 on timescales of several minutes outside of the eclipse although we do not detect any spin modulation in the data.

We then used the specextract CIAO tool to extract spectra and backgrounds, and create response files for all three observations. We grouped the longer OBSID 9563 spectrum by 20 counts/bin and combined the OBSID 8742 and 8753 spectra into one spectrum, which we binned by 10 counts/bin. We fit both spectra with simple models in XSPEC, starting with an

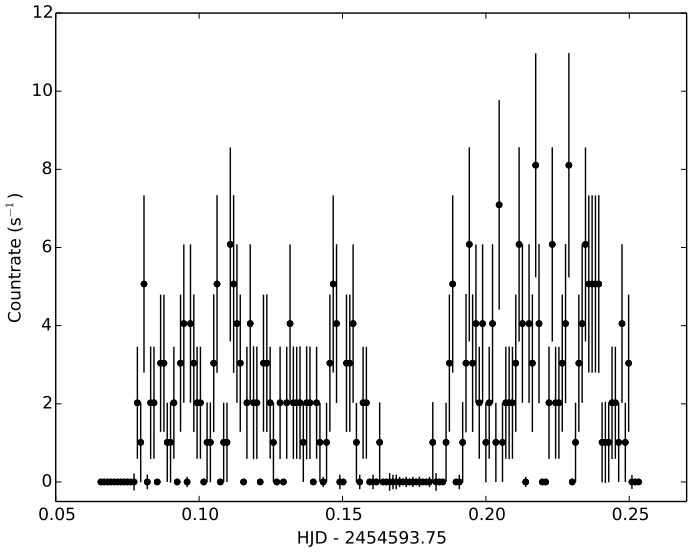

Figure 4.5: The 0.3–8.0 keV X-ray light curve of CX19 binned in 100 second bins showing an X-ray eclipse.

absorbed power-law (using abundances from Wilms et al. 2001). XSPEC is an X-ray spectral fitting program used in CIAO to compare different models when analyzing X-ray spectra. Initially, the observed spectra with background measurements and instrumental responses are supplied by the user, then a set of model spectra are chosen from several different models in the program. Then a predicted spectrum is calculated from input parameters such as temperature and Galactic absorption, N_H, and is compared to the spectrum obtained by the instrument. The values of the parameters of the model are manipulated until the best fit model describes the actual spectrum using χ^2 minimization.

The power-law fit, which forces both spectra to have the same parameters, is poor (χ^2_{red} = 1.89 for 16 degrees of freedom), and shows an excess of unmodeled flux in the OBSID 9563 spectrum at low energies. Allowing the N_H and normalization to differ between observations gives an acceptable fit (χ^2_{red}=1.05), but the power-law index is then forced to -0.4.

Considering the identification of this source as a intermediate polar, we tried a partial covering absorber with a high-temperature (fixed to 30 keV) mekal (thermal plasma,

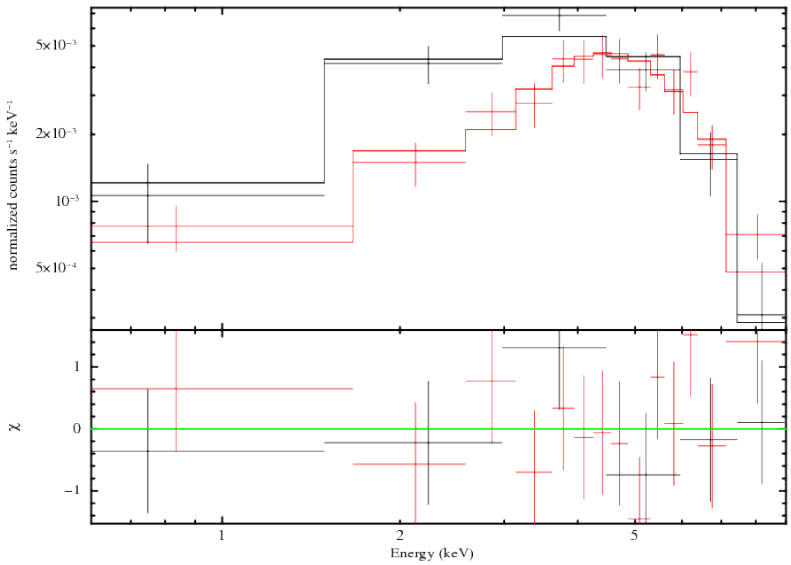

Figure 4.6: X-ray spectral energy distribution and best fit. The top panel shows two spectral fits: OBSID 9563 (red) and the combined spectra of OBSIDs 8742 and 8753 (black). The bottom panel shows the residuals from each fit.

bremsstrahlung dominated; e.g. Liedahl et al. 1995) model, as has typically been used to describe intermediate polars (e.g. Norton & Watson 1989). The mekal model tries to model the emission spectrum from a hot, diffuse gas based on the calculations by Liedahl et al. (1995). Thus, the model is tbabs×pcfabs×mekal, where, in the XSPEC program the parameters "tabs" and "pcfabs" are the Galactic absorption and intrinsic absorption, respectively. We set the tbabs and pcfabs parameters between the spectra, but permit the covering fraction and mekal normalization to be free between the spectra. This gives an excellent fit (reduced $\chi^2_{\rm red}$=0.84 for 14 degrees of freedom), and is shown in Figure 4.6. In this fit, the Galactic absorption is $1.7^{+1.2}_{-0.9} \times 10^{22}$ cm^{-2}, the partial absorber is $23^{+12}_{-7} \times 10^{22}$ cm^{-2}, the covering fractions are 91^{+4}_{-6}% and 79^{+11}_{-21}% (for the longer and shorter observations respectively). The implied intrinsic 0.5–10 keV fluxes are 3.0×10^{-12} and 4.0×10^{-12} ergs cm^{-2} s^{-1}, for the longer and shorter observations respectively. This includes correction of the longer observations flux for the ∼20% of the exposure during eclipse. At the minimum distance of 2.1 kpc (see Section 4.7), this converts to a 0.5–10 keV luminosity of $1.5 - 2.0 \times 10^{33}$ erg/s. This is

somewhat high for CVs, but not unprecedented for magnetic CVs, especially those that are X-ray selected (e.g. Beuermann et al. 2004, Pretorius & Mukai 2014).

4.6 Spectroscopic Features

The averaged VIMOS spectrum of CX19 (Figure 5.1, left panel) shows Hα in emission with a broad and single-peaked line profile with intrinsic FWHM of 850 ± 20 km s^{-1} and EW $= 23.2 \pm 0.2$ Å. HeI $\lambda 5876, 6678$ are also in emission, but weaker (EW ~ 3 Å). At longer wavelengths, CX19 shows the emission lines P12/11/10/9 λ8750/8863/9015/9229 of the Paschen series where P_n stands for the Paschen $n-3$ transition. The lines are broad (~ 1400 km s^{-1} FWHM) with P9 being the strongest of them. In addition to the saturated interstellar NaD doublet, DIBs at λ5780 and λ6284 appear to be present, but affected by residual emission from the sky background. Photospheric lines from the donor star are not detected, in particular, there is no definitive evidence of the CaII triplet in absorption or emission. The VIMOS observation covered orbital phases $0.89 - 0.95$.

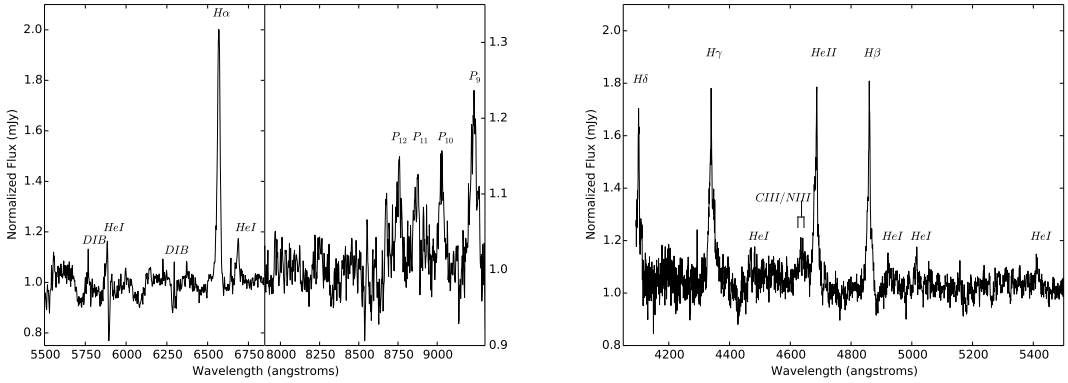

Figure 4.7: Normalized and averaged spectra of CX19 obtained with VIMOS (left panel) and FORS2 (right panel). The most prominent features are labeled.

The right panel of Figure 5.1 shows the averaged FORS2 observations. The blue coverage and spectral resolution provided by the data allows us to detect and characterize emission

lines from Hγ, Hβ and HeII λ4686. Their line profiles are composed of a broad and a red-shifted narrow component. From a 1D-Gaussian fit, we derive the lines' Heliocentric radial velocities and FWHMs which are given in Table 4.1. This table also provides equivalent widths (EWs) and the line parameters for the Hα line in the VIMOS observation. The FWHMs are corrected from the instrumental resolution. The Hβ and HeII lines have similar broadening and strength (840-940 km s^{-1} FWHM, $\sim$ 10 Å EW). Weaker CIII/NIII Bowen blend near λ4640 and HeI λ5412 are also present. The narrow emission line component from HeI $\lambda\lambda 4912, 5016$ is also visible while HeI λ4471 is not detected. Photospheric features from the WD or donor star are absent except perhaps for a feature at λ5712 that matches the expected position for Mg, however this could be an artifact. Other absorption features at $\lambda\lambda 4428, 4882$ are diffuse interstellar bands.

The FORS2 observations covered orbital phases 0.01–0.84 with a phase resolution of 0.014. Figure 4.8 shows a hint at the phase dependence for the HeII and Hβ emission lines. We can see that the high velocity wings of the HeII λ4686 seem to get stronger and narrower when approaching primary eclipse (phase 0.01). Similar results have been seen in other IPs (for example, EX Hya; Hellier et al. 1987) showing narrowing, and slight intensity enhancement of the HeII λ4686 line. In EX Hya and FO Aqr, modulations in HeII λ4686 have led to the realization that the inclination angle must be quite high (Warner, 2003). Since we have only obtained five spectra with insufficient time resolution, we cannot confirm that a modulation is present on the P_{orb} or P_{spin}.

There have been many IPs studied spectroscopically showing not one, but two or more emission line profile components. (Hellier et al., 1987) found a double-peaked line profile tracing the disk velocity and also a broad component modulated on the 67 min spin period for EX Hya. The unpulsed, double-peaked emission profile originates in the accretion material orbiting the WD and is strong evidence for an accretion disk in IPs.

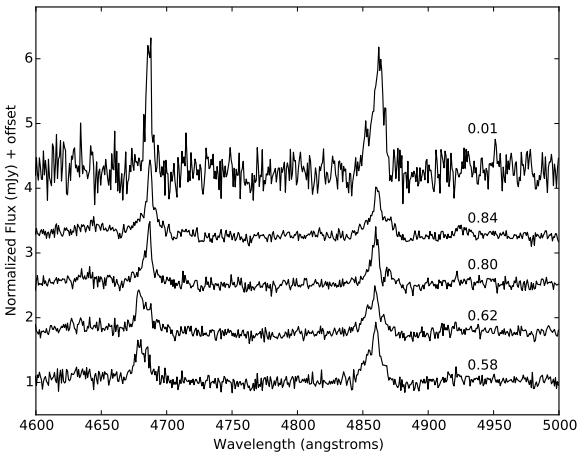

Figure 4.8: A zoom-in of the FORS2 spectra and the evolution of the line profile for the HeII line and the Hβ line. Each FORS2 spectrum is labeled corresponding to the orbital phases 0.58, 0.62, 0.80, 0.84 and 0.01.

Table 4.1: Spectroscopic measurements of line profiles

Line	RV (km/s)	EW (Å)	FWHM (Å)
Hγ	-20 ± 20	13.6 ± 0.3	20.7 ± 0.8
HeII λ4686	-80 ± 20	10.2 ± 0.2	14.6 ± 0.6
Hβ	-110 ± 10	9.8 ± 0.2	13.6 ± 0.4
Hα	230 ± 8	23.2 ± 0.2	18.0 ± 0.4

4.7 Distance Estimate

To calculate an approximate distance, we began by estimating the spectral type of the donor star from the density-period relation given by:

$$\rho \cong 110 \times \mathrm{P}_{\mathrm{orb,hr}}^{-2} \text{ g cm}^{-3} \tag{4.3}$$

where the orbital period is given in hours (Frank et al., 2002). We find an approximate density of $\rho \approx 1.5$ g cm^{-3} which is consistent with a G3V–G5V spectral type donor using

densities from Allen (1973). In our calculation for the distance estimate, we will assume a main sequence companion, although we point out that it is more likely a less dense, late-type star which is usually seen in longer period systems.

In an attempt to estimate the reddening, we determine the observed (R–I) color of CX19 using the I-band magnitude (in eclipse) of I = 19.05 ± 0.01 and the transformation equations between Johnson-Cousins and SDSS u'g'r'i'z' magnitudes derived by Lupton et al. (2001). We do point out that the tranformation equations may be unreliable for redder and/or non-stellar spectra. The observed color, (R–I) ≈ -0.13, is much bluer than the intrinsic color of known G3V-G5V stars (≈ 0.35–0.36) compiled in Eric Mamajek's online stellar tables[2]. This is expected since the spectrum is disk dominated without any apparent absorption features from the donor star. We estimate the maximum extinction to the source by using the "Bulge Extinction and Metallicity Calculator" (BEAM)[3]. BEAM is a Bulge extinction and metallicity calculator based on the method of Gonzalez et al. (2011) using the J-K_s colors of red clump (RC) giants and compare them to the color of RC stars in Baade's window. A small redding map was created for the region and the dereddened magnitudes were used to build the Bulge luminosity function in regions of 0.4°×0.4° to obtain mean RC magnitudes. The BEAM online extinction tool gives $A_K \approx 0.7180$ for a radius of 1.1' centered at the source coordinates of CX19. Since the G-type star does not have to be an ordinary main sequence star (especially since it is in an interacting binary system), we can calculate a distance estimate based on the following assumptions concerning extinction and absolute magnitude. We use the I-band magnitude from OGLE, $A_K = 0.225 \times A_I$ (Allen, 1973), the absolute magnitude of a G5 type star ($M_I = 4.242$), and the apparent magnitude

[2]http://www.pas.rochester.edu/∼emamajek/
[3]http://mill.astro.puc.cl/BEAM/calculator.php

($m_I = 19.05$). The distance modulus:

$$m_I - M_I = 5 \log d - 5 + A_I \tag{4.4}$$

or rearranging:

$$d = 10^{0.2(m_I - M_I + 5 - A_I)} \tag{4.5}$$

we find a minimum distance of $d \approx 2.1$ kpc for a MS G5 star. The caveat to this estimate is that we are assuming that this is a main sequence companion. If the spectral type is later, then the absolute magnitude, M_I, could be >4.242 and the distance estimate would be <2.1 kpc.

4.8 Discussion

At the time of writing (January 2016), the list of confirmed IPs composed by K. Mukai[4] contains 47 systems. Among the confirmed IPs, the orbital period range spans from about 0.05–2.0 days. The WD spin period ranges from ∼33–4000 seconds. Mukai's IP list contains seven systems that show confirmed eclipses, five of which are labeled as grazing/partial: FO Aqr, TV Col, EX Hya, BG CMi and V598 Peg. The other two, DQ Her ($P_{orb} = 4.646$ hr) and XY Ari ($P_{orb} = 6.064$ hr), are deeply eclipsing IPs. It has been shown previously that there appears to be a loose relation between the two periods inherent in most IP systems, mainly $P_{spin}/P_{orb} \sim 0.1$ for systems with $P_{orb} < 5.0$ hours. The most extreme systems in the list have $P_{spin}/P_{orb} < 0.01$ and are found at very long orbital periods, i.e. GK Per ($P_{orb} =$ 47.9 hrs). CX19 has a $P_{spin}/P_{orb} = 0.016$ as would be expected for a long orbital period IP. We classify CX19 as a deeply-eclipsing IP system with an average magnitude depth of Δ mag ~ 1.1 in the I-band. Warner & Woudt (2009) identified V597 Pup as the third deeply

[4]http://asd.gsfc.nasa.gov/Koji.Mukai/iphome/iphome.html

eclipsing IP and Aungwerojwit et al. (2012) presented the fourth deeply eclipsing IP, IPHAS J0627, with a $P_{spin}/P_{orb} = 0.075$ and an eclipse depth of Δ mag $\sim$1.5. CX19 is the fifth system to exhibit deep optical eclipses.

Norton et al. (2004) showed through a series of modeling that there exists a relation for a large range of P_{spin}/P_{orb} and WD magnetic moments, μ_{WD}, for magnetic CVs. This relation is illustrated in Figure 2 of Norton et al. (2004) for an assumed mass ratio of $q = M_2/M_1$, where M_2 and M_1 are the donor star and WD masses. As an estimate for the magnetic moment of CX19, we use a $P_{orb} = 0.358704$ days or $\sim$ 8 h and $P_{spin}/P_{orb} \sim 0.02$ in their Figure 2 to find a very conservative magnetic moment of the WD of μ_{WD} $\sim$1–2 $\times$ 10^{33} G cm^3. For a longer period IP, this is a relatively high magnetic moment and the system is most likely going to evolve in to a synchronous polar.

The similar strengths and FWHMs observed for the Balmer and HeII λ4686 lines in CX19 resemble the emission line properties of the 9.81 hr orbital period IP RXS J154814.5-452845, although in this system, both WD and donor star have been detected in the optical spectra (de Martino et al. 2006). The emission lines of CX19 do appear to be stronger at mid-eclipse than outside eclipse, indicating that the source of their emission is less concentrated towards the orbital plane than the source of the continuum.

We can build a picture of the IP system CX19 based on all the preceding observed and calculated parameters. First, if an accretion disk is present and truncated at some magnetosphere radius, r_μ, it must be smaller than the circularization radius, r_{circ}. We can place an upper limit on r_{circ} by estimating the Roche lobe radii of the binary system. If we use the analytic formula for the Roche Lobe radius from Equation 1.4 and the initial parameters of $M_2 = 0.99$ $M_\odot$ for an average G3V–G5V type star, $R_2 = R_{L,2} = 1.0$ $R_\odot$ and a WD mass of $M_1 = 0.6$ $M_\odot$ (this mass ratio would cause unstable mass transfer, but we use these numbers as estimates), we find $R_{L,1} = 0.83$ $R_\odot$. We know that the $R_{circ} < R_{L,1}$ for the

transferring gas to orbit in a Keplerian orbit after passing through the first Lagrange point. We can then place an upper limit on R_{circ} using the relation:

$$\frac{R_{\rm circ}}{a} = (1+q)[0.500 - 0.227 \times \log(q)]^4 \tag{4.6}$$

We find that the $R_{circ} \approx 0.3\ R_{\odot} \approx 0.36 \times R_{L,1}$ meaning that the R_{μ} must be much smaller than this. For a comparison, Allan et al. (1996) found a disk radius of $0.3 \times R_{L,1} < R_{disk} < 0.45 \times R_{L,1}$ when modeling the light curve of XY Ari showing that our estimate is consistent. A more massive WD with $M_1 = 1.2\ M_{\odot}$ would give us $R_{circ} \approx 0.14 \times R_{L,1}$.

XY Ari is the only other IP that has been confirmed to have both deep eclipses in two different bandpasses, the IR *and* X-ray (Hellier, 1997). XY Ari shows X-ray eclipses recurring with a 6.06 h orbital period but since it is hidden behind the the molecular cloud Lynds 1457, the optical flux is extinguished to V>23. The X-ray light curve of XY Ari also exhibits a clear, pulsed 206 second spin period out-of eclipse. CX19 shows an X-ray eclipse in Figure 4.5 lasting for ∼0.06 of the phase coverage or ∼31 min, with no clear modulation out-of-eclipse. To our knowledge, CX19 is the first X-ray selected IP that shows clear deep-eclipses in both the optical and X-ray.

4.9 Future Work for CX19

The optical photometry and spectroscopy analysed in Johnson et al. (2014b) will provide the groundwork for future observations of CX19 helping to constrain the orbital parameters of the system. With the supplied eclipse timings and ephemeris, one can estimate future times of eclipse (or gather archival photometry if available) and construct O-C curves to look for period changes. These period changes could be the result of a mass ejection or magnetic braking effects from the strong magnetic field of the WD. Time series photometry during mid eclipse can be compared to light curve models to help constrain the inclination

angle (the one parameter that we have no concrete limit for). High resolution time series spectroscopy can provide a radial velocity curve (if we see any donor lines), which, coupled with the inclination angle, can place limits on the total mass of the system and the mass of the WD. Spectroscopic studies of the emission lines also provide the WD spin period through pulsations which manifest themselves in the disk. These pulsations are seen as equivalent width modulations in spectroscopic emission line profiles such as HeI λ4471 and HeII λ 4686. Further X-ray timings are needed to confirm whether or not the WD spin period is present in the X-ray light curve.

5. CX514: A Slowly Pulsating B Star

In this chapter, I discuss the GBS X-ray source CXOGBS J175637.0-271145 = CX514 for which we obtained optical photometry and spectroscopy, accompanied by archival photometry from ASAS. We show that CX514 is a new Slowly Pulsating B (SPB) star containing several photometric frequencies, none of which are the orbital period of the binary system. The second component in the binary appears to be *either* a WD or (more likely) an active G-type star and the X-rays may originate from coronal activity. All the figures in this chapter are the author's original work and reproduced with permission from (Johnson et al., 2014b).

5.1 Introduction

Early type stars have been known to be X-ray sources for quite some time now. The existence of X-ray emission from massive O and B stars was predicted decades ago by Cassinelli & Olson (1979) and was serendipitously discovered at the same time during early observations using the Einstein satellite. The X-ray properties of O and B stars were constrained more accurately by Berghoefer et al. (1997) using the ROSAT All-Sky Survey (RASS). Equipped with 237 detections, Berghoefer et al. (1997) confirmed the decline in the detection rate toward later spectral types (all stars of spectral type O7 or earlier were detected as X-ray sources, while at most 10 % of B3–B9 stars were detected). This fact, and a higher incidence of variability and binarity among the later spectral types, led to the conclusion that low-mass companions could be responsible for the X-ray emission of late B-type stars. This can be interpreted in one of two ways. (1) A matter stream exists between the B star and a compact companion due to Roche lobe overflow (RLOF). The stripped matter impacts the accretion disk causing X-ray emission at the impact point. (2) The low mass companion is coronally

active, which is to be expected since such companions must be very young and have not had enough time to slow their rotational speed yet.

The GBS X-ray source CXOGBS J175637.0-271145 = CX514 (V = 10.04 mag) has coordinates that align with HD314884, initially classified as a B9 star (Nesterov et al., 1995). CX514 was found to have an X-ray luminosity of at least 1.3×10^{30} erg s^{-1} and $\log(\frac{F_{\rm x}}{F_{\rm bol}})$ = -5.4 (Hynes et al., 2012), neither of which is consistent with a single late-type B star. We infer that this is either a chance alignment with HD314884 or that the X-ray source is the binary companion to the B star. The 95% confidence radius of uncertainty in the Chandra position is 3.4". The optical counterpart to CX514 (HD314884) has also been identified as a new All Sky Automated Survey (ASAS) Catalogue (Pojmanski, 2002) variable source ASAS ID# 175637-2711.8. We initially followed up on this source due to the possibility that it could be an XRB analogous to 4U1543-47 (Orosz et al., 1998), which contains a 3 $M_\odot$ BH and A2V companion.

5.2 Spectral Classification and Features

We began the spectral classification by comparing the spectral range 3900–5100 Å of the counterpart obtained from the 2.0 m Liverpool Telescope (see Section 2.5) to several known Morgan-Keenan (MK) standard stars of spectral type B. By visual inspection of Figure 5.1, we can see the weak presence of several HeI lines along with the CII and MgII lines. The most notable lines are the Balmer lines with the presence of HeI lines of λ4026, λ4143, λ4387 and λ4471. Several helium and metal lines can be used to aid in classifying the spectrum of the counterpart. The HeI λ4009 is prominent down to spectral type B3, then starts to get weaker at B5 before disappearing at B8. This feature is very weak in the spectrum of HD314884. The ratio of HeI λ4471/MgII λ4481 is also a useful indicator to help distinguish between mid- to late-type B stars. The neutral HeI λ4471 line weakens and disappears as

the MgII λ4481 strengthens when approaching lower temperatures (Gray & Corbally, 2009) in late-type B stars.

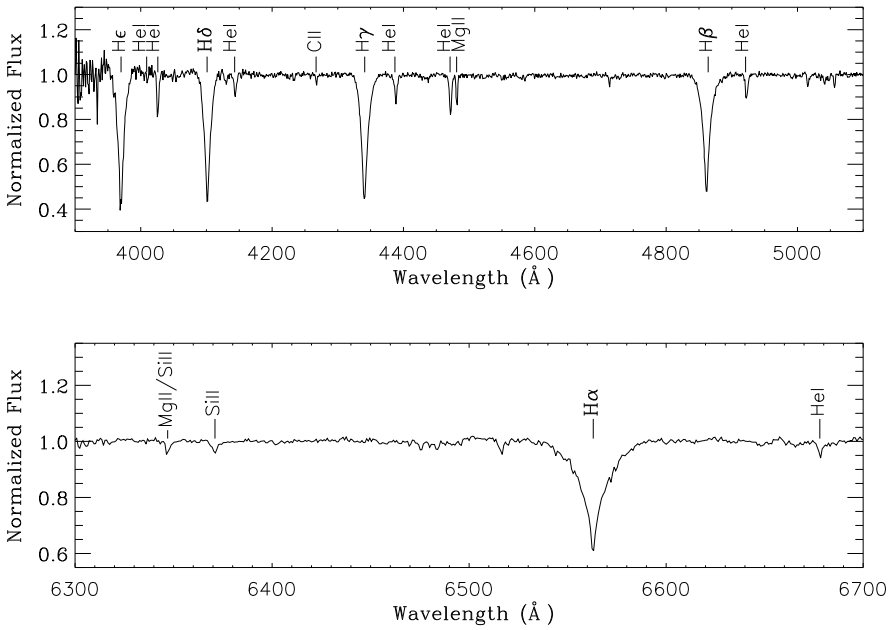

Figure 5.1: Normalized spectra of HD314884 with the top panel showing the blue end and the bottom showing the red end of the spectrum. Prominent spectral lines are marked.

We measured the HeI λ4471/MgII λ4481 ratio to be 1.42 $\pm$ 0.02 for all 22 spectra. We rule out spectral classes B8V–B9V based on the HeI λ4471/MgII λ4481 ratio < 1.00 due to the stronger MgII λ4481 as the T_{eff} approaches cooler temperatures. We then measured the HeI λ4471/MgII λ4481 ratio for several MK standards of types B0V–B9V as a comparison. On average, the B0V–B4V spectra had a HeI λ4471/MgII λ4481 ratio $> 1.55 \pm 0.02$. We find that these indicators, along with the weakness of CII λ4267, point to a B5V–B6V classification for the optical counterpart.

A grid of synthetic spectra (Munari et al., 2005) was then used to match the absorption features to determine approximate spectral parameters of the optical counterpart. We subtracted each template spectrum from the Doppler-corrected average of the observations.

The grid of spectra included B4V–B7V stars with varying T_{eff} and $\log g$. We adopt a $v_r \sin i$ = 45 km s^{-1} from our initial best fit of the line widths to the synthetic line profiles. At every point on the synthetic spectra grid, the best fit was found by performing a χ^2 minimization on the residuals of the subtraction. The best fit obtained shows HD314884 as having a T_{eff} = 15,490 ± 310 K and $\log g = 3.75 \pm 0.25$ dex. From our spectral analysis, the values obtained are in agreement with known B5V–B6V stars contained in Eric Mamajek's online list[1]. We point out that there appear to be no emission lines present in Figure 5.1 which argues against mass transfer from the donor star. We confirm this by Doppler correcting and broadening our Liverpool spectra by an appropriate amount found by looking at the FWHM of the absorption lines in the spectral range 3900–5100 Å using IRAF and the SPLOT task. Since the absorption features are narrower than the template spectra, a broadening of 45 km s^{-1} was applied to each spectrum. The narrow absorption lines make sense since binary systems can be tidally locked slowing down the rotation rate of the stellar components, whereas isolated late-type stars rotate much faster and have broader lines. In a similar manner as above, we then subtracted each from an MK spectral standard B6V template spectrum confirming the absence of residual emission.

5.3 Photometric Period Analysis

Using the ASAS-3 archival data, we next performed an initial period search on the data using the software package PERIOD (see Section 3.3) in the frequency range of 0.01–1000 cycles/day in frequency intervals of 0.00001 cycles/day. We used the Lomb-Scargle technique to produce a periodogram and search for the maximum peak in the power spectrum for a given data set.

[1] http://www.pas.rochester.edu/∼emamajek/spt/B6V.txt

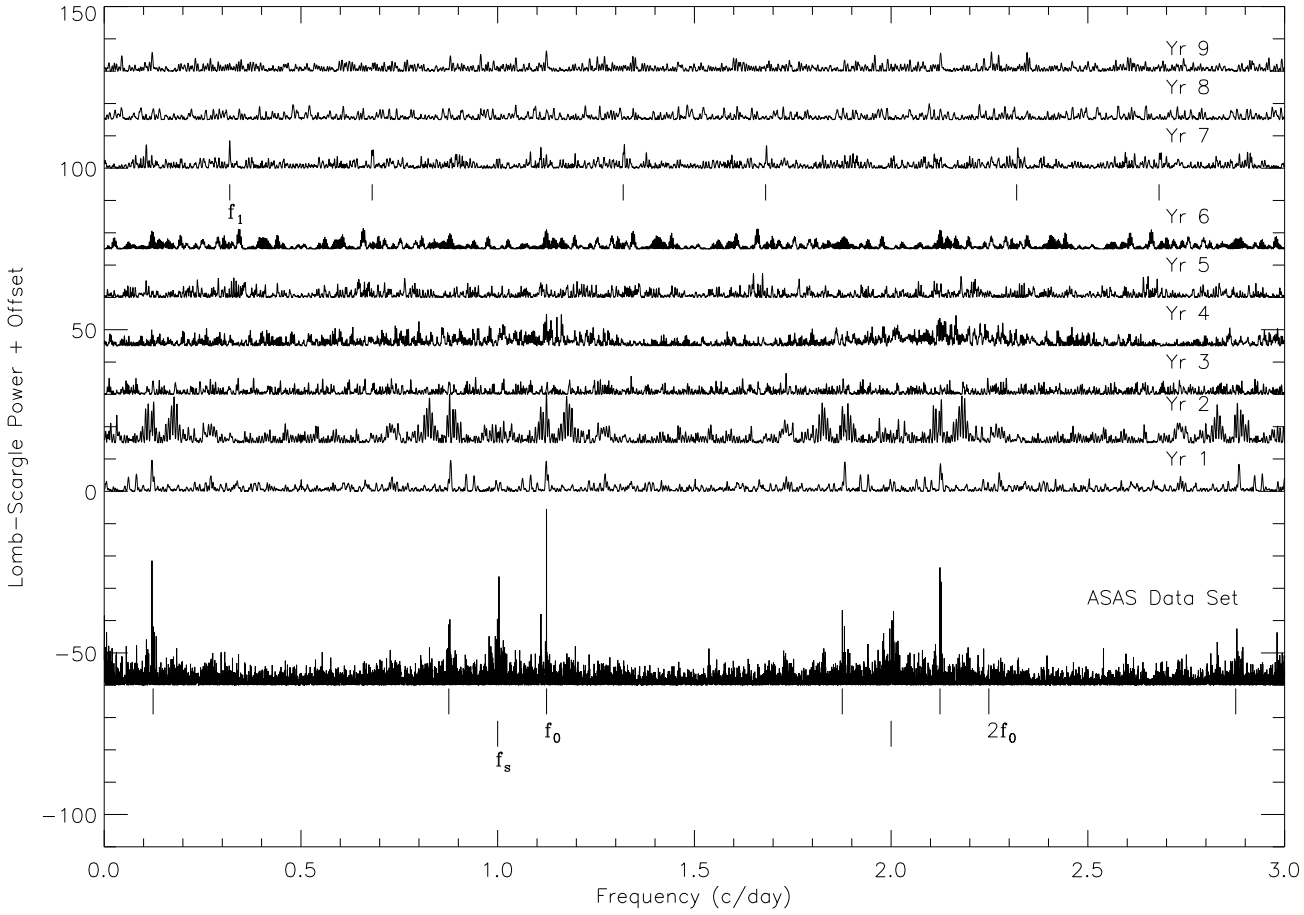

Figure 5.2: Yearly Lomb-Scargle periodograms of HD314884 where 2001 is year 1. The bottom data set is the entire ASAS-3 data set. Several frequency peaks are labeled: f_0 corresponds to the 0.889 day period and the aliases; f_s is the one day sampling frequency and aliases; $2f_0$ is the second harmonic of f_0. f_1 corresponds to the second distinct period of 3.13 days and aliases. Year 7 shows f_1 the best.

The ASAS-3 period search confirmed the V-band photometric period of 0.889521(12) days which is within the quoted 1σ error of the photometric period reported by Hynes et al. (2012) along with the 8 day alias, the sampling frequencies, and the harmonics (all of which can be seen in Figure 5.2). The nine years of ASAS-3 archival data were inspected year by year and as a complete data set to look for any variations on the 0.889521(12) day period. Figure 5.2 shows the periodogram of the data. We identify two "distinct" frequencies when analyzing the data. The 0.889521(12) day period corresponds to a frequency 'f_0' and will be referred to as such. The second distinct frequency, 'f_1', corresponds to a 3.1347(56) day period and is found dominating year 7 of the data set in Figure 5.2. The aliases of f_1 are also labeled in the year 7 data. This signal is present in several other years, but weak. The f_0 frequency is recovered in years 1, 2, 4, 6, and 9, while no substantial frequency was recovered above the background noise in year 8. In Figure 5.2, we label the one day sampling frequency as 'f_s' along with its harmonics. Years 3 and 5 do not show any significant signal above the 3σ level for each of the two data sets.

A Lomb-Scargle frequency search of the 0.9 m SMARTS data concluded in a period of 1.517(28) days, corresponding to f_2. The light curve is shown in the middle panel of Figure 5.3. Neither f_0, nor f_1 were reproducible in the SMARTS data set and f_2 is not at all present above the noise in any of the yearly ASAS-3 data sets in Figure 5.2. Folding the SMARTS data on either of these frequencies does very little to convince us they are the correct frequencies for this data set and we conclude that f_2 is a *third* distinct photometric frequency of this system.

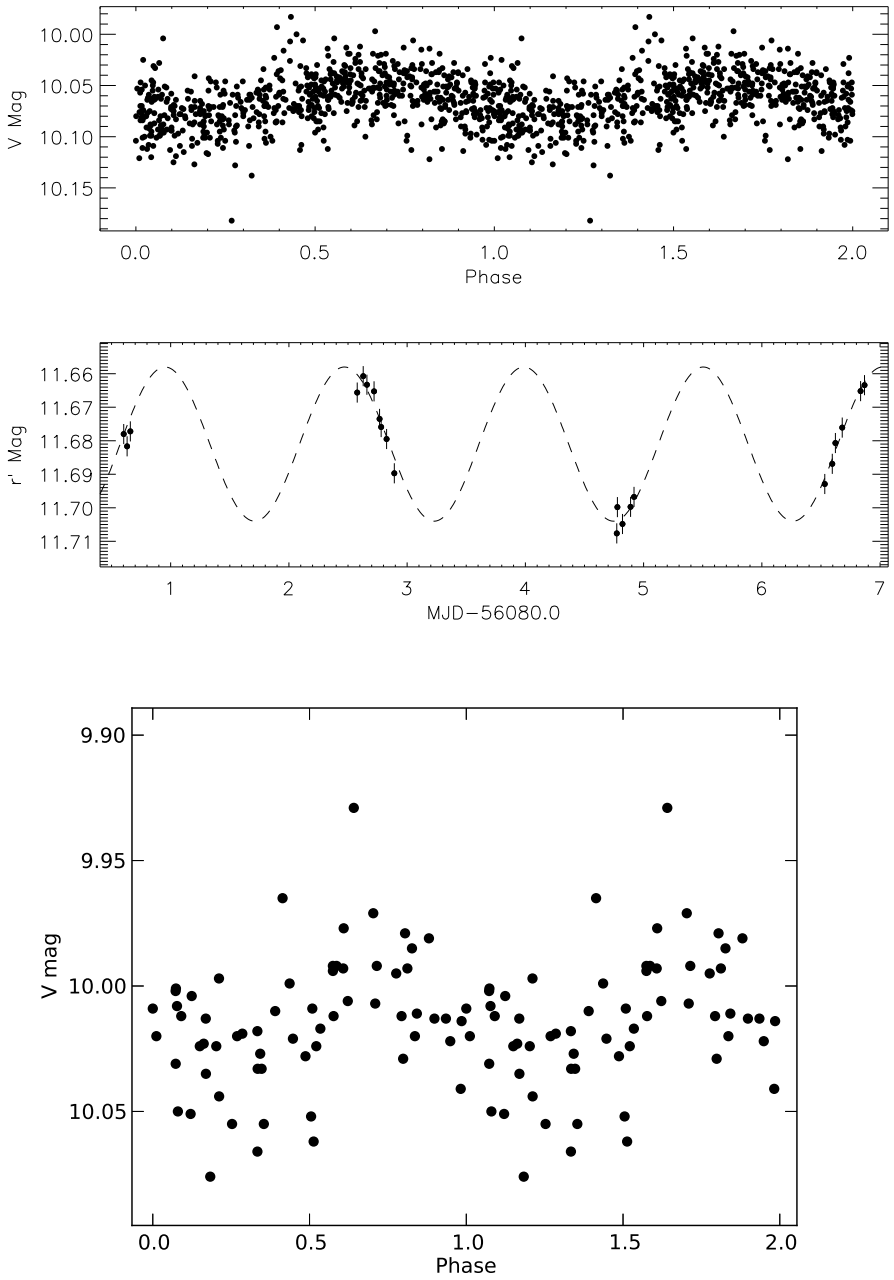

Figure 5.3: The top panel is the phase-folded light curve of the ASAS-3 archival data of HD314884 on the 0.889 day period. The middle panel is the 0.9 m SMARTS light curve with a 1.517(28) day period sine curve plotted over the HD314884 data. The bottom panel shows the phase folded light curve of the ASAS year 7 on the period corresponding to f_1 from Figure 5.2.

5.4 Dynamical Analysis

5.4.1 Radial Velocity Curve

The orbital Doppler shifts of the binary system consisting of HD314884 and its companion were measured from the MgII λ4481 absorption lines in the spectra. An MK standard B6V template spectrum was chosen and each subsequent target spectrum was cross-correlated against this reference. Using the FXCOR task with other standard IRAF tasks, the radial velocities were determined and a Lomb-Scargle period search was performed on the data. An initial orbital period of $P_{orb} = 1.3665(61)$ days was recovered.

The radial velocity curve was then fitted with a sine wave function of the form:

$$y(\phi) = \gamma + K_2 \sin(2\pi\phi + \psi) \tag{5.1}$$

where ϕ is the phase in the orbit, γ is the systemic velocity, K_2 is the semi-amplitude of the radial velocity curve and ψ is the phase offset. All the parameters were then allowed to vary and the best fit was found by using χ^2 minimization. We find that a $\chi^2 = 37.14$ and 21 degrees of freedom gives a $\chi^2_{red} = 1.76$ resulting in the following parameters:

$$P_{orb} = 1.3654 \pm 0.0011 \text{ days}$$
$$K_2 = 49.0 \pm 2.1 \text{ km s}^{-1}$$
$$\gamma = -15.4 \pm 0.6 \text{ km s}^{-1}$$
$$T_0 = 2456141.399 \pm 0.003 \text{ (HJD)}$$

The phase-folded radial velocity curve can be seen in Figure 5.4. The errors bars for the parameters are the result of $\Delta\chi^2$ except for P_{orb} which was found from the bootstrapping technique discussed in Section 3.3. The systemic velocity can be prone to systematic radial velocity calibration errors, but the independent sampling over multiple nights helps mitigate

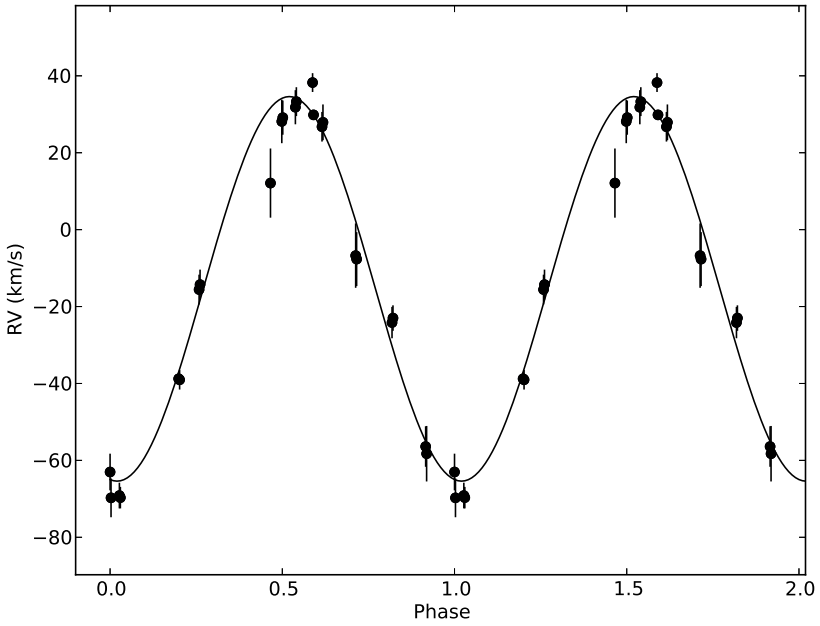

Figure 5.4: The phase-folded radial velocity curve of HD314884 and the unseen companion with the P_{orb} = 1.3654(11) days.

the problem. We then looked at the FWHM variations of several absorption features inherent in the spectra. For the MgII λ4481 line, we find that there is a peak in the Lomb-scargle periodogram at f_0 for the data. The phase-folded light curve of the FWHM of the MgII λ4481 line can be seen in Figure 5.5 with a folded period of 0.889521 days. There is an apparent modulation corresponding to the fundamental *photometric* period of HD314884, not to the *spectroscopic* period.

5.4.2 Masses of Stellar Components

The mass function of the unseen companion found from the given parameters is:

$$f(\mathrm{M}_1) : \mathrm{M}_1 \frac{\sin^3 i}{(1+q)^2} = \frac{P_{\mathrm{orb}} K_2^3}{2\pi G} = 0.0157(21)\ \mathrm{M}_\odot \tag{5.2}$$

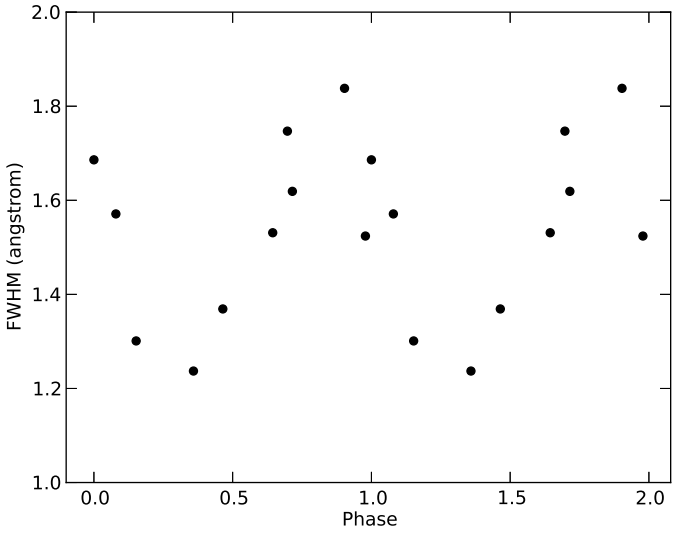

Figure 5.5: The FWHM variations of the MgII λ4481 spectral feature. The data is phase-folded on the 0.889521 day period.

where $q = \frac{M_2}{M_1}$ is the mass ratio in this case. The greatest uncertainty comes from the inclination angle, i, and the mass of the companion star, M_1, when calculating the mass function. To assess the most likely range of companion masses, we used a Monte Carlo method to sample random inclination angles distributed as $\sin i$ and assumed B5V–B6V mass range of 4.1 $M_\odot \leq M_2 \leq$ 4.5 $M_\odot$ (uniformly distributed). The result is a probability distribution of masses given these prior assumptions showing a peak at $\sim 0.8^{+0.3}_{-0.1}$ $M_\odot$ in Figure 5.6. The asymmetric errors quoted are due to the fact that the mass distribution is not Gaussian. This mass constraint places the unseen companion in the region of an active G-type star or a quite massive WD. For the mass distribution data set, we find that the 99% confidence region encloses a mass range of 0.6–2.3 $M_\odot$. Although this mass range does not rule out a neutron star X-ray source, it can rule out a black hole as the X-ray source unless it is of very low mass or the inclination is very low.

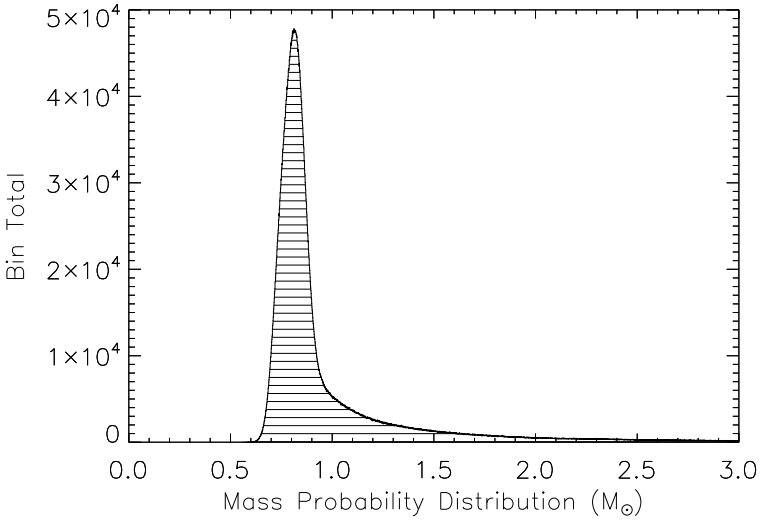

Figure 5.6: The mass distribution of the unseen companion generated by a Monte Carlo sampling routine for random inclination angles distributed as $\sin i$ and a B5V–B6V mass range of 4.1 $M_\odot \leq M_2 \leq$ 4.5 $M_\odot$ distributed uniformly. The peak corresponds to a most probable mass of $M_1 \approx 0.8\ M_\odot$.

5.5 Discussion

The main observational characteristics of SPBs are a mid-B spectral type and multi-periodic oscillations inherent in their light curves on the order of days. The oscillations can be characterised as either p-mode (frequencies on the order of ∼30 minutes) or g-mode (frequencies on the order of ∼days or longer) referring to pressure and gravity modes, respectively. The discovery of HD314884 as an SPB came as a surprise during our analysis of the GBS source CX514. After, the initial photometric period was confirmed using ASAS-3 data, two more distinct periods were uncovered in independent data sets that appear to be non-radial g-mode pulsations. Oscillation frequencies uncovered in photometric studies have frequently been used in precision mode identification to interpret the interior makeup of stars (Saesen et al., 2013) through the use of asteroseismologic techniques. The discrepancy between

the photometric periods and P_{orb} opens the door for this type of asteroseismic analysis on CX514.

Given $P_{orb} = 1.3654(11)$ days and a B star mass range of $4.1\ M_\odot \leq M_2 \leq 4.5\ M_\odot$, we expect an orbital separation of 8.8–9.0 $R_\odot$ making it one of the shortest known period, single-lined binaries containing an SPB, similar to HD24587 (Aerts et al., 1999), but significantly shorter than the SPB sample of De Cat et al. (2000). With the components being so close, tidal effects can play an important role in exciting pulsation frequencies through deformation of the stellar surface (De Cat et al., 2000). In a binary system with an eccentric orbit, a near resonance occurs when a stellar frequency is close to a multiple of the orbital frequency (Hambleton et al., 2012). Tidal resonance can also occur in close, circular orbits with the addition of g-mode frequencies summing to orbital harmonics. We find that $f_0 + f_1 \approx \mathbf{2}f_{orb}$ (1.124200(12) day^{-1} + 0.3190(6) day^{-1} = 1.4432(1) day^{-1}, where $f_{orb} = 0.7323(5)$ day^{-1}) indicating a type of higher order, non-linear tidal process (Weinberg et al., 2012). None of the identified frequencies found were *multiples* of the orbital frequency.

The FWHM variations of metallic absorption lines seen in Figure 5.5 are characteristic of SPBs. The modulation on photometric periods stems from temperature variations across the stellar surface during the pulsation cycle. When examining the spectra, CX514 shows a modulation in the MgII λ4481 absorption feature on the fundamental photometric period of 0.889521 days with an average broadening of 45 km s^{-1}. CX514 is considered a slow rotator and an ideal candidate for mode identification since fast rotators ($v_r \sin i \geq 100$ km s^{-1}) cause the photometric observables to become dependent not only on the mode degree, but also the azimuthal order, inclination angle, and rotation velocity (Szewczuk & Daszyńska-Daszkiewicz, 2012).

The spectral energy distribution (SED) can be seen in Figure 5.7. The SED is constructed with archival data from the *AAVSO Photometric All-Sky Survey DR7* (APASS; Henden et al. 2009) (circles), TYCHO (Hog et al. 1998) (diamonds), the *DEep Near Infrared Survey*

of the Southern Sky (DENIS; DENIS Consortium 2005) (triangles), the *2 Micron All-Sky Survey* (2MASS; Skrutskie et al. 2006) (pentagons) and the *Galactic Legacy Infrared Mid-Plane Survey Extraordinaire* (GLIMPSE; Benjamin et al. 2003) (squares). The model is a Kurucz solar metallicity atmosphere (Castelli & Kurucz, 2003) with a four way average of T_{eff} = 15,000 K, $\log g$ = 3.5,4.0 and T_{eff} = 16,000 K, $\log g$ = 3.5,4.0. If we assume the spectroscopic effective temperature derived above, we can fit this SED with an appropriate reddened Kurucz model atmosphere spectrum to estimate a reddening of $E(B-V) \sim 0.22$. Assuming a typical main-sequence absolute K magnitude from Mamajek's compiled list[1], the K band magnitudes from 2MASS and DENIS imply a distance of ∼1 kpc for HD314884. This suggests that HD314884 has an L_x of about 3×10^{30} erg s^{-1}.

If we assume an active G star as the companion to HD314884, we can describe the source of soft X-rays as coming from Solar-type coronal flares. We know from Solar observations that magnetic phenomena are solely responsible for coronal activity and, in turn, the production and detection of X-rays. The same holds true for Solar-like G stars except that stellar flare peak temperatures and emission measures can be orders of magnitude greater than that of the Sun (Johnstone et al., 2012). The range of L_x for G stars spans almost 3 orders of magnitude from a few times 10^{26} erg s^{-1} to (2–4)$\times10^{30}$ erg s^{-1} (Maggio et al., 1987). Our inferred X-ray luminosity falls near the top end of this range, consistent with a G star near coronal saturation. The five X-ray photons from HD314884 that were detected by Chandra span the soft end of the spectrum from 0.84–1.81 keV. Such soft X-ray detections have been shown to originate in plasma temperatures reaching above T∼10^6 K (Maggio et al., 1990) in the coronal layer of the star due to flaring activity.

We note the calculated luminosity above would be unusually low if the X-ray source were a quiescent accreting NS (see Figure 4 of Reynolds & Miller 2011). Jonker et al. (2007) also point out an exception with 1H 1905+000, which is a LMXB harboring a NS. They inferred an X-ray luminosity limit of 1.7–2.4$\times10^{30}$ erg s^{-1} from 300 ks of Chandra observations. This

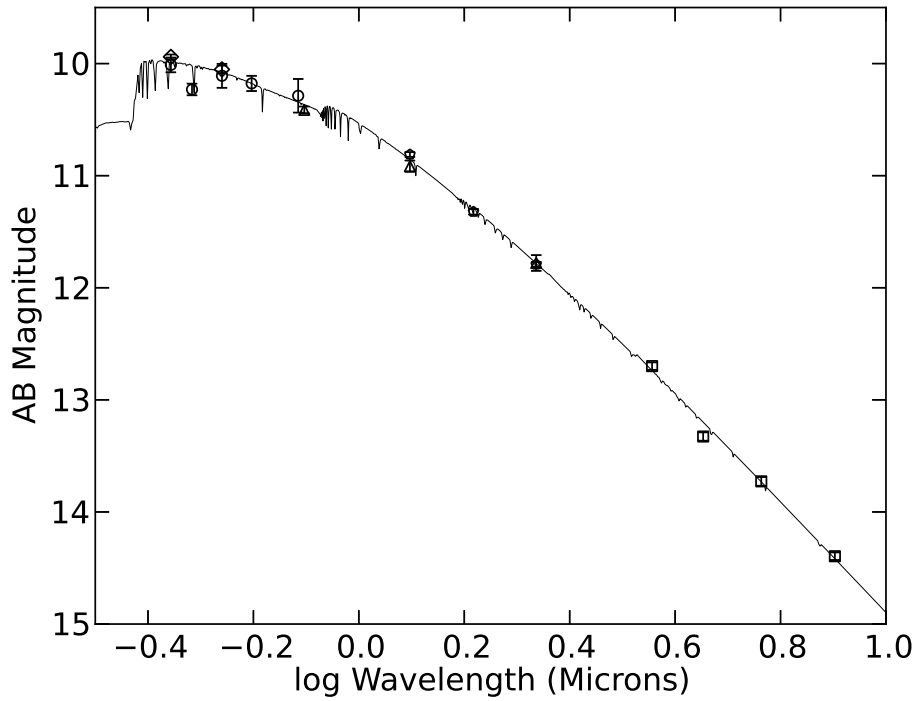

Figure 5.7: The spectral energy distribution for HD314884. The data are drawn from AAVSO Photometric All-Sky Survey DR7 (APASS) (circles), Tycho (diamonds), DeNIS (triangles), 2MASS (pentagons), and the Galactic Legacy Infrared Mid-Plane Survey Extraordinaire (GLIMPSE) (squares). The model is a Kurucz solar metallicity atmosphere with a four way average of $T_{\rm eff}$ = 15,000 K, $\log g$ = 3.5, 4.0 and $T_{\rm eff}$ = 16,000 K, $\log g$ = 3.5, 4.0.

is comparable to the luminosity we infer, so a neutron star companion cannot be ruled out based on the X-ray luminosity. A binary system with a young pulsar cannot be ruled out either since the inferred X-ray luminosity could support the idea as well.

It is unlikely that a BH is the compact object contained in the binary system of CX514 since the maximum mass found in our mass distribution is 2.3 $M_\odot$. Özel et al. (2010c) found that for 16 stellar BHs, the mass distribution peaks at 7.8 $\pm$ 1.2 $M_\odot$. The cutoff mass at the low end is $\geq$ 5 $M_\odot$ (95% confidence), indicating a significant lack of black holes in the $\sim$2–5 $M_\odot$ range. Farr et al. (2011) find that a somewhat lower bound of $\geq$ 4.3 $M_\odot$ with 90% confidence.

Despite the absence of emission lines in the spectra, we cannot fully rule out mass transfer on to an accretion disk. We do want point out that due to the luminosity of the B6 star, emission in the spectra, if present, may be masked. We doppler corrected the spectra and then subtracted them from one another to look for residual emission lines and found none. Also, if mass transfer were present, we would expect much more pronounced ellipsoidal modulations on the spectroscopic period in either of the data sets much like Figure 3 in Ratti et al. (2013).

We estimate the Roche lobe radius, R_{RL}, of the B5V–B6V star from Equation 1.4 to be 4.6–4.8 $R_\odot$ using the mass range 4.1 $M_\odot \leq M_2 \leq$ 4.5 $M_\odot$. The radius of a main sequence B star would be approximately 3.0 $R_\odot$ based on the parameters from the Mamajek compilation list[1], not yet large enough to start accretion on to the G star by Roche lobe overflow.

6. The Classical Nova V603 Aql is Fading

A brief description to CNe was given in Section 1.9 giving the basic picture of the CV subclass. In this section, we focus on the evolutionary aspect of the binary system *after* the nova eruption and mass ejection. The archival data used for this project was compiled by both Bradley Schaefer and myself. Figure 6.1 was reproduced with permission from Johnson et al. (2014a) and much of the text is adapted from the same work.

6.1 CV Evolution Theory

The community accepts a weak but widespread conclusion that any single CV system must somehow transform itself between classes in some type of cyclic manner. Three points of evidence for this idea are as follows: (1) DNe are slowly accumulating material onto the WD, so all of them must eventually become a CN. DNe have a systematically lower accretion rate than CNe, so DNe must have some means to greatly increase their accretion rate so as to turn into these systems. (2) There are greatly too few old novae in the sky to account for the observed nova rate, so old novae must somehow be able to change their appearance, for example by secular decreases in their accretion rate and turning into DNe or perhaps even becoming detached binary systems (Patterson, 1984). (3) Shara et al. (2007) and Shara et al. (2012) have found two dwarf novae that have old nova shells centered on them, proving that at least these two low accretion rate systems were both high accretion rate novae in the past $\sim$1000–10000 years.

The evolution of CVs through nova cycles has become one of the major problems in the field and a variety of models have been proposed. The first was the Hibernation model proposed by Shara et al. (1986) where CNe evolution is driven by the inevitable slight disconnect forced on the binary when the system loses mass during an eruption event. After the

eruption is over, the system evolves toward a low accretion state dictated by the disconnect between the companion and it's Roche lobe, so that the CN will turn into a DN and might even become detached and unrecognizable as an interacting binary system. We can see why mass loss has to impose a separation on the interacting binary system by recalling Equation 1.4:

$$\frac{R_{\rm RL}}{a} = \frac{0.49q^{2/3}}{0.6q^{2/3} + \ln(1+q^{1/3})} \tag{6.1}$$

Here, the ratio $R_{\rm RL}/a$ will increase as the mass ratio q increases. During a CN eruption, M_1 will decrease and M_2 increases leading to an increase in q and, thus, increasing $R_{\rm RL}/a$. Strong support for this claim arises from the observed period increase of the very slow CN BT Mon as a result of the 1939 eruption (Schaefer & Patterson, 1983). After some long time, angular momentum loss in the binary will drive the two stars back together so that it turns into a high accretion rate CV again and the cycle starts over. The Hibernation hypothesis has long been controversial, with few in the community advocating the full model.

The basic mechanism certainly works and so the only question is how deep the hibernation period extends for. A variety of alternative models have been proposed (Naylor 2002; Patterson et al. 2013) and all of these point towards the CV evolving over very long time scales. Vogt (1983) has proposed a cyclic diagram where the CNe and DNe are one and the same stars evolving in the empirical sequence:

$$Classical\ Nova \rightarrow BV\ Pup \rightarrow U\ Gem \rightarrow Z\ Cam \rightarrow UX\ UMa \rightarrow Classical\ Nova$$

With the scenario described above, the CNe will metamorphosize in to DNe (BV Pup, U Gem, Z Cam) before eventually reaching mass accretion rates similar to NLs (UX UMa) and, ultimately, returning back to a CN once enough mass has accreted to ignite a thermonuclear runaway (TNR) on the surface of the WD. The recurrence time, $\tau_{\rm rec}$, of CN eruptions is

thought to last between 10^{3-4} years (Patterson, 1984) for systems to accrete enough material at rates of $\dot{M}_{av} \geq 10^{-8}$ $M_{\odot}$ yr^{-1} (Shara et al., 1986).

The long time scale evolution of CNe has never really been tested. The reason is that the evolution happens on time scales of centuries to millennia and such data is impossible to get. If we look on the time scale of nearly a century, the expected effects may not be large. For example, Hibernation predicts a decline rate that should average to perhaps 1 magnitude per century, although the uncertainties on the rate of fading are substantial (Shara et al. 1986; Kovetz et al. 1988). All pre-1970's magnitudes have systematic errors of up to one magnitude and more (see Figures 3 and 5 of Sandage 2001), so it becomes impossible to test old CNe evolution unless these effects are corrected. Many of the old magnitudes are visual and there are color terms that are required to transform to the modern V magnitude system introducing more systematic errors.

6.2 Acquiring Archival Data

We measured pre-eruption B magnitudes for V603 Aql with the archival plates at the HCO (see Section 2.4). These plates are all in the B magnitude system with an essentially zero color term. The comparison stars that we used all have modern B-band magnitudes, so the derived magnitudes for V603 Aql are almost exactly in the Johnson B magnitude system. With much experience of experimental measures, the one-sigma measurement uncertainty is 0.15 mag on average for these plates. We obtained 50 pre-eruption magnitudes going from 1898 to just 20 days before the nova outburst and present them in Table 6.1. The pre-eruption magnitudes have an RMS scatter of 0.23 mag, which is likely larger than our typical measurement uncertainty due to flickering. The average pre-eruption B magnitude is measured to be 11.43(3) mag.

We have constructed the post-eruption light curve primarily from two sources: the Son-

Table 6.1. Individual magnitudes of V603 Aql

JD	Band	m	Observer
2414515.621	B	11.2	BS, LSU
2415546.786	B	11.2	”
2415552.749	B	11.4	”
2415562.744	B	11.0	”
2415966.783	B	11.3	”
...	...	...	
2452900.593	Vis	11.6	TDB, AAVSO
2452901.325	Vis	11.6	MUY, AAVSO
2452901.684	Vis	11.8	HK, AAVSO
2452902.569	Vis	11.7	BEB, AAVSO
2452907.544	Vis	11.4	BRJ, AAVSO

Note: The full table is available in electronic format only and can be found at: http://vizier.cfa.harvard.edu/viz-bin/VizieR?-source=J/ApJ/780/L25. The 1σ error estimates for each magnitude are described in Section 6.5. The observer column contains the observer's initials followed by affiliation or a reference.

neberg archival plates from 1934 to 2004 for the B-band and the AAVSO light curve from 1934 to 2013 for the V-band. Just as with the HCO plates, the Sonneberg plates all have near-zero color terms. Modern Johnson B magnitudes were used for the comparison stars, so the resultant magnitudes for V603 Aql are all correctly calibrated to the Johnson B magnitude system. We additionally used observations made by the *Association Française des Observateurs d'Ètoiles Variables* (AFOEV) observers, W. H. Steavenson between 1928-1953 (Steavenson 1928, 1934, 1935, 1936, 1938, 1939, 1947, 1948, 1950, 1953). Also, we have V-band observations from Landolt (1968), Landolt (1973), Bruch (1980), Bruch (1991a), Bruch (1991b), Patterson et al. (1997), Sherrington & Jameson (1983), Walker (1957), and Suleimanov et al. (2004), with all of these being on the Johnson V magnitude system. Additional B-band magnitudes taken with CCD cameras appear in the AAVSO database, all of which are very close to the Johnson B magnitude system.

6.3 Transformation of Visual to V Magnitudes

All of our magnitudes from plates and CCDs are already in the Johnson B and V magnitude systems, but all of our visual data is only *close* to the Johnson V magnitudes. Typical differences between V and visual magnitudes amount to about a tenth of a magnitude mainly because V603 Aql is very blue compared to most of its comparison stars. A further problem is that the early comparison star magnitudes are imperfect, with typical errors of a third of a magnitude. This translates into systematic errors for all early observations made with those charts, with chart errors varying with time. Because on these complications, all the visual measures must be transformed carefully to the Johnson V magnitude system.

The transformation from visual magnitudes (m) to V-band magnitudes (V) has been exhaustively measured for many observers as reported in Stanton (1999). They find

$$m = V + 0.21 \times (B - V) \tag{6.2}$$

over a very wide range of $B - V$ colors. The B and V magnitudes for the comparison stars are now well measured, with compilations in APASS. With this, we can recalculate the visual magnitude of each comparison star. V603 Aql has an average color of $B - V$= –0.04 (Bruch & Engel, 1994), which allows us to also transform visual-to-V for the old nova.

Each star in the comparison sequence has a modern B and V magnitude, so we can calculate each visual magnitude, m, using Equation 6.2. Then each star also has a given magnitude recorded on the comparison chart, which we label as μ. Essentially, all visual observations are made with the observer judging the apparent visual magnitude of the target against two nearby comparison stars that bracket the target in brightness and are the closest in brightness to the target. The magnitudes of the slightly brighter comparison star will contain the subscript 'b' and the fainter comparison star will have a subscript 'f'. The

observer makes an estimate as to the fraction, F, of the brightness difference that the target star is from the brighter star, i.e.

$$F = \frac{m - m_b}{m_f - m_b} \tag{6.3}$$

The magnitude *reported* by the observer, μ, will be the observed fraction of the difference between the two comparison stars as calculated from their charted magnitudes, so we also have

$$F = \frac{\mu - \mu_b}{\mu_f - \mu_b} \tag{6.4}$$

We can then equate the two expressions in Equations 6.3 and 6.4 for F and we are left with one equation involving the quantity that we want (m, soon to be converted to V) and known quantities. So our final equation looks like:

$$V = m_b + \frac{(m_f - m_b)(\mu - \mu_b)}{(\mu_f - \mu_b)} - 0.21 \times (B - V). \tag{6.5}$$

The uncertainty in this transformation is small (Stanton, 1999), so the dominant uncertainty in V is simply the usual measurement error which is $\pm$ 0.20 mag. Now we have a full and accurate prescription for transforming from visual to V magnitudes for V603 Aql.

Old magnitudes from the literature almost always report their comparison stars and their adopted magnitudes. For example, Steavenson (1950) magnitudes were made with a sequence reported in Steavenson (1938). For the AAVSO observations, we have gone through the archives at the AAVSO Headquarters to pull out the full set of charts as used by actual observers. The chart used from 1918 until 1986 is that of 184300(d) as based on Harvard photometry. The 1986 chart was used until late 2008, when a new chart (the current chart) was introduced. The modern Johnson B and V magnitudes for all sequence stars come from the APASS photometry (Henden et al., 2012).

6.4 V603 Aql 1918 Eruption

The 1918 nova eruption produced the all-time brightest known nova event, peaking at -0.5 mag. The eruption light curve has been previously published in a variety of places (e.g., Campbell 1919; Payne-Gaposchkin 1964), but none of these follow the nova until it is back to quiescence. Strope et al. (2010) have produced a comprehensive eruption light curve. They classify the light curve as O(12), which is to say that it had oscillations superposed on the usual smooth decline and that the time it took to decline by three magnitudes from the peak (i.e., t_3) was 12 days. V603 Aql has an observed shell of ejected material where the underlying binary has an orbital period of $P_{orb} = 0.1385$ days (3.324 hours) with a highly magnetic WD. Strope et al. (2010) measured that the eruption light curve took 6800 days (i.e., 18.6 years, until 1937) to return to quiescence by means of linear extrapolation of the fitted late light curve to the steady post-eruption level.

6.5 V603 Aql Light Curve

We have collected 22,722 Johnson B, V and visual magnitudes in Table 6.1. We have 50 pre-eruption B magnitudes from HCO (1898-1918), 539 post-eruption B magnitudes from Sonneberg (1928–2004), 15 B magnitudes from the AAVSO (2010–2012), 2 B magnitudes from AFOEV (2012), 18,980 visual magnitudes from the AAVSO (1934–2013), 61 visual magnitudes from Steavenson (1928–1953) and 3,075 V magnitudes from the sources listed in Section 6.2. For most magnitudes, the individual error bars were not measured, so we have used typical values of $\pm$ 0.15 for the HCO and Sonneberg plates, $\pm$ 0.20 for visual observers, and $\pm$ 0.02 for CCD measures.

The error bars for non-CCD magnitudes are irrelevant because the ordinary flickering on all time scales of V603 Aql is always larger. That is, the $\pm$ 0.20 mag uncertainty from visual observers contributes only a fraction of extra variance to our light curve because a much

larger variance arises from flickering in the star. The 0.15–0.20 mag measurement errors for single observations is also irrelevant because we always have a large number of observations (N), so the measurement error is $0.20/\sqrt{N}$ and is always small.

With the ubiquitous flickering of V603 Aql, our light curve shows the usual scatter of points, with the true behavior partly hidden by all the scatter. To better show the long-term behavior, we have binned our light curve into yearly averages for each calendar year from 1934. With the large number of points per year, we can directly determine the measurement error bar of the average as the larger of RMS/$\sqrt{N}$ or $0.15/\sqrt{N}$, where N is the number of included observations and RMS is the *root mean square* of their scatter. For bins with hundreds of magnitudes, this leads to unrealistically small error bars because the measurement errors will be dominated by systematic errors. We have placed a lower limit on the error bars of 0.02 mag. The resultant yearly-binned B and V-band average magnitudes are tabulated in Table 6.2 and the light curve is displayed in Figure 6.1.

6.6 Observational Evidence Confirming V603 Aql is Fading

The Hibernation model predicts that old novae will be fading at roughly the rate of one magnitude per century. Other models (e.g., Patterson et al. 2013) also predict fading long after the eruption is completely over and all the eruption-related transients have completely died down. The whole purpose of this particular study of V603 Aql was to test these models of CN evolution. An initial glance at Figure 6.1 shows that V603 Aql is fading, and the rate is roughly half a magnitude per century.

The steeper decline in V before 1938 is likely just the tail end of the eruption. To avoid confusing the end of the eruption with any fading due to evolution, we must only look for a trend after the eruption is over. Strope et al. (2010) fitted the fading tail and found that it reached quiescence in early 1937 (i.e., 6800 days after peak). A second convincing means

Table 6.2. Yearly-binned B and V magnitudes after correcting visual magnitudes in Table 6.1 as described in Section 6.3

<Year>	$<m_B>$	$\sigma_{B,\mathrm{meas}}$	$<m_V>$	$\sigma_{V,\mathrm{meas}}$
1934.5	11.43	0.03	11.11	0.02
1935.5	11.36	0.02	11.16	0.02
1936.5	11.32	0.09	11.24	0.02
1937.5	11.20	0.03	11.29	0.03
1938.5	11.51	0.05	11.31	0.02
1939.5	11.54	0.03	11.20	0.03
...	...	...	...	...

Note: The full table is available in electronic format only and is available at: http://vizier.cfa.harvard.edu/viz-bin/VizieR?-source=J/ApJ/780/L25.

to determine the end of the eruption is to see when the nova has faded to the pre-eruption level $B = 11.43(3)$, which is certainly true by 1938. Thus, we confidently take 1938 to be the year by which the eruption is completely over.

After 1938, there are some fluctuations in this otherwise steady decline. The correlation between the variations in the B and V light curves is vague and unconvincing. From 1975 to 1981, both colors show a decline compared to the best fit linear trend, but the B-band light curve immediately brightens from 1981 to 1990 while the V-band light curve holds constant over the same interval. Neither the structure in the V-band light curve from the 1960's, nor the outlier 1964 B magnitude are shown in the other color. V603 Aql has never been seen to change its color significantly (Bruch & Engel 1994) or systematically in any substantial manner, so the deviations between the B and V light curves are likely caused by some sort of unrecognized systematic error. This alerts us, not surprisingly, that our light curve still has systematic variations at the 0.1 mag level. Fortunately, such problems are small compared to the observed fitted decline of $\sim$0.4 mag over 76 years.

Another way to get an idea as to systematic errors is to compare the AAVSO V-band

light curve with the non-AAVSO V-band light curve. These are two completely independent measures of the same function, so significant variations can only be ascribed to unknown systematic problems. A direct comparison is problematic because the non-AAVSO light curve has many gaps. Nevertheless, a simple fitting of the best line through χ^2 minimization returns identical intercepts and slopes of 0.48(8) and 0.58(18) mag per century for the AAVSO and non-AAVSO binned light curves respectively from 1938-2002. The comparison light curve can be seen in Figure 6.2. This comparison suggests that systematic problems in the derived slope of the light curve are negligibly small.

Whether through intrinsic variations in V603 Aql or due to small residual systematic errors in measuring the light curve, we realize that the 1938-2013 light curve will show deviations from a straight line. Such deviations will result in a chi-square fit of the light curve to a simple line that has a large reduced chi-square. A more realistic analysis will allow for some (presumed constant) variations (with RMS scatter of $\sigma_{\rm sys}$) superposed on a steady linear decline. In essence, we have the total one-sigma variations in the yearly-binned magnitudes equal to $\sqrt{\sigma_{\rm meas}^2 + \sigma_{\rm sys}^2}$. If we set $\sigma_{\rm sys}$ such that the reduced chi-square of the fit is near unity, then we will get realistic error bars in the slope. With this, we set $\sigma_{\rm sys} = 0.10$.

The 1938-2013 B and V yearly-binned light curves for V603 Aql in Figure 6.1 have fitted slopes of 0.30(8) and 0.50(5) mag per century respectively. These two slopes are different at the two-sigma level, and we judge them to be the same to within the error bars. (Such differences are easily caused by, for example, the lack of B-band magnitudes from 2005–2009, such that their inclusion would apparently bring the slopes into much closer agreement.) The existence of similar slopes in completely independent light curves gives us good confidence that V603 Aql is fading. With V603 Aql observed to be essentially constant in color (Bruch & Engel 1994), the best measure of the slope is from some combination of the measures in the two colors. The weighted average of the two slopes is 0.44(4) mag/century.

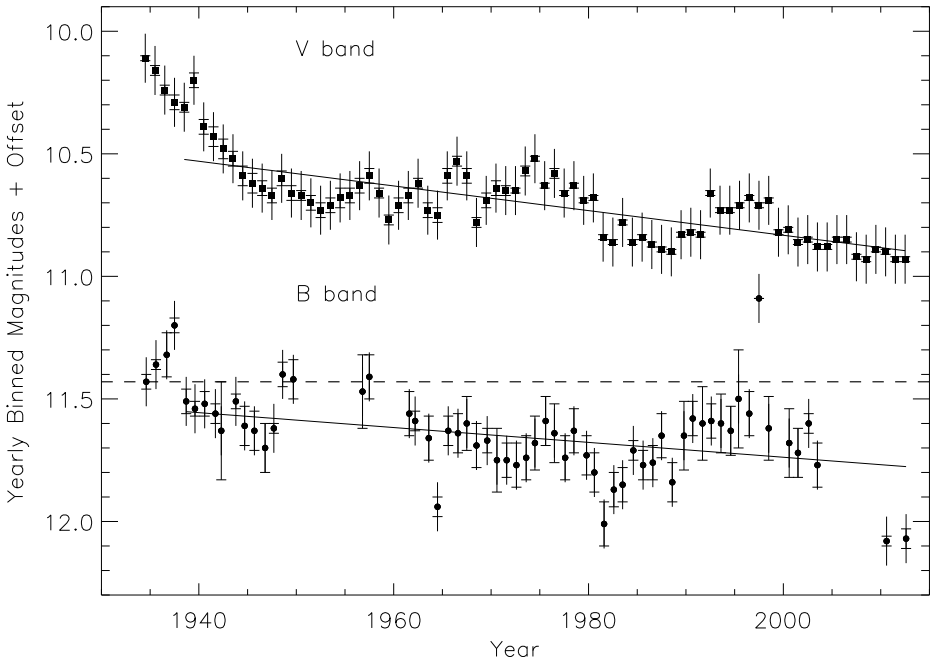

Figure 6.1: Yearly-binned light curve for V603 Aql. The bottom curve is the B-band yearly-averaged magnitudes from 1934-2013 and is taken primarily from Sonneberg archival plates. The top curve is for the V-band with an offset upwards of 1.0 mag, taken primarily from the visual magnitudes reported to the AAVSO. The visual magnitudes have been correctly transformed into Johnson V-band measures. Each yearly average has its measurement uncertainty represented by the inner error bars with serifs, while the total uncertainty, including the estimated systematic uncertainty, is represented by the outer error bars. The *pre*-eruption level is at $B = 11.43(3)$ mag (and so $V = 11.47(3)$), as represented by the horizontal dashed line, so the eruption is certainly over by 1938. The point of this figure is that both B and V light curves show V603 Aql to be significantly declining from 1938-2013.

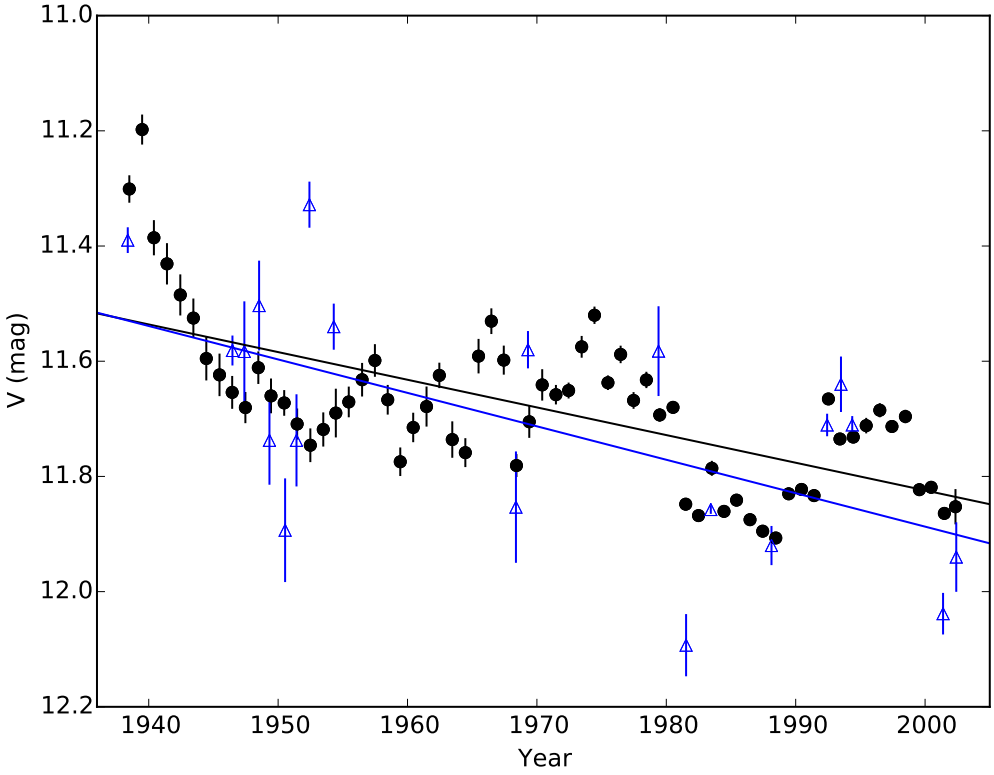

Figure 6.2: Comparison light curve of V603 Aql using yearly binned AAVSO V data (black circles) and non-AAVSO V data (blue triangles) with best fit lines fitting each of the data sets.

7. Conclusions

The total number of detected GBS X-ray sources closely resembles those predicted by population synthesis models from Jonker et al. (2011), although these models are not always perfect. The same models also predict that ∼128 sources in the DECam data set (424 total sources) should not have an optical counterpart but should be bright enough to be detectable in X-ray. I found only 29 sources without any visible star inside the X-ray error circle using the r' filter with a limiting magnitude of $r' = 23$. Of the 424 sources, 142 contain visible counterparts that are non-variable. Some of the source percentages are very close to the source percentages found in Britt et al. (2014) where they analysed the first 1216 sources of the GBS survey. Table 7.1 shows the comparison of percentages for each source category from Britt et al. (2014) and those found in this work. One thing to note is the percentage of saturated sources. The low number in this work is based on the fact that we followed our 2×90 sec exposures with 2×1 sec exposures insuring that we were sensitive enough to brighter stars in our FoV > 11.4 in the r'. Britt et al. (2014) only used 120 sec exposures resulting in a sensitivity > 16 in the r' band before saturation. The percentages of ellipsoidal, long period variables, and flaring events are all approximately the same between the two surveys. Their (Britt et al. 2014) percentage of variables, non-variables, and no counterparts is roughly double that which I found. This may be attributed to the baseline for observations (their 8 days compared to my 2 days). For instance, a pulsating variable in a binary or an eclipsing variable could have periods from 1–70 days and the chance at detection is larger in a longer baseline observational survey. The shorter baseline in this work ensures higher time resolution and the idea that we are more sensitive to short period systems (which we are more interested in). The histogram of sources with confirmed periods is shown in Figure

Table 7.1: Comparison of percentages for sources in Britt et al. (2014) and this work

	Britt et al. (2014)	This work
V	20	56
NV	67	33
NC	13	7
S	29	4
Flick	46	76
Ell	3	2
Ec	16	3
LPV	10	9
Flare	6	5
Per	23	5

Note: The numbers in this table represent percentages where Britt et al. (2014) analysed a total of 1216 sources compared to the 424 sources in this work. The naming scheme in column 1 is the same as that used in Section 3.4. In Britt et al. (2014) they use "sinusoidal" whereas I use "Per".

7.1. The highest concentration of sources are found with periods less than 1 day and peaking around a period of 0.3 days.

With a higher time resolution, we would expect to have less flickering sources that should have resolved, short periods. One specific example is CX44 which was first classified as a flickering source in Britt et al. (2014). When I analysed the DECam data for CX44 I found a 0.66 day ellipsoidal modulation (See Figure 2.2). As a check to see if crowding and nearby starlight entering the aperture was an issue, I visually checked several flickering sources and their reference images. The result was that they appeared to be genuine flickering sources without any apparent problems.

RS CVns and W UMas are much more common than LMXBs. Jonker et al. (2014) predicted ∼221 RS CVns and ∼59 W UMas in the area covered by DECam which should be detectable in both X-ray and optical. For a sample of 424 sources, this equates to 280 sources or ∼66% of the DECam sample. I have confirmed that 6 W Umas and 4 RS CVns exist in the DECam sample based on light curve morphology and $\frac{F_{\rm x}}{F_{\rm opt}}$ (see Section 3.5). This

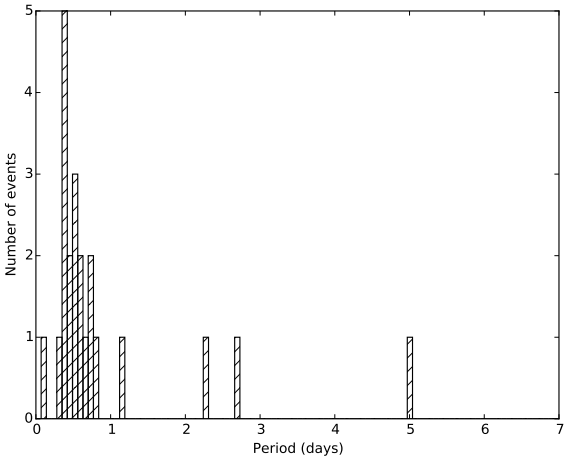

Figure 7.1: Histogram of the confirmed periods in the DECam data set.

leaves another 18 LPVs with periods that appear to be > 2 days. Assuming that all 18 are RS CVns and if we assume that all 15 saturated sources are a mixture of the two types, then this brings us to a total of 43 sources which is well below that which is predicted from the population synthesis models. The light curve morphology of RS CVns and W UMas are very distinct with periods of <1 day to several days and showing an amplitude of (approximately) $\Delta r' > 0.1$ magnitude. With a sampling frequency of approximately every 2–14 minutes, we would expect to see all of the RS CVns and W UMas in the survey. A small amplitude, long-period RS CVn could be missed, especially at low inclination, and we could argue this for all the missing RS CVns. The missing W UMas are problematic since these are not too faint as to be missed, not too bright as to be saturated, and not too long of periods.

I have confirmed 3 CVs and another 7 more can be classified as either a CV or a qLMXB. CVs (and IPs) and qLMXBs are expected to show aperiodic flickering (although CX19 is an eclipsing IP exception). I have found another 170 sources that show aperiodic flickering without a large outburst or periodicity. So if all of these flickering sources are attributed to disk light from CVs, then this would potentially bring the total to 180. Jonker et al. (2011)

predicts that there should be ∼23 CVs and ∼56 IPs in the area covered by DECam for a total of 79. This is dramatically lower than the total number of flickering sources and so some of them must be attributed to other X-ray emitting sources. Whether these are the missing qLMXBs that are predicted to exist is still not known. Some qLMXBs must be flickering without a recoverable period. These 101 flickering sources could possibly be the missing qLMXBs where ∼45 were predicted in the population synthesis models by Jonker et al. (2011). Among the qLMXB candidates in the survey, CXB82 shows G9 spectral features along with Hα emission after subtracting the best-fit stellar template (Wu et al., 2015) and CXB99 shows a K2V type star with narrow Hα emission.

This survey complements the work done by Britt et al. (2014) and completes the photometric analysis (and in some cases spectroscopic analysis, e.g. Torres et al. 2014, Wu et al. 2015) of the original 1640 unique X-rays sources found in the GBS (Jonker et al., 2014). The conclusions in Britt et al. (2014) are similar to the findings during the analysis of the 424 DECam sources. Mainly, where are the qLMXBs in the GBS and are they really "missing"? The estimate in Jonker et al. (2011) predicts that there should be ∼45 detectable qLMXBs in both the X-ray and the optical in the DECam area. I briefly describe the possibilities laid out in Britt et al. (2014) and elaborate on them.

First, it is entirely possible that the estimate of sources in Jonker et al. (2011) has been drastically overestimated due to the uncertain X-ray luminosity of qLMXBs. If the quiescent NS LMXBs that have not gone in to outburst are much fainter in X-ray than those that have been *followed* in to quiescence after an outburst, then they might not be readily detectable in the X-ray due to the limits of Chandra. Recently, van Haaften et al. (2015) have shown that there should be a population of $\sim 2.1 \times 10^3$ LMXBs with NS accretors where 15-40 are expected to be persistent at a $L_X = 10^{35}$ ergs cm^{-2} s^{-1} which lends credence to the previous predictions made by Jonker et al. (2011).

Second, the optical counterparts to qLMXBs might be too faint to be detectable even

with a limiting magnitude of $r' = 23$ on a 4.0 meter telescope. The flickering or variability may not be noticeable because the photometric errors are comparable to the amplitude of variability. Some of the sources in this sample have milli-mag errors with hundredths of a mag variations and were easily detected as variable based on their RMS scatter, i. e. CXB82 or CXB149.

Third, the degree of variability of qLMXBs is not understood and they could be intrinsically non-variable, showing no flickering or ellipsoidal modulations in their optical light curves. The spectroscopic analysis of a handful of sources by Torres et al. (2014) and Wu et al. (2015) have revealed potential accreting binary systems along with a candidate BH qLMXB (CX561) which shows no variability (Britt et al., 2014). The potential accreting sources may be different from those found in outburst though where the narrow emission lines may originate in chromospherically active stars.

Fourth, qLMXBs may flicker *too* much to recover their underlying periodic nature. The DECam GBS survey has approximately 101 flickering sources that do not have a secure classification that could potentially be qLMXBs. Britt et al. (2014) found that the number of flickering sources in their Mosaic-II survey was not enough to account for both the expected population of IPs and the population of qLMXBs.

Lastly, the missing qLMXBs are not missing, they are just not there. Maybe there is not a large population of Galactic qLMXBs. The initial population estimate of Jonker et al. (2011) assumed a spatial distribution of qLMXBs that followed the distribution of stars in our Galaxy. The Blaauw kicks imparted to systems and asymmetry in SNe explosions can increase the random distribution of qLMXBs both above and below the Galactic Plane. We know that $\sim$20% of BH transients are found 1 kpc $< z <$ 1.5 kpc above or below the Galactic Plane (Jonker & Nelemans, 2004). Whether qLMXBs follow the same spatial distribution is unclear.

One other possibility is that the qLMXB population is masked as non-eclipsing CVs

where only flickering from the accretion disk is present. Both of these types of systems have very similar observational properties from their period range to donor star spectral features (when present) to $\frac{F_{\rm x}}{F_{\rm opt}}$ to light curve morphology. In the case of qLMXBs with NS primaries, even the mass range can overlap with the heavier WD primaries in CVs. For example, the WD mass distribution tapers off towards $\sim$1.2 $M_{\odot}$ (Wijnen et al., 2015) which overlaps with NS mass distribution of 1.1–2.0 $M_{\odot}$ (Özel & Freire, 2016). Distinguishing between CVs and qLMXBs ultimately comes down to gathering enough time-series spectroscopy to cover a full orbital period. From the semi-amplitude of the radial velocity curve we can then place constraints on the mass function (assuming we have some information about the inclination angle). Ratti et al. (2013) showed that CX93 is a long period CV using the same technique mentioned above to distinguish it from a qLMXB where it showed many of the same properties before a spectroscopic followup was completed.

In some cases, even the spectroscopy is not completely reliable in confirming accreting binaries based on disk emission features. Wu et al. (2015) has shown that there possibly exists an entire population of hidden accreting binaries (HABs) once their spectrum is optimally subtracted from a template spectrum. It appears as though in several cases the absorption features from the donor star may partially fill in the emission line cores making these systems look like normal single stars. One case in particular that confirms the presence of HABs in the DECam GBS sample is CXB26. In Section 3.6.3, I showed that CXB26 is indeed a HAB with a DN outburst of $\sim$1 magnitude and $\frac{F_{\rm x}}{F_{\rm opt}}$ appropriate for CVs. This discovery proves that HABs are out there and could be harboring not only CVs, but possibly the qLMXB population.

I have shown that multi-wavelength, multi-epoch observational campaigns can help to characterize different stellar systems based on the morphology of light curves, spectral features, and X-ray signatures. Placing limits on the system parameters such as effective temperature, dynamical masses, inclination angle, distance, orbital/spin period or a com-

bination of all parameters leads to better knowledge of the system and understanding its present stage of evolution.

I have examined the optical variability of X-ray sources in the GBS using DECam on timescales of less than two days. My collaborators and I have identified 237 variable counterparts which includes 38 periodic or long period variables, 179 flickering sources, and 7 eclipsing sources. The flickering sources are a mixture of CVs, IPs, and, possibly, a population of hidden accreting binaries (qLMXBs?). We have several unconfirmed CV or qLMXB candidates based on light curve morphology, spectral features, and $\frac{F_{\rm X}}{F_{\rm opt}}$ (CXB: 48, 64, 77, 82, 99, 137, 149).

Optical variability is very powerful in distinguishing between systems, but a full spectroscopic followup on each source would be ideal. I have shown that an in-depth study of CX19 has revealed the first X-ray selected, deeply-eclipsing IP with X-ray eclipses. On the other hand, an in-depth study of CX514 has revealed a SPB star with a 0.8 $M_{\odot}$ companion which is most likely an active G-type star or WD. CX514 has at least 3 distinct photometric frequencies attributed to non-radial pulsation modes that are different from the orbital period of the system.

Through the use of photographic plates and archival magnitudes, we have shown that the old nova V603 Aql is fading at a rate of 0.44(4) mag/century. Our calculated fading rate further supports the idea of a fading model (much like the Hibernation model of Shara et al. 1986) long after a nova eruption. The Hibernation model predicts that CNe could continue fade into quiescent states between eruptions and possibly "change" in to detached binaries over time if significant mass is lost during eruptions. These quiescent systems are not unlike those possibly hiding in the GBS, mainly qLMXBs, W UMas, and even HABs.

References

Aerts, C., De Cat, P., Peeters, E., et al. 1999, A&A, 343, 872

Alard, C., & Lupton, R. H. 1998, ApJ, 503, 325

Alcock, C., Allsman, R. A., Axelrod, T. S., et al. 1996, ApJ, 461, 84

Allan, A., Hellier, C., & Ramseyer, T. F. 1996, MNRAS, 282, 699

Allen, C. W. 1973, Astrophysical quantities

Angelini, L., & Verbunt, F. 1989, MNRAS, 238, 697

Antoniadis, J., Freire, P. C. C., Wex, N., et al. 2013, Science, 340, 448

Aungwerojwit, A., Gänsicke, B. T., Wheatley, P. J., et al. 2012, ApJ, 758, 79

Benjamin, R. A., Churchwell, E., Babler, B. L., et al. 2003, PASP, 115, 953

Berghoefer, T. W., Schmitt, J. H. M. M., Danner, R., & Cassinelli, J. P. 1997, A&A, 322, 167

Bernardini, F., Russell, D. M., Koljonen, K. I. I., et al. 2016, ArXiv e-prints, arXiv:1604.08022

Beuermann, K., Harrison, T. E., McArthur, B. E., Benedict, G. F., & Gänsicke, B. T. 2004, A&A, 419, 291

Binney, J., & Merrifield, M. 1998, Galactic Astronomy

Blaauw, A. 1961, BAN, 15, 265

Bohlin, R. C., Savage, B. D., & Drake, J. F. 1978, ApJ, 224, 132

Britt, C. T., Hynes, R. I., Johnson, C. B., et al. 2014, ApJS, 214, 10

Bruch, A. 1980, Information Bulletin on Variable Stars, 1805

—. 1991a, Information Bulletin on Variable Stars, 3567

—. 1991b, AcA, 41, 101

Bruch, A., & Engel, A. 1994, A&AS, 104

Campbell, L. 1919, Harvard College Observatory Circular, 220, 1

Cardelli, J. A., Clayton, G. C., & Mathis, J. S. 1989, ApJ, 345, 245

Casares, J., Charles, P. A., Jones, D. H. P., Rutten, R. G. M., & Callanan, P. J. 1991, MNRAS, 250, 712

Casares, J., Charles, P. A., & Naylor, T. 1992, Nature, 355, 614

Cassinelli, J. P., & Olson, G. L. 1979, ApJ, 229, 304

Castelli, F., & Kurucz, R. L. 2003, in IAU Symposium, Vol. 210, Modelling of Stellar Atmospheres, ed. N. Piskunov, W. W. Weiss, & D. F. Gray, A20

Cieslinski, D., Diaz, M. P., Drake, A. J., & Cook, K. H. 2004, PASP, 116, 610

Clark, G. W. 1975, ApJL, 199, L143

De Cat, P., Aerts, C., De Ridder, J., et al. 2000, A&A, 355, 1015

de Martino, D., Bonnet-Bidaud, J.-M., Mouchet, M., et al. 2006, A&A, 449, 1151

Demorest, P. B., Pennucci, T., Ransom, S. M., Roberts, M. S. E., & Hessels, J. W. T. 2010, Nature, 467, 1081

Dempsey, R. C., Linsky, J. L., Fleming, T. A., & Schmitt, J. H. M. M. 1997, ApJ, 478, 358

DENIS Consortium. 2005, VizieR Online Data Catalog, 2263

Dhillon, V. S. 1996, in Astrophysics and Space Science Library, Vol. 208, IAU Colloq. 158: Cataclysmic Variables and Related Objects, ed. A. Evans & J. H. Wood, 3

Draine, B. T. 2003, ApJ, 598, 1017

Dziembowski, W. A., Moskalik, P., & Pamyatnykh, A. A. 1993, MNRAS, 265, 588

Echevarria, J. 1988, MNRAS, 233, 513

Eggleton, P. P. 1983, ApJ, 268, 368

Evans, I. N., Primini, F. A., Glotfelty, K. J., et al. 2010, ApJS, 189, 37

Farr, W. 2012, in X-ray Binaries. Celebrating 50 Years Since the Discovery of Sco X-1

Farr, W. M., Sravan, N., Cantrell, A., et al. 2011, ApJ, 741, 103

Frank, J., King, A., & Raine, D. J. 2002, Accretion Power in Astrophysics: Third Edition

Garmire, G. P. 1997, in Bulletin of the American Astronomical Society, Vol. 29, American Astronomical Society Meeting Abstracts #190, 823

Gehrels, N. 1986, ApJ, 303, 336

Gonzalez, O. A., Rejkuba, M., Zoccali, M., Valenti, E., & Minniti, D. 2011, A&A, 534, A3

Gonzalez, O. A., Rejkuba, M., Zoccali, M., et al. 2012, A&A, 543, A13

Gray, R. O., & Corbally, J., C. 2009, Stellar Spectral Classification

Grimm, H.-J., Gilfanov, M., & Sunyaev, R. 2003, MNRAS, 339, 793

Grindlay, J. E. 1999, in Astronomical Society of the Pacific Conference Series, Vol. 157, Annapolis Workshop on Magnetic Cataclysmic Variables, ed. C. Hellier & K. Mukai, 377

Grindlay, J. E. 2006, Advances in Space Research, 38, 2923

Grindlay, J. E., Hong, J., Van den Berg, M., Servillat, M., & Zhao, P. 2010, in Bulletin of the American Astronomical Society, Vol. 42, AAS/High Energy Astrophysics Division #11, 735

Grindlay, J. E., Hong, J., Zhao, P., et al. 2005, ApJ, 635, 920

Güdel, M. 2004, A&ARv, 12, 71

Gunn, J. E., Carr, M., Rockosi, C., et al. 1998, AJ, 116, 3040

Hambleton, K., Kurtz, D., Prša, A., Bloemen, S., & Southworth, J. 2012, in IAU Symposium, Vol. 282, From Interacting Binaries to Exoplanets: Essential Modeling Tools, ed. M. T. Richards & I. Hubeny, 77–78

Hands, A. D. P., Warwick, R. S., Watson, M. G., & Helfand, D. J. 2004, MNRAS, 351, 31

Harlaftis, E. T., & Horne, K. 1999, MNRAS, 305, 437

Heinke, C. O. 2010, in American Institute of Physics Conference Series, Vol. 1314, American Institute of Physics Conference Series, ed. V. Kalogera & M. van der Sluys, 135–142

Hellier, C. 1997, MNRAS, 291, 71

Hellier, C., Mason, K. O., Rosen, S. R., & Cordova, F. A. 1987, MNRAS, 228, 463

Henden, A. A., Levine, S. E., Terrell, D., Smith, T. C., & Welch, D. 2012, Journal of the American Association of Variable Star Observers (JAAVSO), 40, 430

Henden, A. A., Welch, D. L., Terrell, D., & Levine, S. E. 2009, in American Astronomical Society Meeting Abstracts, Vol. 214, American Astronomical Society Meeting Abstracts #214, 669

Hog, E., Kuzmin, A., Bastian, U., et al. 1998, A&A, 335, L65

Hong, J., van den Berg, M., Grindlay, J. E., Servillat, M., & Zhao, P. 2012, ApJ, 746, 165

Hong, J., van den Berg, M., Schlegel, E. M., et al. 2005, ApJ, 635, 907

Hynes, R. I., & Britt, C. T. 2012, ApJ, 755, 66

Hynes, R. I., Robinson, E. L., & Jeffery, E. 2004, ApJL, 608, L101

Hynes, R. I., Wright, N. J., Maccarone, T. J., et al. 2012, ApJ, 761, 162

Ivanova, N., Belczynski, K., Fregeau, J. M., & Rasio, F. A. 2005, MNRAS, 358, 572

Ivanova, N., & Taam, R. E. 2003, ApJ, 599, 516

Johnson, C. B., Schaefer, B. E., Kroll, P., & Henden, A. A. 2014a, ApJL, 780, L25

Johnson, C. B., Hynes, R. I., Maccarone, T., et al. 2014b, MNRAS, 444, 1584

Johnstone, C. P., Gregory, S. G., Jardine, M. M., & Getman, K. V. 2012, MNRAS, 419, 29

Jonker, P. G., & Nelemans, G. 2004, MNRAS, 354, 355

Jonker, P. G., Steeghs, D., Chakrabarty, D., & Juett, A. M. 2007, ApJL, 665, L147

Jonker, P. G., Bassa, C. G., Nelemans, G., et al. 2011, ApJS, 194, 18

Jonker, P. G., Torres, M. A. P., Hynes, R. I., et al. 2014, ApJS, 210, 18

Kallrath, J., & Milone, E. F. 2009, Eclipsing Binary Stars: Modeling and Analysis, doi:10.1007/978-1-4419-0699-1

Kalogera, V. 1999, ApJ, 521, 723

Kovetz, A., Prialnik, D., & Shara, M. M. 1988, ApJ, 325, 828

Krivonos, R., Tsygankov, S., Lutovinov, A., et al. 2012, A&A, 545, A27

Kupfer, T., Groot, P. J., Levitan, D., et al. 2013, MNRAS, 432, 2048

Landolt, A. U. 1968, PASP, 80, 481

—. 1973, Information Bulletin on Variable Stars, 822

Lasota, J.-P. 2001, NewAR, 45, 449

Lattimer, J. M., & Prakash, M. 2001, ApJ, 550, 426

—. 2007, PhR, 442, 109

Liedahl, D. A., Osterheld, A. L., & Goldstein, W. H. 1995, ApJL, 438, L115

Lin, D., Webb, N. A., & Barret, D. 2012, ApJ, 756, 27

Lupton, R., Gunn, J. E., Ivezić, Z., Knapp, G. R., & Kent, S. 2001, in Astronomical Society of the Pacific Conference Series, Vol. 238, Astronomical Data Analysis Software and Systems X, ed. F. R. Harnden, Jr., F. A. Primini, & H. E. Payne, 269

Maggio, A., Sciortino, S., Vaiana, G. S., et al. 1987, ApJ, 315, 687

Maggio, A., Vaiana, G. S., Haisch, B. M., et al. 1990, ApJ, 348, 253

Marsh, T. R., Robinson, E. L., & Wood, J. H. 1994, MNRAS, 266, 137

Mauerhan, J. C., Muno, M. P., Morris, M. R., et al. 2009, ApJ, 703, 30

Menou, K., Esin, A. A., Narayan, R., et al. 1999, ApJ, 520, 276

Munari, U., Sordo, R., Castelli, F., & Zwitter, T. 2005, A&A, 442, 1127

Muno, M. P., Baganoff, F. K., Bautz, M. W., et al. 2003, ApJ, 599, 465

Narayan, R., & McClintock, J. E. 2005, ApJ, 623, 1017

Naylor, T. 2002, in American Institute of Physics Conference Series, Vol. 637, Classical Nova Explosions, ed. M. Hernanz & J. José, 16–20

Nelemans, G. 2005, in Astronomical Society of the Pacific Conference Series, Vol. 330, The Astrophysics of Cataclysmic Variables and Related Objects, ed. J.-M. Hameury & J.-P. Lasota, 27

Nelemans, G., & Jonker, P. G. 2010, NewAR, 54, 87

Nelemans, G., Jonker, P. G., & Steeghs, D. 2006, MNRAS, 370, 255

Nesterov, V. V., Kuzmin, A. V., Ashimbaeva, N. T., et al. 1995, A&AS, 110

Niels Bohr Institute, U. o. C., Institute of Astronomy, UK, C., & Real Instituto y Observatorio de La Armada en San Fernando. 2014, VizieR Online Data Catalog, 1327

Norton, A. J., & Watson, M. G. 1989, MNRAS, 237, 853

Norton, A. J., Wynn, G. A., & Somerscales, R. V. 2004, ApJ, 614, 349

Nowak, M. A., Heinz, S., & Begelman, M. C. 2002, ApJ, 573, 778

Nowak, M. A., Wilms, J., Heindl, W. A., et al. 2001, MNRAS, 320, 316

Orosz, J. A., & Bailyn, C. D. 1997, ApJ, 477, 876

Orosz, J. A., Jain, R. K., Bailyn, C. D., McClintock, J. E., & Remillard, R. A. 1998, ApJ, 499, 375

Orosz, J. A., McClintock, J. E., Narayan, R., et al. 2007, Nature, 449, 872

Özel, F., Baym, G., & Güver, T. 2010a, Phys. Rev. D, 82, 101301

Özel, F., & Freire, P. 2016, ArXiv e-prints, arXiv:1603.02698

Özel, F., Güver, T., & Psaltis, D. 2009, ApJ, 693, 1775

Özel, F., Psaltis, D., Narayan, R., & McClintock, J. E. 2010b, ApJ, 725, 1918

—. 2010c, ApJ, 725, 1918

Paczyński, B. 1971, ARA&A, 9, 183

Paczyński, B. 1976, in IAU Symposium, Vol. 73, Structure and Evolution of Close Binary Systems, ed. P. Eggleton, S. Mitton, & J. Whelan, 75

Patterson, J. 1984, ApJS, 54, 443

—. 1994, PASP, 106, 209

Patterson, J., Kemp, J., Saad, J., et al. 1997, PASP, 109, 468

Patterson, J., Uthas, H., Kemp, J., et al. 2013, MNRAS, 434, 1902

Payne-Gaposchkin, C. 1964, The galactic novae

Pfahl, E., Rappaport, S., & Podsiadlowski, P. 2003, ApJ, 597, 1036

Plotkin, R. M., Gallo, E., & Jonker, P. G. 2013, ArXiv e-prints, arXiv:1306.1570

Pojmanski, G. 1997, AcA, 47, 467

—. 2002, AcA, 52, 397

Poznanski, D., Prochaska, J. X., & Bloom, J. S. 2012, MNRAS, 426, 1465

Predehl, P., & Schmitt, J. H. M. M. 1995, A&A, 293, 889

Pretorius, M. L., & Mukai, K. 2014, MNRAS, 442, 2580

Ratti, E. M., van Grunsven, T. F. J., Jonker, P. G., et al. 2013, MNRAS, 428, 3543

Remillard, R. A., & McClintock, J. E. 2006, ARA&A, 44, 49

Revnivtsev, M., Sazonov, S., Gilfanov, M., Churazov, E., & Sunyaev, R. 2006, A&A, 452, 169

Reynolds, M. T., & Miller, J. M. 2011, ApJL, 734, L17

Ritter, H., Zhang, Z.-Y., & Kolb, U. 2000, A&A, 360, 959

Rosner, R., Golub, L., & Vaiana, G. S. 1985, ARA&A, 23, 413

Saesen, S., Briquet, M., Aerts, C., Miglio, A., & Carrier, F. 2013, AJ, 146, 102

Sandage, A. 2001, PASP, 113, 267

Scaringi, S., Bird, A. J., Norton, A. J., et al. 2010, MNRAS, 401, 2207

Schaefer, B. E., & Patterson, J. 1983, ApJ, 268, 710

Schlegel, D. J., Finkbeiner, D. P., & Davis, M. 1998, ApJ, 500, 525

Schmitt, J. H. M. M., Fleming, T. A., & Giampapa, M. S. 1995, ApJ, 450, 392

Shara, M. M. 1989, PASP, 101, 5

Shara, M. M., Hinkley, S., Zurek, D. R., Knigge, C., & Dieball, A. 2005, AJ, 130, 1829

Shara, M. M., Livio, M., Moffat, A. F. J., & Orio, M. 1986, ApJ, 311, 163

Shara, M. M., Mizusawa, T., Wehinger, P., et al. 2012, ApJ, 758, 121

Shara, M. M., Martin, C. D., Seibert, M., et al. 2007, Nature, 446, 159

Sherrington, M. R., & Jameson, R. F. 1983, MNRAS, 205, 265

Silber, A. D. 1992, PhD thesis, Massachusetts Institute of Technology.

Skrutskie, M. F., Cutri, R. M., Stiening, R., et al. 2006, AJ, 131, 1163

Stanton, R. H. 1999, Journal of the American Association of Variable Star Observers (JAAVSO), 27, 97

Steavenson, W. H. 1928, MNRAS, 88, 615

—. 1934, MNRAS, 94, 765

—. 1935, MNRAS, 95, 639

—. 1936, MNRAS, 96, 698

—. 1938, MNRAS, 98, 673

—. 1939, MNRAS, 99, 697

—. 1947, MNRAS, 107, 401

—. 1948, MNRAS, 108, 186

—. 1950, MNRAS, 110, doi:10.1093/mnras/110.6.621

—. 1953, MNRAS, 113, 258

Stetson, P. B. 1987, PASP, 99, 191

Strader, J., Chomiuk, L., Maccarone, T. J., Miller-Jones, J. C. A., & Seth, A. C. 2012, Nature, 490, 71

Strope, R. J., Schaefer, B. E., & Henden, A. A. 2010, AJ, 140, 34

Sugizaki, M., Mitsuda, K., Kaneda, H., et al. 2001, ApJS, 134, 77

Suleimanov, V., Bikmaev, I., Belyakov, K., et al. 2004, Astronomy Letters, 30, 615

Szewczuk, W., & Daszyńska-Daszkiewicz, J. 2012, Astronomische Nachrichten, 333, 942

Szkody, P., & Mateo, M. 1984, ApJ, 280, 729

Taam, R. E., & Sandquist, E. L. 2000, ARA&A, 38, 113

Tauris, T. M., & van den Heuvel, E. P. J. 2006, Formation and evolution of compact stellar X-ray sources, ed. W. H. G. Lewin & M. van der Klis, 623–665

Torres, M. A. P., Jonker, P. G., Britt, C. T., et al. 2014, MNRAS, 440, 365

Udalski, A., Kowalczyk, K., Soszyński, I., et al. 2012, AcA, 62, 133

Valdes, F., Gruendl, R., & DES Project. 2014, in Astronomical Society of the Pacific Conference Series, Vol. 485, Astronomical Data Analysis Software and Systems XXIII, ed. N. Manset & P. Forshay, 379

van Amerongen, S., & van Paradijs, J. 1989, A&A, 219, 195

van Haaften, L. M., Nelemans, G., Voss, R., van der Sluys, M. V., & Toonen, S. 2015, A&A, 579, A33

Véron-Cetty, M. P., & Véron, P. 2000, A&ARv, 10, 81

Vogt, N. 1983, Sterne und Weltraum, 22, 123

Wade, R. A., & Horne, K. 1988, ApJ, 324, 411

Waelkens, C. 1991, A&A, 246, 453

Walczak, P., Szewczuk, W., & Daszyńska-Daszkiewicz, J. 2012, Astronomische Nachrichten, 333, 1065

Walker, M. F. 1957, in IAU Symposium, Vol. 3, Non-stable stars, ed. G. H. Herbig, 46

Warner, B. 2003, Cataclysmic Variable Stars

Warner, B., & Wickramasinghe, D. T. 1991, MNRAS, 248, 370

Warner, B., & Woudt, P. A. 2009, MNRAS, 397, 979

Weinberg, N. N., Arras, P., Quataert, E., & Burkart, J. 2012, ApJ, 751, 136

Wijnen, T. P. G., Zorotovic, M., & Schreiber, M. R. 2015, A&A, 577, A143

Wilms, J., Nowak, M. A., Pottschmidt, K., et al. 2001, MNRAS, 320, 327

Woudt, P. A., Warner, B., Gulbis, A., et al. 2012, MNRAS, 427, 1004

Wu, J., Jonker, P. G., Torres, M. A. P., et al. 2015, MNRAS, 448, 1900

Zurita, C., Casares, J., & Shahbaz, T. 2003, ApJ, 582, 369

Appendix A: Permission To Reproduce Figures

A.1 Copyright Agreement with AAS

The AAS is eager for the information published in its journals to reach the widest possible audience and it encourages the reuse of figures, tables, or other materials in review articles, textbooks, and other appropriate means of scholarly communication. To ensure the long-term access of the research community to its archives, the AAS holds the copyright on all copyrightable materials published in its journals, but the Society grants control of the right to reproduce the material to the original authors as long as they are alive.

A.2 Copyright Agreement with NASA

NASA content - images, audio, video, and computer files used in the rendition of 3-dimensional models, such as texture maps and polygon data in any format - generally are not copyrighted. You may use this material for educational or informational purposes, including photo collections, textbooks, public exhibits, computer graphical simulations and Internet Web pages. This general permission extends to personal Web pages.

A.3 Copyright Agreement with AAVSO

The AAVSO International Database is a collection of variable star observations made primarily by the amateur astronomical community, and includes data from AAVSO observers, observers affiliated with other variable star astronomy organizations that share and archive data with us, and data from professional researchers and published literature. Data are served in three primary ways: through the Light Curve Generator, via the QuickLook web tool, and via Data Download. In all cases these data are freely available to the community, but we request that users adhere to the policy outlined below. Doing so indicates that you support the mission of the AAVSO, and respect the organization and the worldwide community of observers who provided these data to you.

The AAVSO International Database is the product of the ongoing efforts and expertise of the volunteer observers who contribute the data and the AAVSO Headquarters technical staff who prepare and maintain the database with high quality-control standards. Please respect their and our work by using these data in accordance with our policies.

Formal policy: Acknowledgement for Using AAVSO Data

Acknowledgement for data correlation/reference:

If AAVSO data are used for correlation with other types of data, such as multiwavelength observations, or as reference material, we request the following acknowledgement or one similar to it:

"We acknowledge with thanks the variable star observations from the AAVSO International Database contributed by observers worldwide and used in this research."

A.4 Permission to use Figure 1.1

Dr. Frank,

I have to get written permission to use figures that are not mine in my thesis. May I use Figure 4.2 in your book "Accretion Power in Astrophysics" to describe the surface representing the Roche potential in a binary system?

Thanks,
Chris

Dear Chris,

This e-mail is to give you permission to use Fig. 4.2 from "Accretion Power in Astrophysics" in your PhD dissertation.

Sincerely,
Juhan Frank

date: Fri, Jul 1, 2016 at 10:29 AM

A.5 Permission to use Figure 1.2

Dr. Lattimer,

My name is Christopher Johnson and I am a PhD candidate at Louisiana State University working on X-ray sources in the Galactic Bulge region. I would like to use your Figure 2 from Lattimer, J. M., Prakash, M. 2007, PhR, 442, 109 in my thesis. We need to get written permission to use figures that are not our original work.

Thank you,

Christopher Johnson

Dear Christopher,

You have my permission to use the figure you requested.

James Lattimer
Distinguished Professor
Department of Physics Astronomy
Stony Brook University
(631)632-8227
James.Lattimer@StonyBrook.edu

date: Mon, Jun 27, 2016 at 4:39 PM

A.6 Permission to use Figure 1.5

Dr. Woudt,

My name is Chris Johnson and I am a PhD student at Louisiana State University working on X-ray sources in the Galactic Bulge Region. I am writing my thesis and need written permission to use figures that are not my original work. I would like to use your Figure 2 in the paper: Woudt, P. A., Warner, B., Gulbis, A., et al. 2012, MNRAS, 427, 1004. It is the light curve of CC Scl showing the superimposed spin period in the optical.

Thank you, Chris Johnson

Dear Chris,

Yes you have my permission.

Patrick Woudt

A.7 Permission to use Figure 1.6

Dr. Patterson,

My name is Chris Johnson and I am a PhD student at Louisiana State University working on X-ray sources in the Galactic Bulge Region. I am writing my thesis and need written permission to use figures that are not my original work. I would like to use your Figure 1 in

the paper: Patterson, J., 1994, PASP, 106, 209.

Thank you,
Chris Johnson

Hi Chris,

Sure, you can use that or any other figure of mine in any work, not just that one.

joe

date: Mon, Jun 27, 2016 at 2:25 PM

Vita

Christopher Charles Bradley Johnson was born in Detroit, Michigan, on March 5, 1985. He received a B.S. in Physics with a minor in Philosophy from the University of Arizona in May 2010. He was awarded an assistantship from the Department of Physics and Astronomy at Louisiana State University and began Graduate school in May of 2012. He earned his M.S. degree in Physics in 2015 and completed his Ph.D in Physics in August of 2016.